NUMERICAL STUDY ON INTERACTION EFFECT IN MULTIPLE CRACK PROBLEMS AND SOME PRACTICAL APPLICATIONS

アバス, アデインカ

NUMERICAL STUDY ON INTERACTION EFFECT IN MULTIPLE CRACK PROBLEMS AND SOME PRACTICAL APPLICATIONS

A dissertation submitted to Graduate School of Engineering, Kyushu University, Japan for the degree of Doctor of Philosophy in Engineering

Presented by

ADEYINKA ABASS

July 2023

TABLE OF CONTENTS

ABSTRACT

Prior to the emergence of a dominant major crack, many engineering fracture processes such as those observed in corrosion fatigue, fracture of weldments, fracture of casted component, stress corrosion cracking, thermal fatigue and fracture of additive-manufactured components can be modelled as a multiple crack problem. The computation of the stress intensity factors (SIFs) of the distributed cracks is an essential step in the application of fracture mechanics (FM) to such practical engineering problems. The determination of SIFs of a 3-D crack is a challenging endeavour since it is generally much more intricate, both analytically and numerically, than that of a 2-D crack. The presence of a free surface, such as in a semi-infinite body, results in greater difficulty. High computational cost becomes an additional bottleneck when multiple cracks are involved in the analysis.

Since the early 1970s, several FM models have been proposed for assessment of fracture process dominated by initiation, interaction, and coalescence of distributed cracks. These models can be divided into two categories, i.e., Size Dominant Model (SDM) and Interaction Dominant Model (IDM). In SDM, the crack with the largest size is assumed to be the primary actor in the fracture process, hence the existence of other cracks is irrelevant. Therefore, according to SDM, the task is simply to determine the dimensions of the largest crack, followed by estimation of relevant SIFs and comparing the results with threshold values. Majority of existing models are of SDM type.

In IDM, it is assumed that cracks in close proximity interact with each other. Therefore, it is necessary to include the interaction effect in the estimation of their SIFs and threshold conditions. Models of this type was pioneered by the work of Kitagawa (Kitagawa, 1978). In his paper, Kitagawa utilized Isida's 2-D solutions for two interacting cracks in a wide plate under tension to account for interaction effect among the 3-D fatigue cracks that initiated from

corrosion pits on a steel specimen. Clearly, applying a solution of two interacting 2-D cracks in a plate to multiple, randomly distributed, 3-D surface cracks is highly questionable. Unfortunately, since Kitagawa's papers, development of IDMs has stagnated. Perhaps this is due to the additional complexity that is involved in IDM, i.e., interaction effects among cracks. The interaction effect manifests itself in two forms i.e., interaction effect on threshold conditions (material resistance) and interaction effect on SIFs (load actions). Recently, papers on interaction effect on threshold conditions started to appear in literature, for example the work of Åman (Åman, 2020) and Okazaki (Okazaki, 2021). It seems research on crack interaction is experiencing a renaissance.

This thesis aims to address some of the challenges faced by FM based models targeted to engineering problems whose fracture processes are dominated by multiple interacting cracks. The main focus is the development of an efficient tool for numerical analysis of SIFs for multiple, 3-D, distributed, semi-elliptical cracks on the surface of a semi-infinite elastic body under arbitrary loading condition. A complementary objective is to develop a tool that can quantitatively characterise the spatial distribution of features, such as inclusions, pits, and cracks, on a given surface. The aspiration of this thesis is that such tools (numerical analysis of SIFs for multiple 3-D cracks and characterisation of spatial distribution of surface defects) will facilitate further research in this field, serves as valuable aid to advance our understanding of crack interaction phenomenon, and improve the performance of existing FM models targeted to multiple crack problems.

This dissertation consists of 6 Chapters which can be summarized as follows.

Chapter 1 described the central theme of this study, i.e., interaction effect in fracture processes that are dominated by initiation, propagation, and coalescence of multiple, distributed surface cracks. It introduced existing models for assessment of engineering

problems whose fracture processes are dominated by multiple interacting cracks. Existing solutions and research gap in the SIFs analysis of interacting 3-D surface cracks were briefly reviewed. Then, the objectives and outline of this study were introduced.

Chapter 2 provided the basic formulation, numerical procedure, and MATLAB codes for the numerical analysis of SIFs for multiple non-planar, semi-elliptical cracks that were distributed on the surface of a semi-infinite elastic body under arbitrary loading conditions. The eigenstrain method adopted for the study is based on the technique of distributing infinitesimal dislocation loops (IDLs) on the crack surfaces in order to satisfy their respective boundary conditions. This formulation led to a set of 2-D, hyper-singular integral equations. The integral equations had a singularity of order three and were interpreted in the Hadamard finite-part sense. In the numerical calculation, the crack regions were discretised into triangular sections. The discretisation transformed the integral equations into a system of algebraic equations. Corresponding MATLAB code for each stage of the numerical procedure is provided.

Chapter 3 applied the procedure of Chapter 2 to some problems of practical importance. Firstly, the accuracy of the analysis result was confirmed with a simple example, i.e., a single semi-elliptical surface crack under tension, by comparison with result from earlier work and known extreme cases. Then, more complex cases such as two parallel non-aligned cracks and random array of semi-elliptical surface cracks under tension were analysed.

Chapter 4 proposes two Nearest Neighbour Analysis (NNA)-based procedures as suitable statistical tools to quantitatively characterise the spatial distribution of cracks, defects, or inclusions (henceforth collectively refer to as “defects”). By using these procedures, the spatial distribution of defects can be categorised as ordered, random, clustered, or random with superimposed clusters. The validity of this approach was confirmed by the experimental results

for a medium-carbon steel, previously exposed to a mist of 3.5% NaCl solution for a duration of 0.5h to 6.0h. Finally, a new cleanliness rating method for materials exposed to corrosive environment was proposed.

Chapter 5 focused on different practical application area of the techniques developed in this study. The novel multiple 3-D crack analysis procedure was combined with Monte-Carlo simulation approach to propose a new method for material quality assessment, in consideration of the interaction effect of distributed material defects and loading. Pioneering study on when multiple cracks problem can be classified as crack size dominance or crack interaction dominance was reported. Finally, application to corrosion-fatigue prediction model was suggested.

Chapter 6 provided a summary of major findings from this study and suggestion for future research in this area.

NOMENCLATURE

a	Major radius of a crack
b	Minor radius of a crack
$\vec{\boldsymbol{b}}$	Burgers vector of a dislocation loop
$b_{\mathrm{x}}, b_{\mathrm{y}}, b_{\mathrm{z}}$	Components of the Burgers vector of a dislocation loop
c	Distance between cracks along the global Z axis
$f_1^{i,j}$, $f_2^{i,j}$, $f_3^{i,j}$	Unknown constants of element *j* of crack *i*
$F_{\mathrm{I}}, F_{\mathrm{II}}, F_{\mathrm{III}}$	Dimensionless Modes I, II and III stress intensity factors
h	Distance between cracks along the global X axis
K_{ij}	Kernel function of the fundamental infinitesimal dislocation solution
$K_{\mathrm{I}}, K_{\mathrm{II}}, K_{\mathrm{III}}$	Modes I, II, III stress intensity factors
l, m, n	Local crack coordinate system
N	Total number of cracks in the body
X, Y, Z	Global coordinate system
$T_{\mathrm{jkm}}(\boldsymbol{x}, \boldsymbol{\xi})$	Stress tensor at point $\boldsymbol{x}$ due to unit point forces at $\boldsymbol{\xi}$ in a semi-infinite body
x, y, z	Coordinate system of point $\boldsymbol{x}$
α	A parameter that can take the value of 0, 0.5 or 1.0
$\gamma_{\mathrm{A}}, \gamma_{\mathrm{B}}, \gamma_{\mathrm{C}}$	Interaction factor at points A, B and C
δ_{ij}	Kronecker delta
δS	Area of an infinitesimal dislocation loop
μ	Modulus of rigidity
v	Poisson's ratio
$\sigma_{\mathrm{iz}}(\boldsymbol{x})$	Stress components at point $\boldsymbol{x}$ of the semi-infinite body
ξ, η, ζ	Coordinate system of point $\boldsymbol{\xi}$
ρ	The density of the features per unit area
φ	Size ratio of the largest crack to average size of the population

ACRONYMS

AM	Additive manufacturing
NNA	Nearest neighbour analysis
FEM	Finite element method
FM	Fracture mechanics
IDL	Infinitesimal dislocation loop
SCDM	Stress component division method
BFM	Body force method
BIEM	Boundary integral equation method
SIF	Stress intensity factor
QR method	A method to characterise spatial distribution of features
Schwartz method	A method to separate cluster features from random features

CHAPTER 1. General introduction

1.1 Research background

1.1.1 Multiple crack problems in fracture of engineering structures

Failure analysis of many structural failures revealed the root cause of the fracture process as multiple cracks that were initiated at region with high stress concentrations [1-9]. In most of these cases, the cracks initiated from pre-existing defects such as non-metallic inclusions, cavities, weldments, scratches, corrosion pits and others. The interaction and coalescence of the distributed cracks led to the emergence of a dominant crack that lead to fracture.

Additive manufacturing (AM) technology holds tremendous potential in material efficiency and easy production of low volume components. Results from many studies indicate the presence of multiple crack initiation sites in the samples [4, 5, 9]. For example, Molaei and Fatemi [9] reported multiple fatigue cracks on the outer surface of an AM as-built heat treated 17-4 PH specimens subjected to different cyclic loading. Some of these cracks are shown in Fig. 1.1. The cracks initiation site is determined by the pre-existing surface defects network from the manufacturing process.

Engineered structures and machineries are often subjected to combined effect of corrosive environment and mechanical loading which makes them susceptible to corrosion fatigue phenomenon. Extensive research over the years showed that corrosion fatigue mechanism involves the appearance of multiple pits, mostly at non-metallic inclusion sites of the base metal where they serve as local galvanic cells, followed by the pit growth stage. Due to the cyclic loading, a multiplicity of small fatigue cracks originates from the pits, the interaction and resultant coalescence of which eventually lead to the formation of a major crack that will dominate fracture [1].

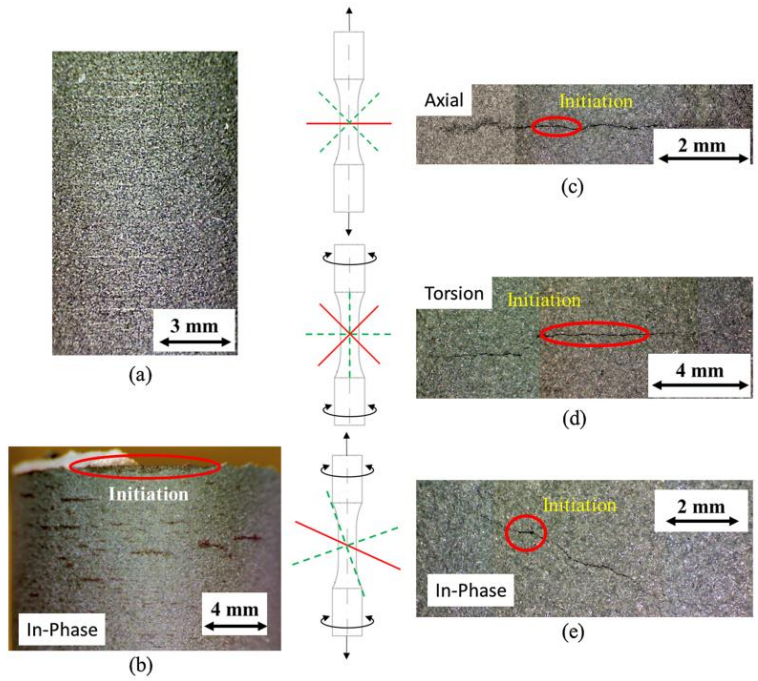

Fig. 1.1 Representative of multiple circumferentially connected defect-networks/cracks resulting from fabrication process on the outer surface of AM vertically-built 17-4 PH specimens with as-built surface: (a) before testing and (b) after undergoing combined in-phase axial-torsion load with N_f = 3157 cycles. Failure crack orientation under (c) axial, (d) torsion, and (e) combined in-phase axial-torsion loadings. All crack initiations are along the weak build plane orientations for vertically built specimens. Solid red lines indicate maximum principal plane orientations and dashed green lines represent maximum shear plane directions [9].

Consequently, an understanding of the multiple crack initiation/interaction behaviour is essential to the development of a blueprint for forecasting corrosion fatigue life, based on the actual damage scenario. For example, Kitagawa et al. [10] observed multiple fatigue cracks on the surface of a high strength steel specimen under cyclic loading in a corrosive chamber as presented in Fig. 1.2.

In fatigue of weldment, the existence of multiple fatigue cracks along the toes of the weld seams has been reported [11-13]. For instance, Zerbst et. al [11], observed many small cracks in the early stages of the fracture of a butt weld. Subsequent growth and coalescence of the cracks lead to reduction in the number of cracks and eventually the emergence of a main crack that lead to failure, as shown in Fig. 1.3.

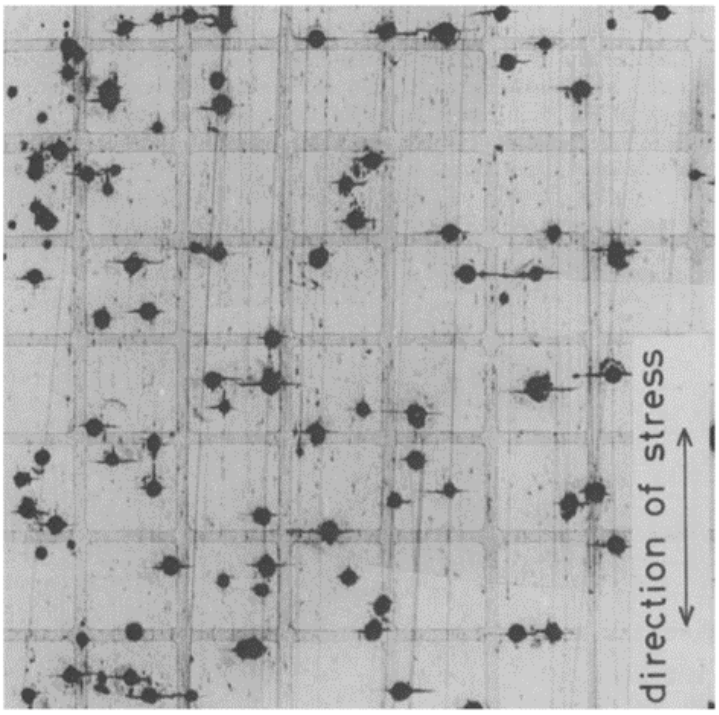

Fig. 1.2 Multiple corrosion-fatigue cracks on the surface of a high-strength-steel plate, after exposure to a corrosive environment at a stress-range of 235 MPa after one million cycles. All the cracks initiated from corrosion-pits [10].

Furthermore, it was reported in the literature [11] that a significant part of the total life of the butt weld passed before the emergence of the dominating major crack, i.e., major part of the fatigue life was spent in the propagation, interaction, and coalescence of multiple small cracks.

All the cases discussed above shared a common characteristic. That is, their fracture process can be modelled as a multiple crack problem prior to the emergence of a dominant major crack. This implies that fracture mechanics, the science of cracks, will be highly effective for their strength assessment. The discussion above clarifies the importance of research to further improve our understanding of the behaviour of multiple cracks with regards to their spatial distribution, interactions, coalescence, and their applications to problems of practical importance.

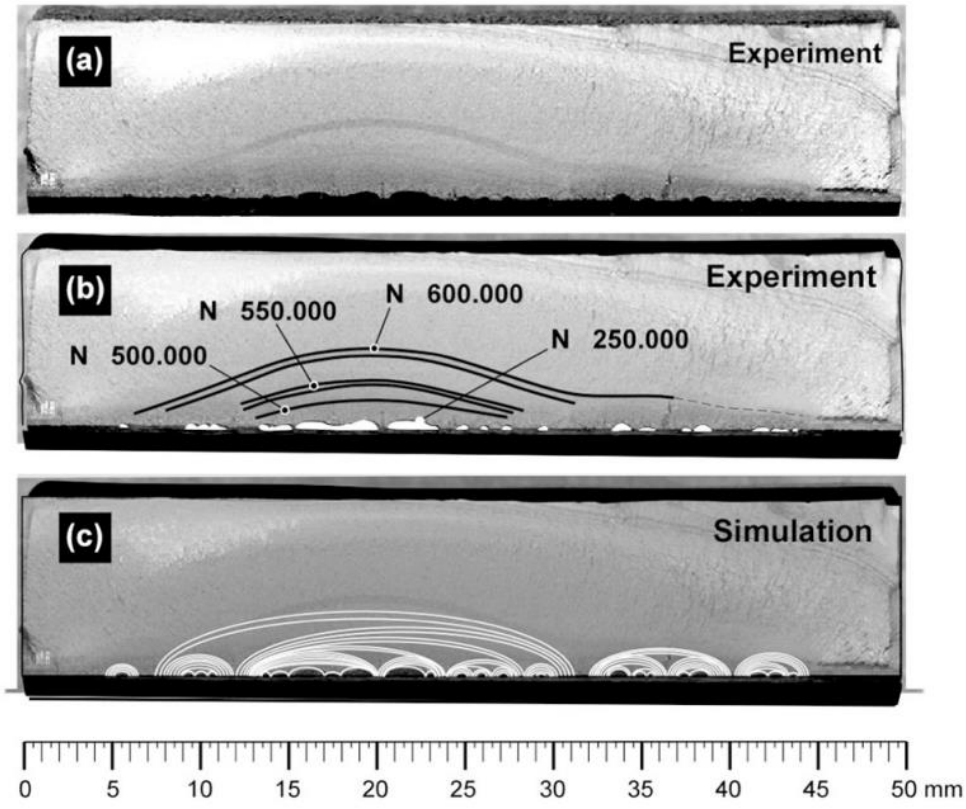

Fig. 1.3 Multiple fatigue crack propagation and coalescence (a) marked cracks (by heat tinting and beach marking) (b) replotted pattern with the corresponding numbers of loading cycles (c) results of a simulation starting from the cracks visualized by heat tinting (black and white areas at the lower edge in (a) and (b) as initial cracks; S355NL; R = −1 [11]

1.1.2 Stress Intensity Factors (SIFs)

When fracture of a structure occurs at stress level well below the yield strength of the structural material, the preceding failure analysis often attribute the fracture to cracks or cracklike defects in the structure that were not accounted for during the design stage. Such failures are not uncommon and suggest that the conventional strength analysis of structures alone is not always sufficient to guarantee structural integrity under operational conditions. In such cases, the analysis of stress state ahead of crack tip is fundamental for the prevention of

such fracture accidents. Fracture mechanics (FM) is the scientific field concerned with analysing the failure of materials containing cracks and flaws.

In elastic analysis of cracked body, the Stress Intensity Factors (SIFs) characterises the stress, strain, and displacement fields in the vicinity of the crack tip since it represents the magnitude of the dominant singular term of the stress state, this makes it an important parameter in design and fracture analysis using FM approach [14-15]. The determination of SIFs is an essential step in the application of FM to practical engineering problems. Several researchers have reported solutions for numerous SIFs problems for 2-D and 3-D cracks. The determination of SIFs of 3-D cracks is a challenging endeavour since it is generally much more intricate, both analytically and numerically, than that of 2-D cracks [16-20]. The presence of a free surface, such as in a semi-infinite body, results in greater difficulty because the free surface constitutes an additional boundary condition that must be considered in the basic formulation of the governing equations [17-29]. In practice, most defects are often approximated as 3-D elliptical cracks. For this reason, it is important for researchers to focus attention on SIF analyses for 3-D cracks despite the enormous difficulties involved.

Although the finite element method (FEM) can be used to calculate the SIFs of 3-D cracks with sufficient accuracy, it is virtually impracticable when multiple distributed cracks are involved. This is due to the considerable effort required to develop fine meshes in the vicinity of the cracks and the high computational resources necessary to obtain a satisfactory solution [30]. Other numerical approaches such as the body force method (BFM) and boundary integral equation method (BIEM) have found wide applications in 3-D crack analysis [14]. Numerous solutions addressing the case of multiple cracks in an infinite body can be found in the existing literature [31-37]. Numerical analysis of interacting distributed cracks in an elastic semi-infinite body involves highly complicated mathematical formulation. This has limited available solutions to very special cases (e.g., coplanar, and parallel cracks) where some of the

complication significantly ease. Fig 1.1-1.3 showed that multiple 3-D, distributed, surface cracks often exist in many application. Therefore, it is important for researchers to focus attention on SIFs analysis of distributed 3-D surface cracks despite the enormous difficulties involved.

1.1.3 Research gap in assessment of structural failure involving multiple cracks

FM based models that account for the presence of multiple cracks/defects in assessment of many practical engineering problems in different fields have been appearing in literature since the early 1970s. These models can be divided into two categories, i.e., Size Dominant Model (SDM) and Interaction Dominant Model (IDM).

In SDM, the crack with the largest size is assumed to be the primary actor in the fracture process, hence the existence of other cracks is irrelevant. Therefore, according to SDM, the task is simply to determine the dimensions of the largest crack, followed by estimation of relevant SIFs and comparing the results with threshold values. There are few special SDM models that include the statistical variation in the sizes of the cracks (or defects modelled as crack) in their formulation. Most models of this type use the variation in the crack sizes to explain variation in the fracture strength and advocate for a probabilistic approach to strength assessment [4, 6, 11-13]. Others invoked statistics of extreme to predict the maximum crack size contained in a given control volume [2]. The noteworthy merit of statistics of extremes is that it can allow for the effect of control volume, i.e., the maximum cracks included in a structure naturally increase with a rise in sample population.

In IDM, it is assumed that cracks in close proximity interacts with each other. Therefore, it is necessary to include the interaction effect in the estimation of SIFs and threshold conditions. Models of this type was pioneered by the work of Kitagawa in 1970s [10]. Unfortunately, since Kitagawa's paper [10], development of IDMs has stagnated. Perhaps this might be due to the additional difficulty that is involved in IDM, i.e., interaction effects among cracks. The interaction effect manifests itself in two forms. They are; interaction effect on threshold conditions (material resistance) and interaction effect on SIFs (load actions). There are surprisingly very few studies on influence of interacting cracks/defects on thresholds (such as fatigue limit) of engineering material. Recently, this area of research is beginning to gather attention. For example, Åman [7,8] investigated the influence of interacting small defects on the fatigue limit of a medium carbon steel (JIS-S45C), pure iron (JIS-SUY1) and a bearing steel (JIS-SUJ2). Okazaki [38] conducted investigation on the interaction effect of adjacent circumferential V-notches on the fatigue limit of structural steel (JIS-SM490B) and a Nickel-based superalloy (Alloy 718). Results from these studies indicate that interaction effect on thresholds is material dependent and in most cases differs from predictions derived from analytical solution of interaction effect on SIFs of the cracks. Further research is needed in this area.

From the discussion above, the obvious conclusion is that IDMs are more challenging to formulate and implement in practice than SDMs. Therefore, for cases where multiple cracks are involved in the fracture process, it will be useful to have a guideline to determine if it is sufficient to focus the assessment solely on the crack with largest size without the need to consider interaction effect. In other words, there is a need for a procedure to choose between IDM and SDM. At present, such a procedure is not in existence.

Kitagawa [10] utilized Isida's 2-D solutions for two interacting cracks in a wide plate under tension to account for interaction effect among the 3-D fatigue cracks that initiated from

corrosion pits on a steel specimen subjected to cyclic tension-compression in a corrosive environment. Clearly, applying a solution obtained for two interacting 2-D cracks in a wide plate to multiple, randomly distributed, 3-D surface cracks is highly questionable. What is needed is a tool to estimate the interaction effect among multiple, distributed 3-D cracks under arbitrary loading.

In literature, some solutions of 3-D crack interaction have been reported. Murakami employed BFM to study two dissimilar, semi-elliptical coplanar cracks in a semi-infinite body under tension and bending loading [39, 40]. Isida et al. also utilised BFM to investigate the interaction of multiple (i.e., two to five), periodically-arrayed, parallel, semi-elliptical surface cracks in a semi-infinite body under tension [41]. Moussa et al. used FEM to analyse the nature of the interaction between two identical, non-coplanar, semi-elliptical surface cracks in an infinite plate under tension and pure bending [42]. Åman et al. proposed an FEM-based procedure known as the stress component division method (SCDM), to obtain SIFs for interacting arbitrarily-shaped 3-D cracks [43]. SCDM employs commercially-available FEM software for crack interaction analysis without the need for singular elements or complicated meshing procedures. Although SCDM does not require fine meshes in the vicinity of the cracks, it remains computationally expensive when tens or hundreds of randomly-distributed cracks are involved. As previously noted, the existing literature reflects a dearth of analysis for arbitrarily-distributed cracks in a semi-infinite body under tension and shear loading. Therefore, further development of the analysis method is expected to tackle, more precisely, problems where the fracture process is dominated by nucleation, interaction, and coalescence of randomly-distributed cracks.

1.2 Objective of this study

The study addresses some of the challenges in FM based models that are used in the assessment of engineering problems whose fracture processes are dominated by multiple interacting cracks. The main focus is the development of an efficient method for numerical analysis of SIFs for multiple, 3-D, distributed, semi-elliptical cracks on the surface of a semi-infinite elastic body under arbitrary loading condition. A complementary objective is to develop a suitable method that can quantitatively characterise the spatial distribution of features, such as inclusions, pits, and cracks, on a given surface.

Furthermore, previous section elucidated that existing model for fracture assessment of multiple crack problems can be divided into size dominance model (SDM) and interaction dominance model (IDM). While SDMs focus on the crack with largest size, IDMs , on the other hand, prioritised the interaction among the cracks. However, there is no study that establish when to invoke SDM or IDM for a multiple crack problem. This study aims to address this research gap.

1.3 Thesis outline

This thesis consists of 6 chapters. The thesis outline is follows:

Chapter 1 described the central theme of this study, i.e., interaction effect in fracture processes that are dominated by initiation, propagation, and coalescence of multiple, distributed surface cracks. It introduced existing models for assessment of engineering problems whose fracture processes are dominated by multiple interacting cracks. Existing solutions and research gap in the SIFs analysis of interacting 3-D surface cracks were briefly reviewed. Then, the objectives and outline of this study were introduced.

Chapter 2 provided the basic formulation, numerical procedure, and MATLAB codes for the numerical analysis of SIFs for multiple non-planar, semi-elliptical cracks that were distributed on the surface of a semi-infinite elastic body under arbitrary loading conditions. The eigenstrain method adopted for the study is based on the technique of distributing infinitesimal dislocation loops (IDLs) on the crack surfaces in order to satisfy their respective boundary conditions. This formulation led to a set of 2-D, hyper-singular integral equations. The integral equations had a singularity of order three and were interpreted in the Hadamard finite-part sense. In the numerical calculation, the crack regions were discretised into triangular sections. The discretisation transformed the integral equations into a system of algebraic equations. Corresponding MATLAB code for each stage of the numerical procedure is provided.

Chapter 3 applied the procedure of Chapter 2 to some problems of practical importance. Firstly, the accuracy of the analysis result was confirmed with a simple example, a single semi-elliptical surface crack under tension, by comparison with result from earlier work and known extreme cases. Then, more complex cases such as two parallel non-aligned cracks and random array of semi-elliptical surface cracks under tension were analysed.

Chapter 4 proposes two Nearest Neighbour Analysis (NNA)-based procedures as suitable statistical tools to quantitatively characterise the spatial distribution of cracks, defects, or inclusions (henceforth collectively refer to as “defects”). By using these procedures, the spatial distribution of defects can be categorised as ordered, random, clustered, or random with superimposed clusters. The validity of this approach was confirmed by the experimental results

for a medium-carbon steel, previously exposed to a mist of 3.5% NaCl solution for a duration of 0.5h to 6.0h. Finally, a new cleanliness rating method for materials exposed to corrosive environment was proposed.

Chapter 5 focused on different practical application area of the techniques developed in this study. The novel multiple 3-D crack analysis procedure was combined with Monte-Carlo simulation approach to propose a new method for material quality assessment, in consideration of the interaction effect of distributed material defects and loading. Pioneering study on when multiple cracks problem can be classified as crack size dominance or crack interaction dominance was reported. Finally, application to corrosion-fatigue prediction model was suggested.

Chapter 6 provided a summary of major findings from this study and suggestion for future research in this area.

CHAPTER 2. Analysis of SIFs of distributed surface cracks in a body

2.1 Basic formulation

At first, a semi-infinite elastic body was considered under arbitrary loading conditions with no cracks. The stress state at every point of the body is known based on a suitable analytical or numerical method. Multiple, distributed, non-planar, semi-elliptical cracks were then introduced on the surface of the body, as shown in Fig. 2.1. Each crack possessed its own local coordinate system, as can be seen in Fig. 2.2. Since the origin of each local coordinate system could be expressed in the global coordinate system, they were mutually transformable. In general, the crack-faces can undergo three displacement modes as a result of the external boundary conditions: opening mode (Mode I), shearing mode (Mode II) and tearing mode (Mode III).

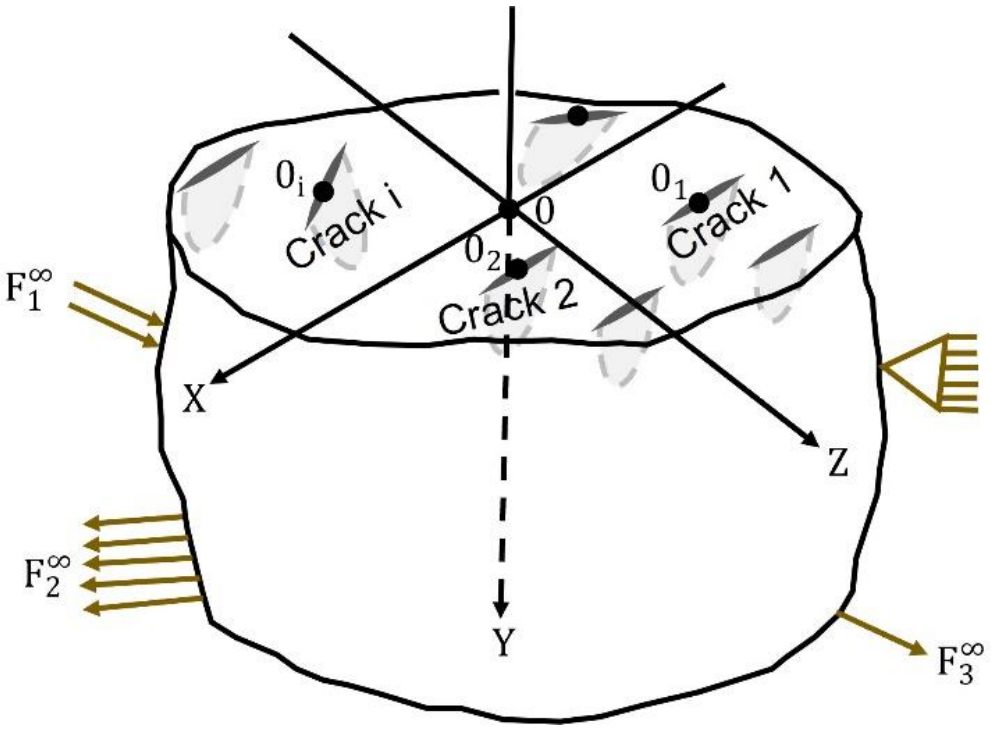

Fig. 2.1 Distribution of cracks on the surface of a semi-infinite body under arbitrary loading conditions.

The central aim of this research was to determine the distribution functions of the relative displacement of crack-faces in each crack. Once the displacement functions are identified, SIFs corresponding to the three modes can easily be ascertained from the asymptotic relationship between crack-front displacement discontinuities and SIFs [44].

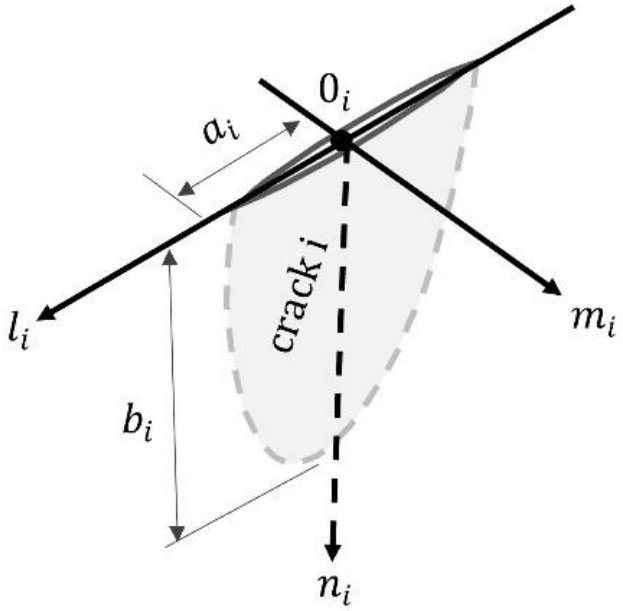

Fig. 2.2 Local crack coordinate system.

When the cracks are modelled as continuously-distributed IDLs with the area of an IDL, δS, and Burgers vector, $\vec{\boldsymbol{b}} = (b_{\mathrm{x}}, b_{\mathrm{y}}, b_{\mathrm{z}})$, the relative displacements of the crack-faces are represented by $\vec{\boldsymbol{b}}$ of the IDLs [45]. Therefore, once the Burgers vector components are obtained for each crack, the three relative displacement modes of the crack-faces can be determined. Following the coordinate system in Fig. 2.2, the Mode I displacement corresponds to b_{z}, while b_{x} and b_{y} correspond to displacements in Modes II and III, respectively. The correct distributions of the IDLs are those which satisfy the traction-free condition on overall crack-faces. This formulation resulted in a set of 2-D, hyper-singular integral equations. In order to derive the integral equations, it was necessary to obtain the expressions for the stresses at any point in a semi-infinite body due to an IDL at an arbitrary location in the body. In Fig.

2.3, of interest were the stress components, $\sigma_{\mathrm{iz}}(\boldsymbol{x})$, at point $\boldsymbol{x}$, due to an IDL of area, δS, located at point $\boldsymbol{\xi}$ in the elastic body. $\sigma_{\mathrm{iz}}(\boldsymbol{x})$ is expressed by:

$$\sigma_{\mathrm{iz}}(\boldsymbol{x}) = K_{\mathrm{ij}}(\boldsymbol{x}, \boldsymbol{\xi}) b_{\mathrm{j}}(\boldsymbol{\xi}) \tag{2-1}$$

where,

i, j: x, y and z;

$\sigma_{\mathrm{iz}}(\boldsymbol{x})$ are stress components at point $\boldsymbol{x}$ in the semi-infinite body expressed in the local coordinate system of the crack where $\boldsymbol{x}$ is located.

$b_j(\boldsymbol{\xi})$ are components of the Burgers vector of the IDL at point $\boldsymbol{\xi}$ expressed in the local coordinate system of the crack where $\boldsymbol{\xi}$ is located; and $K_{\mathrm{ij}}(\boldsymbol{x}, \boldsymbol{\xi})$ denotes Kernel function, the fundamental infinitesimal dislocation solution.

The expression for $K_{\mathrm{ij}}(\boldsymbol{x}, \boldsymbol{\xi})$ was derived in tensor form by Bacon and Groves [46] as:

$$K_{\mathrm{ij}}(\boldsymbol{x}, \boldsymbol{\xi}) = \mu \left[\frac{\partial T_{\mathrm{ziz}}(\boldsymbol{x}, \boldsymbol{\xi})}{\partial \xi_{\mathrm{j}}} + \frac{\partial T_{\mathrm{zij}}(\boldsymbol{x}, \boldsymbol{\xi})}{\partial \zeta} + \frac{2\nu}{1-2\nu} \frac{\partial T_{\mathrm{zim}}(\boldsymbol{x}, \boldsymbol{\xi})}{\partial \xi_{\mathrm{m}}} \delta_{\mathrm{ij}} \right] \tag{2-2}$$

where,

$T_{\mathrm{jkm}}(\boldsymbol{x}, \boldsymbol{\xi})$ is the stress tensor at point $\boldsymbol{x}$ (x, y, z) due to unit point forces at $\boldsymbol{\xi}$ (ξ, η, ζ) in a semi-infinite body, as first derived by Mindlin [47];

μ is Modulus of rigidity;

ν is Poisson's ratio;

x, y, z represents the coordinate system of point $\boldsymbol{x}$;

ξ, η, ζ denotes the coordinate system of point $\boldsymbol{\xi}$; and

δ_{ij} is Kronecker delta.

Starting from the Mindlin solution for stresses in a semi-infinite body due to three unit point forces, *P*, *Q* and *R*, pointing in the *z*, *x*, and *y* axes, respectively, the explicit expression of Eq. (2-1) is given as follows:

$$\sigma_{zz} = \frac{2\mu(1-\nu)}{1-2\nu}\left[\frac{\partial\sigma_{zz}^{P}}{\partial\zeta} + \frac{\nu}{1-\nu}\left(\frac{\partial\sigma_{zz}^{Q}}{\partial\xi} + \frac{\partial\sigma_{zz}^{R}}{\partial\eta}\right)\right] b_z + \mu\left[\frac{\partial\sigma_{zz}^{P}}{\partial\xi} + \frac{\partial\sigma_{zz}^{Q}}{\partial\zeta}\right] b_x + \mu\left[\frac{\partial\sigma_{zz}^{P}}{\partial\eta} + \frac{\partial\sigma_{zz}^{R}}{\partial\zeta}\right] b_y \qquad (2\text{-}3a)$$

$$\tau_{xz} = \frac{2\mu(1-\nu)}{1-2\nu}\left[\frac{\partial\tau_{xz}^{P}}{\partial\zeta} + \frac{\nu}{1-\nu}\left(\frac{\partial\tau_{xz}^{Q}}{\partial\xi} + \frac{\partial\tau_{xz}^{R}}{\partial\eta}\right)\right] b_z + \mu\left[\frac{\partial\tau_{xz}^{P}}{\partial\xi} + \frac{\partial\tau_{xz}^{Q}}{\partial\zeta}\right] b_x + \mu\left[\frac{\partial\tau_{xz}^{P}}{\partial\eta} + \frac{\partial\tau_{xz}^{R}}{\partial\zeta}\right] b_y \qquad (2\text{-}3b)$$

$$\tau_{yz} = \frac{2\mu(1-\nu)}{1-2\nu}\left[\frac{\partial\tau_{yz}^{P}}{\partial\zeta} + \frac{\nu}{1-\nu}\left(\frac{\partial\tau_{yz}^{Q}}{\partial\xi} + \frac{\partial\tau_{yz}^{R}}{\partial\eta}\right)\right] b_z + \mu\left[\frac{\partial\tau_{yz}^{P}}{\partial\xi} + \frac{\partial\tau_{yz}^{Q}}{\partial\zeta}\right] b_x + \mu\left[\frac{\partial\tau_{yz}^{P}}{\partial\eta} + \frac{\partial\tau_{yz}^{R}}{\partial\zeta}\right] b_y \qquad (2\text{-}3c)$$

An investigation of the genesis of Eq. (2-3) required 21 painstaking derivatives of expressions for the stress components in the Mindlin solution, undertaken for the first time for the present study and provided in detail in Appendix A.

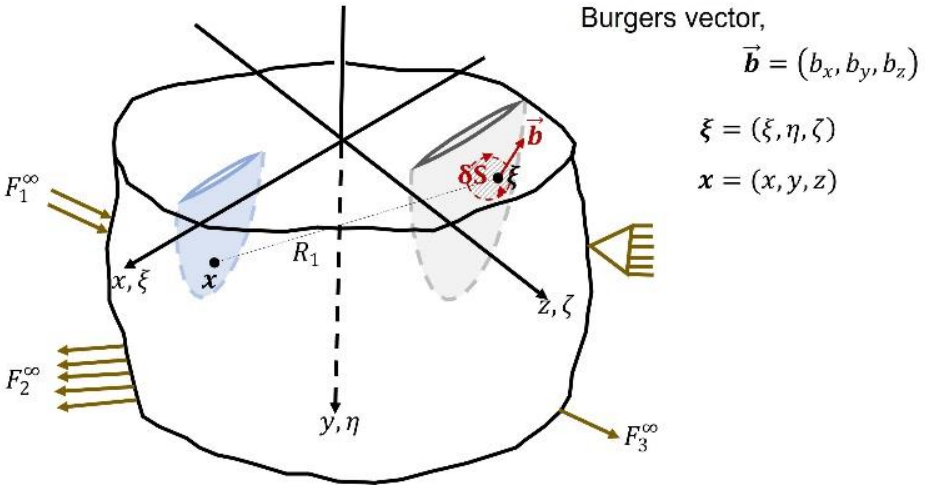

Fig. 2.3 Stresses in a semi-infinite body due to an infinitesimal dislocation loop.

With the solution of stresses at a given point courtesy of an arbitrarily-located IDL now available, the formulation of an integral equation system becomes straightforward. The total number of surface cracks should be *N* under arbitrary loading conditions, where the crack-faces undergo three modes of relative displacement. These relative displacements were modelled as distributed IDL, $\vec{\boldsymbol{b}}$, the distribution function of which was unknown for each crack. The correct density distribution of the IDLs

for each crack simultaneously satisfied the traction-free conditions on overall crack-faces. In other words, the correct distribution was that which nullified the stresses due to external loadings at locations occupied by the cracks. Mathematically, this condition is expressed by:

$$\sum_{k=1}^{N}\left(\int_{S_k} K_{ij}(\boldsymbol{x},\,\boldsymbol{\xi}) b_j^k(\boldsymbol{\xi})\delta S\right) = -t_i^{\infty}(\boldsymbol{x}) \qquad (2\text{-}4)$$

where,

$t_i^{\infty} = \begin{bmatrix}\sigma_{xz}^{\infty}\\ \sigma_{yz}^{\infty}\\ \sigma_{zz}^{\infty}\end{bmatrix}$ are stresses at point $\boldsymbol{x}$ due to external loading;

N represents the total number of cracks in the body;

$b_j^k(\boldsymbol{\xi})$ is the Burgers vector component of the IDL at point $\boldsymbol{\xi}$ of the k_{th} crack; and

S_k is the integration area of the k_{th} crack.

The unknown terms in the set of integral equations were the distribution densities of b_j^k for the cracks, the solutions of which can be applied to compute many fracture mechanics parameters of practical importance. In this case, they were adopted to compute the SIFs for the cracks using the asymptotic relationship.

Since it was not possible to derive an analytical solution for the set of integral equations in Eq. (2-4), a numerical procedure was therefore required. Furthermore, Eq. (2-4) comprises a set of hyper-singular integral equations because $K_{ij}(\boldsymbol{x},\boldsymbol{\xi})$ has a singularity of order 3 as $\boldsymbol{x}$ approaches $\boldsymbol{\xi}$. This can be confirmed by a review of the equations in Appendix A. Hence, Eq. (2-4) must be interpreted in the Hadamard finite-part sense [48].

2.2 Numerical procedure

It is noteworthy that the preceding formulation and derived equations were independent of the geometry of the cracks. In this case, the following numerical procedures were developed specifically

for arbitrarily-distributed surface cracks, all of which were semi-elliptical in shape with different aspect ratios. Each crack-plane was divided into a few triangular segments, following the simple pattern featured in Fig. 2.4. The unknown field function was represented as a piecewise constant approximation, whereby it was approximated by the product of a known weight function and an unknown constant. The choice of the weight function is important for the effectiveness and accuracy of the approximation. In the case of elliptical cracks, an analytical expression for a suitable weight function was proposed by Eshelby [49].

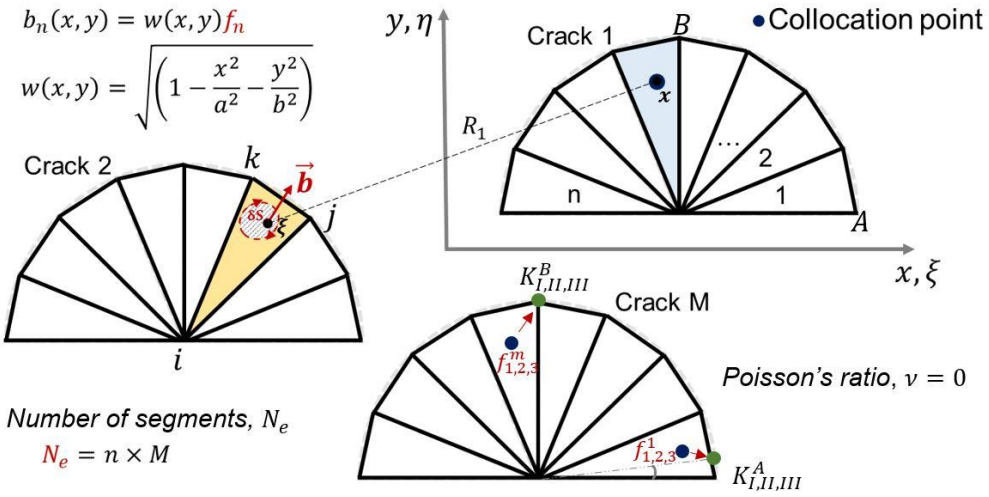

Fig. 2.4 Discretisation of the crack-faces into triangular segments.

Therefore, the relative crack-face displacement function, $\vec{\boldsymbol{b}} = (b_x, b_y, b_z)$, for the j_{th} element in the i_{th} crack is approximated numerically by:

$$b_x^{i,j} = \left(1 - \frac{x^2}{a_i^2} - \frac{y^2}{b_i^2}\right)^{1/2} f_1^{i,j} \; ; \; b_y^{i,j} = \left(1 - \frac{x^2}{a_i^2} - \frac{y^2}{b_i^2}\right)^{1/2} f_2^{i,j} \; ; \; b_z^{i,j} = \left(1 - \frac{x^2}{a_i^2} - \frac{y^2}{b_i^2}\right)^{1/2} f_3^{i,j} \quad (2\text{-}5)$$

where,

$b_x^{i,j}$, $b_y^{i,j}$, $b_z^{i,j}$ are components of the Burgers vector of the j_{th} element in the i_{th} crack;

a_i, b_i are the major and minor radii of the i_{th} crack; and $f_1^{i,j}$, $f_2^{i,j}$, $f_3^{i,j}$ are constants of the j_{th} element in the i_{th} crack.

Furthermore, the traction-free requirement on overall crack-faces is relaxed, such that it is only enforced at the centroid of the elements [17-18, 21-22]. Therefore, Eq. (2-4) can be rewritten as:

$$\sum_{m=1}^{N_e}(K_{mn}^{33}f_3^m + K_{mn}^{32}f_2^m + K_{mn}^{31}f_1^m) = -\sigma_{zz\infty}^n(x^n, y^n) \quad (n = 1, 2, \dots, N_e) \tag{2-6a}$$

$$\sum_{m=1}^{N_e}(K_{mn}^{23}f_3^m + K_{mn}^{22}f_2^m + K_{mn}^{21}f_1^m) = -\sigma_{yz\infty}^n(x^n, y^n) \quad (n = 1, 2, \dots, N_e) \tag{2-6b}$$

$$\sum_{m=1}^{N_e}(K_{mn}^{13}f_3^m + K_{mn}^{12}f_2^m + K_{mn}^{11}f_1^m) = -\sigma_{xz\infty}^n(x^n, y^n) \quad (n = 1, 2, \dots, N_e) \tag{2-6c}$$

Equation (2-6), in turn, can then be revised in matrix format, as documented in Eq. (2-7).

$$\sum_{m=1}^{N_e}\left(\begin{bmatrix} K_{mn}^{33} & K_{mn}^{32} & K_{mn}^{31} \\ K_{mn}^{23} & K_{mn}^{22} & K_{mn}^{21} \\ K_{mn}^{13} & K_{mn}^{12} & K_{mn}^{11} \end{bmatrix} \cdot \begin{bmatrix} f_3^m \\ f_2^m \\ f_1^m \end{bmatrix}\right) = \begin{bmatrix} -\sigma_{zz\infty}^n(x^n, y^n) \\ -\sigma_{yz\infty}^n(x^n, y^n) \\ -\sigma_{xz\infty}^n(x^n, y^n) \end{bmatrix} \quad (n = 1, 2, \dots, N_e) \tag{2-7}$$

where,

N_e is the total number of elements;

(x^n, y^n) are the centroid coordinates of the n_{th} element; and

$\sigma_{xz\infty}^n, \sigma_{yz\infty}^n$ and $\sigma_{zz\infty}^n$ are stresses at the centroid of the n_{th} element.

Table 2.1 Expressions for the Kernel matrix of Equation (2-7).

Kernel	Expression
$\boldsymbol{K_{mn}^{11}}$	$\mu\left[\frac{\partial\tau_{xz}^P}{\partial\xi} + \frac{\partial\tau_{xz}^Q}{\partial\zeta}\right]\left(1 - \frac{x^2}{a_m^2} - \frac{y^2}{b_m^2}\right)^{1/2}$
$\boldsymbol{K_{mn}^{12}}$	$\mu\left[\frac{\partial\tau_{xz}^P}{\partial\eta} + \frac{\partial\tau_{xz}^R}{\partial\zeta}\right]\left(1 - \frac{x^2}{a_m^2} - \frac{y^2}{b_m^2}\right)^{1/2}$
$\boldsymbol{K_{mn}^{13}}$	$\frac{2\mu(1-\nu)}{1-2\nu}\left[\frac{\partial\tau_{xz}^P}{\partial\zeta} + \frac{\nu}{1-\nu}\left(\frac{\partial\tau_{xz}^Q}{\partial\xi} + \frac{\partial\tau_{xz}^R}{\partial\eta}\right)\right]\left(1 - \frac{x^2}{a_m^2} - \frac{y^2}{b_m^2}\right)^{1/2}$
$\boldsymbol{K_{mn}^{21}}$	$\mu\left[\frac{\partial\tau_{yz}^P}{\partial\xi} + \frac{\partial\tau_{yz}^Q}{\partial\zeta}\right]\left(1 - \frac{x^2}{a_m^2} - \frac{y^2}{b_m^2}\right)^{1/2}$
$\boldsymbol{K_{mn}^{22}}$	$\mu\left[\frac{\partial\tau_{yz}^P}{\partial\eta} + \frac{\partial\tau_{yz}^R}{\partial\zeta}\right]\left(1 - \frac{x^2}{a_m^2} - \frac{y^2}{b_m^2}\right)^{1/2}$
$\boldsymbol{K_{mn}^{23}}$	$\frac{2\mu(1-\nu)}{1-2\nu}\left[\frac{\partial\tau_{yz}^P}{\partial\zeta} + \frac{\nu}{1-\nu}\left(\frac{\partial\tau_{yz}^Q}{\partial\xi} + \frac{\partial\tau_{yz}^R}{\partial\eta}\right)\right]\left(1 - \frac{x^2}{a_m^2} - \frac{y^2}{b_m^2}\right)^{1/2}$
$\boldsymbol{K_{mn}^{31}}$	$\mu\left[\frac{\partial\sigma_{zz}^P}{\partial\xi} + \frac{\partial\sigma_{zz}^Q}{\partial\zeta}\right]\left(1 - \frac{x^2}{a_m^2} - \frac{y^2}{b_m^2}\right)^{1/2}$
$\boldsymbol{K_{mn}^{32}}$	$\mu\left[\frac{\partial\sigma_{zz}^P}{\partial\eta} + \frac{\partial\sigma_{zz}^R}{\partial\zeta}\right]\left(1 - \frac{x^2}{a_m^2} - \frac{y^2}{b_m^2}\right)^{1/2}$
$\boldsymbol{K_{mn}^{33}}$	$\frac{2\mu(1-\nu)}{1-2\nu}\left[\frac{\partial\sigma_{zz}^P}{\partial\zeta} + \frac{\nu}{1-\nu}\left(\frac{\partial\sigma_{zz}^Q}{\partial\xi} + \frac{\partial\sigma_{zz}^R}{\partial\eta}\right)\right]\left(1 - \frac{x^2}{a_m^2} - \frac{y^2}{b_m^2}\right)^{1/2}$

Expressions for the Kernel matrix in Eq. (2-7) can be obtained *via* multiplication of Eq. (2-3) by the weighing function, as presented in Table 2.1, where a_{m} and b_{m} are the major and minor radii of the crack to which the m_{th} element belongs. The derivatives in their complete format are provided in Appendix A.

In addition, evaluation of the kernels requires the numerical integration of the expressions over the element where the IDLs are distributed. In cases where the evaluation point $(x^{\mathrm{n}}, y^{\mathrm{n}})$ lies outside of the integration area (*i.e.*, $n \neq m$), a conventional 2-D quadrature approach can be employed. On the other hand, in cases where $n = m$, such a technique is not applicable due to the presence of terms with third order singularity, for which a special procedure would be needed. In this study, the method proposed in [45] was adopted and successfully implemented. The sequence of equations in Eq. (2-7) can be solved using a standard solution routine to determine the unknown constants. The relative crack-face displacements for each element can be deduced using Eq. (2-5). Moreover, the SIFs for a target crack-front point can be established using the asymptotic relationship between relative crack-face displacement and SIFs. For elliptical cracks, dimensionless SIFs ($F_{\mathrm{I}}, F_{\mathrm{II}}, F_{\mathrm{III}}$) at a point $p(x_{\mathrm{p}}, y_{\mathrm{p}})$ along the crack-front can be determined by Eq. (2-8). Prior to using Eq. (2-8), f_{n} and f_{t} at point *p*, corresponding to the displacement discontinuities along the lines normal and tangential to the crack-front, should be evaluated using the equivalent values of f_1 and f_2, as well as a suitable vector transformation rule.

$$F_{\mathrm{I}}^{\mathrm{p}} = \frac{2\pi f_3^{\mathrm{p}}}{b}\left(\sin^2\beta + \frac{b^2}{a^2}\cos^2\beta\right)^{1/4} \tag{2-8a}$$

$$F_{\mathrm{II}}^{\mathrm{p}} = \frac{2\pi f_{\mathrm{n}}^{\mathrm{p}}}{b}\left(\sin^2\beta + \frac{b^2}{a^2}\cos^2\beta\right)^{1/4} \tag{2-8b}$$

$$F_{\mathrm{III}}^{\mathrm{p}} = \frac{2\pi f_{\mathrm{t}}^{\mathrm{p}}}{b}\left(\sin^2\beta + \frac{b^2}{a^2}\cos^2\beta\right)^{1/4} \tag{2-8c}$$

where,

$\tan\beta = \frac{a y_{\mathrm{p}}}{b x_{\mathrm{p}}}$; and $F_{\mathrm{I}}^{\mathrm{p}} = \frac{K_{\mathrm{I}}^{\mathrm{p}}}{\sigma_\infty\sqrt{\pi b}}$; $F_{\mathrm{II}}^{\mathrm{p}} = \frac{K_{\mathrm{II}}^{\mathrm{p}}}{\tau_\infty\sqrt{\pi b}}$; $F_{\mathrm{III}}^{\mathrm{p}} = \frac{K_{\mathrm{III}}^{\mathrm{p}}}{\tau_\infty\sqrt{\pi b}}$.

2.3 MATLAB code with illustrative example

In this section, a step-by-step guide to determine the SIFs of interacting cracks using the procedure and equations from previous section will be provided. The procedure includes four main stages, i.e., discretisation of the cracks, estimating the tractions at collocation points, calculation of kernel matrix and determination of SIFs. MATLAB codes that are needed to perform the analysis is developed and applied to the illustrative example. The complete codes are provided in Appendix B. By making the codes publicly available, the aim is to facilitate the adoption and further improvement of this powerful and versatile procedure by researchers and engineers.

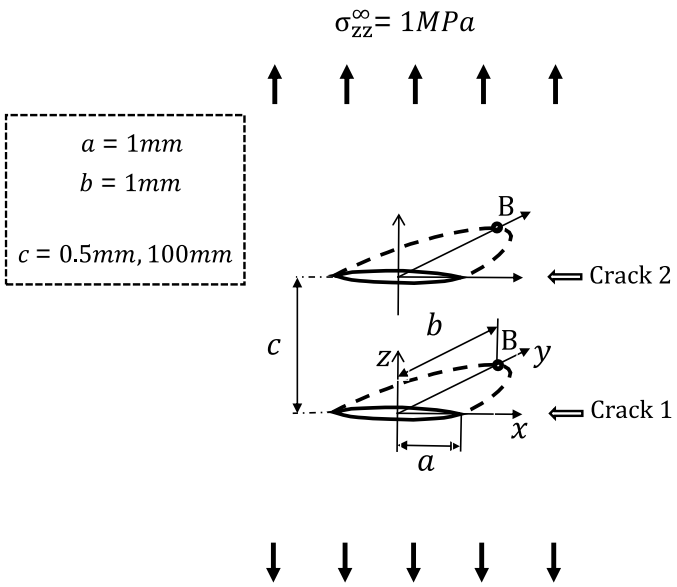

Fig. 2.5 Two similar, parallel, and aligned semi-elliptical surface cracks under tension loading.

Consider two similar semi-elliptical, parallel, and aligned cracks on the surface of an elastic body under tension loading shown in Fig. 2.5. The aim of the analysis is to determine the dimensionless SIFs at point B of the cracks when c = 0.5 mm and 100 mm. Numerical results

of the illustrative example for each of the four main stages, will be reported in the following sections.

2.3.1 Discretisation of the cracks

In this step, each of the crack is divided into a number of elements. EllipseMesh is a function that takes the ellipse dimension (a = MajorRadius, b = MinorRadius) and number of divisions (Num) as input and output necessary data of the elements (MESHdata). EllipseMesh divides the plane of a semi-elliptical crack into triangular segments. In this example, each of the cracks will be divided into 3 triangular segments. All points are expressed in the local coordinate system of the crack and can be easily expressed in the global coordinate system with the help of the crack's origin coordinates when required.

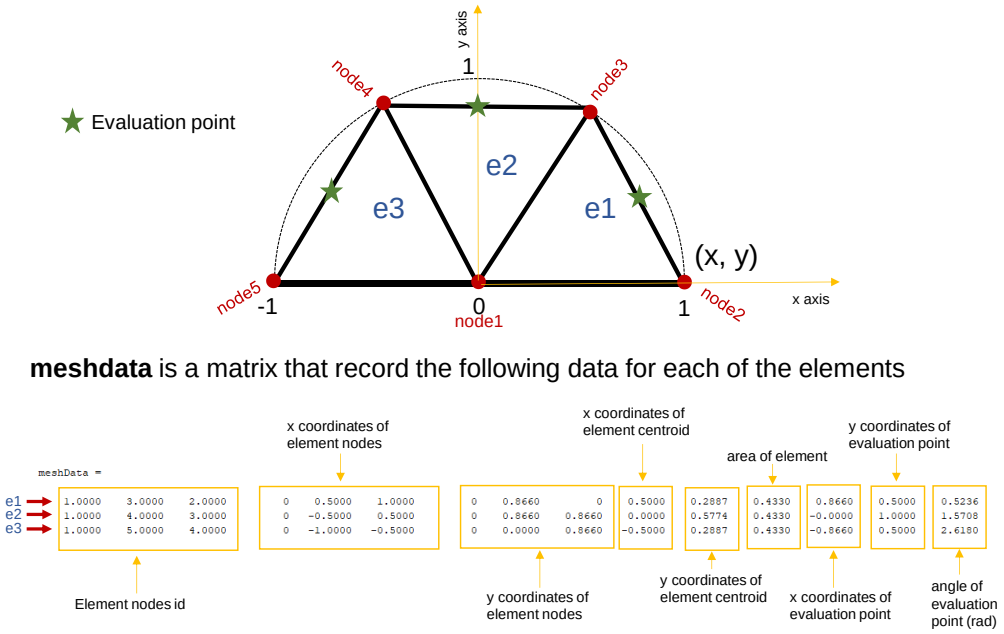

Fig. 2.6 Discretisation of the crack-faces into triangular segments.

The output, MESHdata, is therefore similar for both cracks. MESHdata is a matrix with number of rows equals number of divisions (Num, a row for each of the elements) and 15 columns. The associated data on each of the columns is presented in Fig.2.6. As the name implies, EllipseMesh is only suitable for discretising cracks that are semi-elliptical in shape, which is the focus of this study. For other shapes, another discretisation procedure is required.

2.3.2 Traction at collocation points

Another essential step is the computation of the stress components, σ_{zz}, τ_{xz} and τ_{yz} at the collocation points expressed in the local coordinate system of the corresponding crack. In this work, the centroid of the elements is chosen as the collocation point. In this example, the coordinate system of the 2 cracks corresponds to the global coordinate system. Therefore, the stress components at the collocation points are easily determined. In general cases, it will be necessary to transform the applied stresses, expressed in the global coordinate system, to the corresponding's local coordinate system using stress transformation equations. Stresses_ColloPoints is the MATLAB function that takes the number of collocation points, N_e (number of cracks x number of crack division, 6) and stress components of applied stress at infinity (σ_{zz}, τ_{xz}, τ_{yz}) as input. The output, SIGMA, is a (3 x 6) by 1 vector. In this example, the stress components at the collocation points are $\sigma_{zz} = 1$ MPa, $\tau_{xz} = 0$ and $\tau_{yz} = 0$. Therefore, the first 6 components of SIGMA vector are 1 and the remaining 12 components are 0.

2.3.3 Calculation of Kernel Matrix in the Main Function

Numerical evaluation of the kernel matrix *K*, in Eq. (2-7), is the most challenging aspect of the whole analysis. Calculation of the kernel matrix is performed as a sub-function in the main function. The sub-function is named Kmatrix and itself consists of other sub-functions that the program needs to perform multiple times. Developing the MATLAB code to evaluate the 9 components, K_{ij} of the matrix requires great care and precision. This is because the complete equations in appendix A must be expressed as a computer code.

Table 2.2 Component of Kernel matrix for Problem in Fig. 2.5.

c = 0.5 mm	c = 100 mm
$K^{33}_{mn} = \begin{bmatrix} -0.882 & 0.192 & 0.054 & -0.470 & 0.028 & 0.052 \\ 0.165 & -0.989 & 0.165 & 0.037 & -0.479 & 0.037 \\ 0.054 & 0.192 & -0.882 & 0.053 & 0.028 & -0.470 \\ -0.470 & 0.028 & 0.053 & -0.882 & 0.192 & 0.054 \\ 0.037 & -0.479 & 0.037 & 0.165 & -0.989 & 0.165 \\ 0.053 & 0.028 & -0.470 & 0.054 & 0.192 & -0.882 \end{bmatrix} \times 10^5$	$K^{33}_{mn} = \begin{bmatrix} -0.882 & 0.192 & 0.054 & 0 & 0 & 0 \\ 0.165 & -0.989 & 0.165 & 0 & 0 & 0 \\ 0.054 & 0.192 & -0.882 & 0 & 0 & 0 \\ 0 & 0 & 0 & -0.882 & 0.192 & 0.054 \\ 0 & 0 & 0 & 0.165 & -0.989 & 0.165 \\ 0 & 0 & 0 & 0.054 & 0.192 & -0.882 \end{bmatrix} \times 10^5$
$K^{32}_{mn} = \begin{bmatrix} 0 & 0 & 0 & 0.061 & 0.126 & 0.050 \\ 0 & 0 & 0 & -0.105 & 0 & 0.105 \\ 0 & 0 & 0 & -0.050 & -0.126 & -0.061 \\ -0.061 & -0.126 & -0.050 & 0 & 0 & 0 \\ 0.105 & 0 & -0.105 & 0 & 0 & 0 \\ 0.050 & 0.126 & 0.061 & 0 & 0 & 0 \end{bmatrix} \times 10^5$	$K^{32}_{mn} = \begin{bmatrix} 0 & 0 & 0 & 0 & 0 & 0 \\ 0 & 0 & 0 & 0 & 0 & 0 \\ 0 & 0 & 0 & 0 & 0 & 0 \\ 0 & 0 & 0 & 0 & 0 & 0 \\ 0 & 0 & 0 & 0 & 0 & 0 \\ 0 & 0 & 0 & 0 & 0 & 0 \end{bmatrix}$
$K^{31}_{mn} = \begin{bmatrix} 0 & 0 & 0 & 0.245 & 0.009 & 0.046 \\ 0 & 0 & 0 & 0.076 & 0.054 & 0.076 \\ 0 & 0 & 0 & 0.046 & 0.009 & 0.245 \\ -0.245 & -0.009 & -0.046 & 0 & 0 & 0 \\ -0.076 & -0.054 & -0.076 & 0 & 0 & 0 \\ -0.046 & -0.009 & -0.245 & 0 & 0 & 0 \end{bmatrix} \times 10^5$	$K^{31}_{mn} = \begin{bmatrix} 0 & 0 & 0 & 0 & 0 & 0 \\ 0 & 0 & 0 & 0 & 0 & 0 \\ 0 & 0 & 0 & 0 & 0 & 0 \\ 0 & 0 & 0 & 0 & 0 & 0 \\ 0 & 0 & 0 & 0 & 0 & 0 \\ 0 & 0 & 0 & 0 & 0 & 0 \end{bmatrix}$
$K^{23}_{mn} = \begin{bmatrix} 0 & 0 & 0 & 0.045 & 0.089 & 0.010 \\ 0 & 0 & 0 & -0.076 & 0 & 0.076 \\ 0 & 0 & 0 & -0.010 & -0.089 & -0.045 \\ -0.045 & -0.089 & -0.010 & 0 & 0 & 0 \\ 0.076 & 0 & -0.076 & 0 & 0 & 0 \\ 0.010 & 0.089 & 0.045 & 0 & 0 & 0 \end{bmatrix} \times 10^5$	$K^{23}_{mn} = \begin{bmatrix} 0 & 0 & 0 & 0 & 0 & 0 \\ 0 & 0 & 0 & 0 & 0 & 0 \\ 0 & 0 & 0 & 0 & 0 & 0 \\ 0 & 0 & 0 & 0 & 0 & 0 \\ 0 & 0 & 0 & 0 & 0 & 0 \\ 0 & 0 & 0 & 0 & 0 & 0 \end{bmatrix}$
$K^{22}_{mn} = \begin{bmatrix} -0.866 & 0.177 & 0.051 & 0.017 & -0.070 & -0.039 \\ 0.178 & -1.000 & 0.178 & -0.047 & 0.016 & -0.047 \\ 0.051 & 0.177 & -0.866 & -0.039 & -0.070 & 0.019 \\ 0.017 & -0.070 & -0.039 & -0.866 & 0.177 & 0.051 \\ -0.047 & 0.016 & -0.047 & 0.178 & -1.000 & 0.178 \\ -0.039 & -0.070 & 0.017 & 0.051 & 0.177 & -0.866 \end{bmatrix} \times 10^5$	$K^{22}_{mn} = \begin{bmatrix} -0.866 & 0.177 & 0.051 & 0 & 0 & 0 \\ 0.178 & -1.000 & 0.178 & 0 & 0 & 0 \\ 0.051 & 0.177 & -0.866 & 0 & 0 & 0 \\ 0 & 0 & 0 & -0.866 & 0.177 & 0.051 \\ 0 & 0 & 0 & 0.178 & -1.000 & 0.178 \\ 0 & 0 & 0 & 0.051 & 0.177 & -0.866 \end{bmatrix} \times 10^5$
$K^{21}_{mn} = \begin{bmatrix} 0.0004 & -0.022 & -0.043 & -0.017 & 0.015 & -0.030 \\ -0.007 & 0 & 0.007 & 0.080 & 0 & -0.080 \\ 0.043 & 0.022 & -0.0004 & 0.030 & -0.015 & 0.0173 \\ -0.017 & 0.015 & -0.030 & 0.0004 & -0.022 & -0.043 \\ 0.080 & 0 & -0.080 & -0.007 & 0 & 0.007 \\ 0.030 & -0.015 & 0.017 & 0.043 & 0.022 & -0.0004 \end{bmatrix} \times 10^5$	$K^{21}_{mn} = \begin{bmatrix} 0.0004 & -0.022 & -0.043 & 0 & 0 & 0 \\ -0.007 & 0 & 0.007 & 0 & 0 & 0 \\ 0.043 & 0.022 & -0.0004 & 0 & 0 & 0 \\ 0 & 0 & 0 & 0.0004 & -0.022 & -0.043 \\ 0 & 0 & 0 & -0.007 & 0 & 0.007 \\ 0 & 0 & 0 & 0.043 & 0.022 & -0.0004 \end{bmatrix} \times 10^5$
$K^{13}_{mn} = \begin{bmatrix} 0 & 0 & 0 & 0.081 & -0.033 & -0.009 \\ 0 & 0 & 0 & 0.034 & 0.052 & 0.034 \\ 0 & 0 & 0 & -0.009 & -0.033 & 0.081 \\ -0.081 & 0.033 & 0.009 & 0 & 0 & 0 \\ -0.034 & -0.052 & -0.034 & 0 & 0 & 0 \\ 0.009 & 0.033 & -0.081 & 0 & 0 & 0 \end{bmatrix} \times 10^5$	$K^{13}_{mn} = \begin{bmatrix} 0 & 0 & 0 & 0 & 0 & 0 \\ 0 & 0 & 0 & 0 & 0 & 0 \\ 0 & 0 & 0 & 0 & 0 & 0 \\ 0 & 0 & 0 & 0 & 0 & 0 \\ 0 & 0 & 0 & 0 & 0 & 0 \\ 0 & 0 & 0 & 0 & 0 & 0 \end{bmatrix}$
$K^{12}_{mn} = \begin{bmatrix} 0.009 & -0.017 & 0.016 & -0.018 & 0.030 & -0.017 \\ -0.014 & 0 & 0.014 & 0.069 & 0 & -0.069 \\ -0.016 & 0.017 & -0.009 & 0.017 & -0.030 & 0.018 \\ -0.018 & 0.030 & -0.017 & 0.009 & -0.017 & 0.016 \\ 0.069 & 0 & -0.069 & -0.014 & 0 & 0.014 \\ 0.017 & -0.030 & 0.018 & -0.016 & 0.017 & -0.009 \end{bmatrix} \times 10^5$	$K^{12}_{mn} = \begin{bmatrix} 0.009 & -0.017 & 0.016 & 0 & 0 & 0 \\ -0.014 & 0 & 0.014 & 0 & 0 & 0 \\ -0.016 & 0.017 & -0.009 & 0 & 0 & 0 \\ 0 & 0 & 0 & 0.009 & -0.017 & 0.016 \\ 0 & 0 & 0 & -0.014 & 0 & 0.014 \\ 0 & 0 & 0 & -0.016 & 0.017 & -0.009 \end{bmatrix} \times 10^5$
$K^{11}_{mn} = \begin{bmatrix} -0.632 & 0.171 & 0.027 & -0.152 & -0.029 & 0.010 \\ 0.230 & -0.973 & 0.230 & -0.062 & -0.040 & -0.062 \\ 0.027 & 0.171 & -0.632 & 0.010 & -0.029 & -0.152 \\ -0.152 & -0.029 & 0.010 & -0.632 & 0.171 & 0.027 \\ -0.062 & -0.040 & -0.062 & 0.230 & -0.973 & 0.230 \\ 0.010 & -0.029 & -0.152 & 0.027 & 0.171 & -0.632 \end{bmatrix} \times 10^5$	$K^{11}_{mn} = \begin{bmatrix} -0.632 & 0.171 & 0.027 & 0 & 0 & 0 \\ 0.230 & -0.973 & 0.230 & 0 & 0 & 0 \\ 0.027 & 0.171 & -0.632 & 0 & 0 & 0 \\ 0 & 0 & 0 & -0.632 & 0.171 & 0.027 \\ 0 & 0 & 0 & 0.230 & -0.973 & 0.230 \\ 0 & 0 & 0 & 0.027 & 0.171 & -0.632 \end{bmatrix} \times 10^5$

Furthermore, evaluation of the kernels includes numerical integration that require special procedure when the evaluation point lies inside of the integration area. This adds extra complexity to the evaluation of the kernel matrix. In fact, the bulk of the analysis time is spent in the computation of the kernel matrix. In this example, the kernel matrix is reported in Table 2.2.

For c = 100 mm, there is no interaction between the cracks and majority of the elements of kernel matrix are 0. Also, there is no coupling between the normal components of the Burger vector and shearing stresses induced on the slip plane. Therefore, the crack faces are only capable of Mode I displacement with corresponding K_{I}. When c = 0.5 mm, interaction occur between the two cracks. As a result, normal components of the Burger vectors induce shearing stresses on the slip plan and tangential components of the Burger vectors makes contribution to the normal stress on the slip plane. Kernel matrix elements influenced by the interaction effect is highlighted in red in Table 2.2. The coupling effect means that the cracks surfaces will experience all the three mode of displacements i.e., Mode I, II and III with corresponding K_{I}, K_{II} and K_{III} even though only tension loading is applied.

2.3.4 Calculation of SIFs in the Main Function

The last major step of the analysis is the computation of the dimensionless SIFs from the main function, SIFs_EllipticSurfaceCrack. This is possible after all the previous steps has been undertaken. The result of the piecewise constants for each elements are obtained by standard matrix solution routine in MATLAB and are reported in Table 2.3. Results of the dimensionless SIFs at point B for both cases are reported in Table 2.4.

For c = 100 mm, there is no interaction effect between the cracks because the two cracks are sufficiently far away from each other. Therefore, the applied tension loading will only result

to mode I deformation of the crack surfaces without mode II and III. This is why the dimensionless SIFs, $F_{\mathrm{I}}^{\mathrm{B}} = 0.6082$ and $F_{\mathrm{II}}^{\mathrm{B}} = F_{\mathrm{III}}^{\mathrm{B}} = 0$ at point B. It should be noted that the result of $F_{\mathrm{I}}^{\mathrm{B}}$ is 95% of the accurate result reported by Murakami [21], even though the number of division for each of the cracks is only 3. This shows that, using this method, very accurate result can be obtained with small number of divisions

Table 2.3 Piecewise constants for the crack elements for Problem in Fig. 2.5.

		c = 0.5 mm	c = 100 mm
f_3 of element 1 in crack 1	$f_3^{1,1}$	0.0585	0.0986
f_3 of element 2 in crack 1	$f_3^{2,1}$	0.0585	0.0986
f_3 of element 3 in crack 1	$f_3^{3,1}$	0.0585	0.0986
f_3 of element 1 in crack 2	$f_3^{1,2}$	0.0585	0.0986
f_3 of element 2 in crack 2	$f_3^{2,2}$	0.0585	0.0986
f_3 of element 3 in crack 2	$f_3^{3,2}$	0.0585	0.0986
f_2 of element 1 in crack 1	$f_2^{1,1}$	0.0083	0
f_2 of element 2 in crack 1	$f_2^{2,1}$	0	0
f_2 of element 3 in crack 1	$f_2^{3,1}$	-0.0083	0
f_2 of element 1 in crack 2	$f_2^{1,2}$	-0.0083	0
f_2 of element 2 in crack 2	$f_2^{2,2}$	0	0
f_2 of element 3 in crack 2	$f_2^{3,2}$	0.0083	0
f_1 of element 1 in crack 1	$f_1^{1,1}$	0.0103	0
f_1 of element 2 in crack 1	$f_1^{2,1}$	0.0126	0
f_1 of element 3 in crack 1	$f_1^{3,1}$	0.0103	0
f_1 of element 1 in crack 2	$f_1^{1,2}$	-0.0103	0
f_1 of element 2 in crack 2	$f_1^{2,2}$	-0.0126	0
f_1 of element 3 in crack 2	$f_1^{3,2}$	-0.0103	0

For c = 0.5 mm, there is interaction effect between the cracks. As a result, the crack surfaces can experience all the three more of deformation, even though the external loading is only tension load. The

results of dimensionless SIFs at point B are $F_{\mathrm{I}}^{\mathrm{B}} = 0.3694$, $F_{\mathrm{II}}^{\mathrm{B}} = 0.0789$ and $F_{\mathrm{III}}^{\mathrm{B}} = 0$. It should be noted that F_{III} is non-zero at other locations but B. The results shows that the interaction caused approximately 40% reduction in Mode I SIF reduced compared with the result when c = 100 mm and simultaneously the existence of Mode II SIF, $F_{\mathrm{II}}^{\mathrm{B}}$.

Table 2.4 Dimensionless SIFs at point B for Problem in Fig. 2.5.

		c = 0.5 mm	c = 100 mm
Dimensionless Mode I SIF at point B of crack 1	$F_{\mathrm{I}}^{\mathrm{B}}$	0.3694	0.6082
Dimensionless Mode II SIF at point B of crack 1	$F_{\mathrm{II}}^{\mathrm{B}}$	0.0789	0
Dimensionless Mode III SIF at point B of crack 1	$F_{\mathrm{III}}^{\mathrm{B}}$	0	0
Dimensionless Mode I SIF at point B of crack 2	$F_{\mathrm{I}}^{\mathrm{B}}$	0.3694	0.6082
Dimensionless Mode II SIF at point B of crack 2	$F_{\mathrm{II}}^{\mathrm{B}}$	0.0789	0
Dimensionless Mode III SIF at point B of crack 2	$F_{\mathrm{III}}^{\mathrm{B}}$	0	0

CHAPTER 3. SIF solutions of interacting semi-elliptical surface cracks

In this section, the afore-mentioned procedures are applied to some problems of practical importance. In all the examples, each crack was divided into nine segments, based on the pattern showcased in Fig. 2.4. This pattern and the number of divisions, obtained by trial and error, provided the best compromise between analysis time and accuracy. Analysis for one crack took about 5s on average when performed on a typical desktop computer with prevalent CPU (e.g., Intel(R) Core (TM) i3-8100 CPU 3.60 GHz), i.e., for n number of cracks, the analysis took approximately ($n \times 5$) s. A significant portion of the analysis time was used in the determination of the Kernel matrix in Eq. (2-7).

Several studies on the stress singularity at/near a corner point (i.e., a point where the crack-front intersects with the free surface) reported the effect of Poisson's ratio on the nature of singularity at the corner point [23, 26, 27, 50, 51]. They reported different form of stress singularities at the corner points depends on the value of the poisson ratio. Since such exceptional singularity behaviour at the corner point does not exist when $v = 0$, i.e., only the well-known elastic crack tip stress singularity, $r^{-0.5}$ exist [23, 26]. Furthermore, it was reported that the effect of Poisson ratio on SIFs is negligible outside the corner points. Therefore, Poisson's ratio, v, was set to zero for all the examples analyzed in this study. Zero Poisson's ratio brings additional advantage to the computation time because the other values ($v \neq 0$) led to an increase of approximately 1 s per crack in the analysis.

As will be demonstrated by the example of a semi-elliptical surface crack under tension, the accuracy of the analysis results for the proposed method is comparable to that of earlier works. In the following, the method's precision is first established for a semi-elliptical surface crack with various aspect ratios under tension. Subsequently, more complex examples will be

analysed (e.g., parallel arrays of surface cracks and randomly-distributed surface cracks under tension) and some interesting observations will be discussed.

3.1 Single semi-elliptical surface crack under tension

Fig. 3.1 portrays a single semi-elliptical surface crack under remote tension. In this case, Mode I SIFs, K_{IA}, at crack tip A, and K_{IB}, at the deepest point B, were analysed, where the crack aspect ratio, $\frac{b}{a}$, ranged from 0.1 to 10.

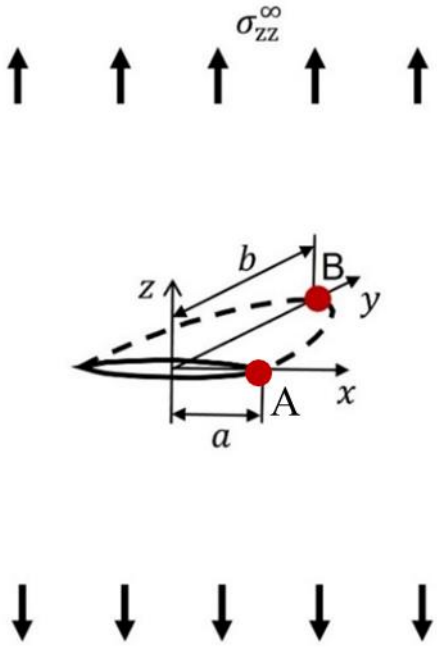

Fig. 3.1 Semi-elliptical surface crack under tension loading.

Table 3.1 Stress intensity factors for semi-elliptical surface cracks under tension loading.

b/a	$F_{IA} = K_{IA}/\sigma_{zz\infty}\sqrt{\pi a}$	$F_{IB} = K_{IB}/\sigma_{zz\infty}\sqrt{\pi b}$
0.1	0.355	1.096
0.5	0.517	0.864 (0.872*)
1	0.705 (0.713*)	0.656 (0.640*)
5	1.051	0.219
10	1.101	0.118

* Result obtained by Murakami [21]. In that study, Poisson's ratio was $\nu = 0.3$.

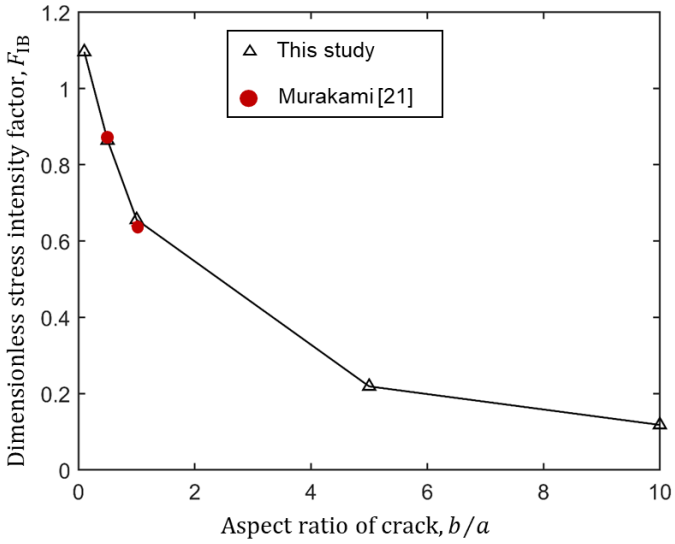

Fig. 3.2(a) Dimensionless Mode I SIF at problem point B in Fig. 3.1

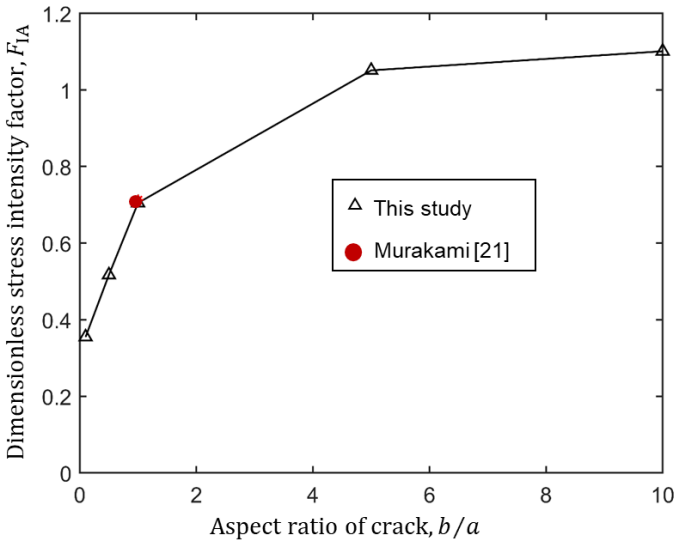

Fig. 3.2(b) Dimensionless Mode I SIF at problem point A in Fig. 3.1

The obtained dimensionless SIFs are listed in Table 3.1 and presented in Fig. 3.2. Where available, the values acquired by Murakami [21] are attached in parentheses for comparison purposes. In Murakami's analysis, Poisson's ratio was 0.3, while in this study it was set to zero,

a factor which may explain the difference between the results. Nevertheless, the variance was always less than 3%. The result indicates that the accuracy of this method is sufficient for practical applications.

3.2 Parallel semi-elliptical surface cracks under tension

Consider two parallel surface cracks, identical in both shape and dimensions, were considered under remote tension, as depicted in Fig. 3.3. This problem was first analysed by Isida et al. [41] using two similar cracks with $\frac{b}{a} \leq 1.0$ and $\frac{c}{b} \geq 1$. In this study, analysis was performed for $\frac{b}{a}$ ranging from 0.1 to 10 and $\frac{c}{b}$ ranging from 0.1 to 5.

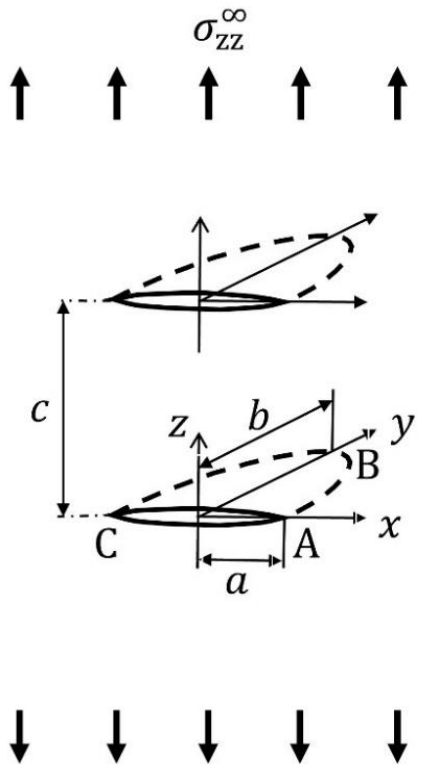

Fig. 3.3 Two parallel cracks under tension loading.

Table 3.2(a) documents the values of the interaction factor, γ_{B}, defined as the ratio of the dimensionless SIF at point B (i.e., crack-bottom) to that of a single crack under the same loading condition. These values are plotted in Fig. 3.4. The result indicates that an interaction of cracks led to the reduction in the Mode I SIF. The interaction effect depended on the aspect ratio of the cracks. A shallower crack tended to demonstrate a greater interaction effect; however, as the two cracks got very close, the aspect ratio dependence appeared to diminish. Furthermore, the existence of K_{II} and K_{III} was confirmed in this example. Table 3.2(b) lists the dimensionless Mode II SIF, $F_{\mathrm{II}}^{\mathrm{B}}$, at point B. In most cases, the K_{II} and K_{III} values were insignificant when compared with K_{I}.

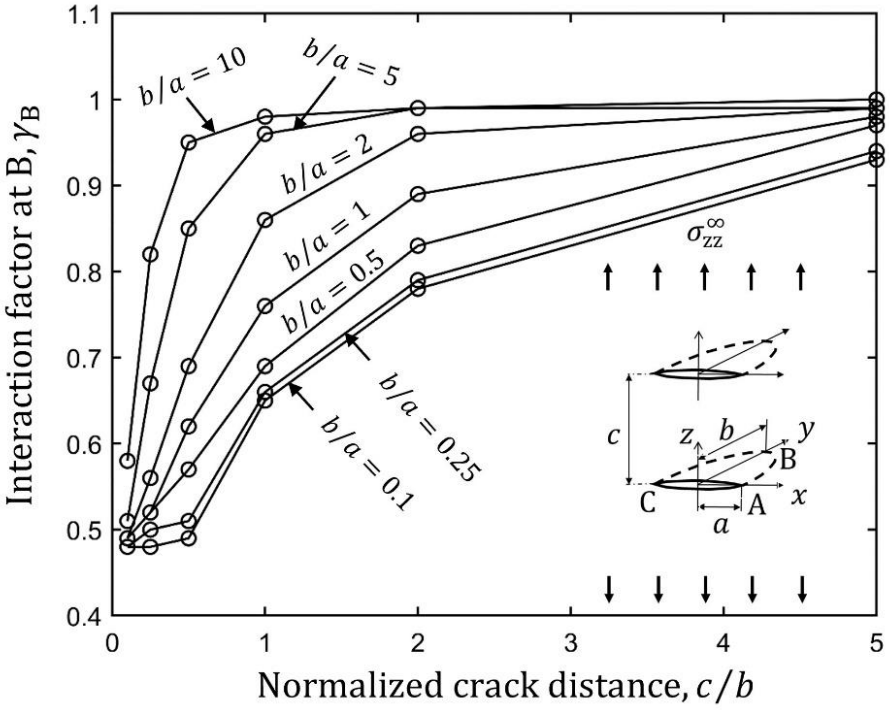

Fig. 3.4 Interaction factors at problem point B in Fig. 3.3

Consequently, the Mode II and III SIFs are not expected to affect the fracture strength (e.g., fatigue strength) in practical problems but could play a major role in the determination of crack-growth direction. However, Modes II and III SIFs showed considerable increase for very

shallow cracks, as noted in Table 3.2(b). For example, when $\frac{b}{a}$ = 0.1 and $\frac{c}{b}$ = 0.5, $F_{\mathrm{II}}^{\mathrm{B}}$ = 0.27 and $F_{\mathrm{I}}^{\mathrm{B}}$= 0.49. In this case, $F_{\mathrm{II}}^{\mathrm{B}}$ was about 55% of $F_{\mathrm{I}}^{\mathrm{B}}$ and might therefore no longer be negligible in fracture strength assessment. Moreover, this type of Mode I crack interaction can play a positive role for fracture strength as compared to the case of a single crack [38, 52].

Table 3.2(a) The γ_{B} for two similar and parallel, semi-elliptical surface cracks under tension loading.

c/b \ b/a	0.1 (1.096)	0.25 (1.026)	0.5 (0.864)	1 (0.656)	2 (0.439)	5 (0.219)	10 (0.118)
5	0.93	0.94	0.97	0.98	0.99	0.99	1.00
2	0.78	0.79	0.83	0.89	0.96	0.99	0.99
1	0.65	0.66	0.69	0.76	0.86	0.96	0.98
0.5	0.49	0.51	0.57	0.62	0.69	0.85	0.95
0.25	0.48	0.50	0.52	0.52	0.56	0.67	0.82
0.1	0.48	0.48	0.49	0.49	0.49	0.51	0.58

Table 3.2(b) The $F_{\mathrm{II}}^{\mathrm{B}}$ for two similar and parallel, semi-elliptical surface cracks under tension loading.

c/b \ b/a	0.1	0.25	0.5	1	2	5	10
5	0.018	0.014	0.007	0.002	0.001	0.000	0.000
2	0.106	0.095	0.064	0.028	0.008	0.001	0.000
1	0.190	0.170	0.126	0.072	0.029	0.003	0.001
0.5	0.272	0.241	0.149	0.093	0.043	0.008	0.002
0.25	0.161	0.112	0.073	0.088	0.036	0.009	0.003
0.1	0.101	0.043	0.029	0.014	0.026	0.002	0.001

A natural extension of the problem in Fig. 3.3 is the case where there are more than two similar, parallel, and aligned surface cracks under remote tension. The results of such investigations will be useful in addressing practical fracture problems related to surface roughness due to manufacturing methods such as machining and additive manufacturing. Analyses were performed for *N*, an odd number of parallel and aligned surface cracks under tension (as shown in Fig. 3.5) for different combinations of $\frac{c}{b}$ and $\frac{b}{a}$ ratios, with emphasis on the interaction effects of the outermost and middle cracks.

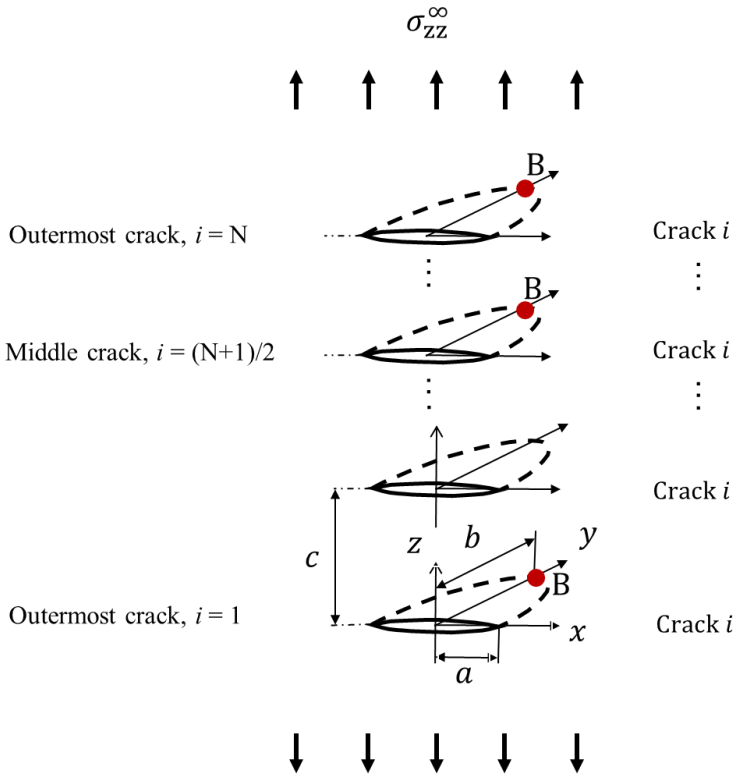

Fig. 3.5 *N* number of parallel cracks under tension loading.

Table 3.3 details the dimensionless SIFs and interaction factors, γ_B at point B. When available, the results from the study by Isida et al. [41] are provided in parentheses for comparison. It is noteworthy to highlight that in the Isida study, Poisson's ratio was set to 0.3 while it was fixed at zero in this study, perhaps the reason for the variation in results. Notwithstanding, for all practical purposes, the disparity appears to be minor. The obtained γ_B

values are shown in Fig. 3.6. In all cases, the γ_B of the middle crack (dashed line) was always lower than that of the outermost crack (solid line). For a constant $\frac{c}{b}$ ratio, the difference in γ_B values between the outermost and middle crack were dependent on the aspect ratio.

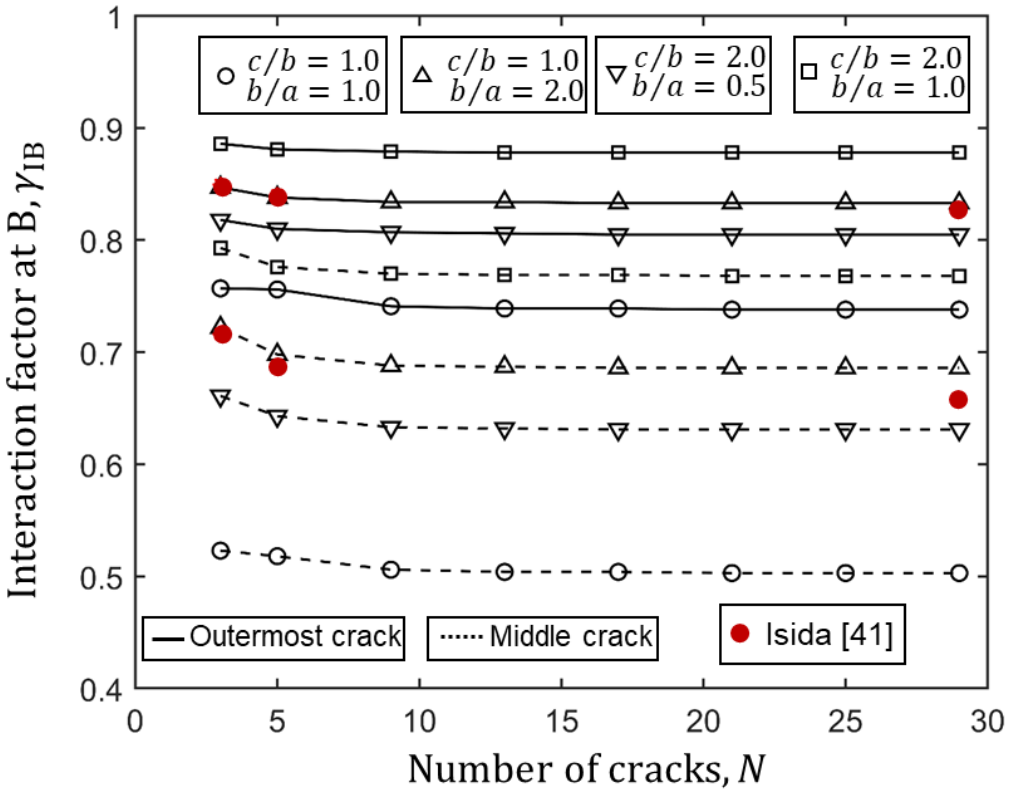

Fig. 3.6 Interaction factors at point B.

In addition, the degree of interaction was minimally affected by the number of cracks, N. In fact, in all the cases analysed, the γ_B was almost constant for $N \geq 5$. The result suggests that analytical and experimental studies of this nature can be executed with five cracks and the outcomes would be equally applicable to a larger number of cracks. This will lead to considerable savings insofar as effort and resources are concerned.

3.3 Two parallel non-aligned cracks of identical shape but different sizes under tension

In the previous example, two parallel interacting cracks were of the same shape and size while the distance between the cracks varied. The cracks were also perfectly aligned perpendicular to the loading direction. However, in reality, many practical problems involve parallel interacting cracks that are not necessarily of the same size and most probably not aligned.

Table 3.3 The F_{I} and γ_{B} for *N* similar and parallel, semi-elliptical surface cracks under tension loading.

		N	$F_{\mathrm{IB}}^{\mathrm{outermost}}$	$F_{\mathrm{IB}}^{\mathrm{middle}}$	$\gamma_{\mathrm{B}}^{\mathrm{outermost}}$	$\gamma_{\mathrm{B}}^{\mathrm{middle}}$
$\frac{c}{b}=1.0$	$\frac{b}{a}=1.0$	3	0.496	0.343	0.757	0.523
		5	0.489	0.340	0.756	0.518
		9	0.486	0.332	0.741	0.506
		13	0.485	0.331	0.739	0.504
		17	0.485	0.330	0.739	0.504
		21	0.484	0.330	0.738	0.503
		25	0.484	0.330	0.738	0.503
		29	0.484	0.330	0.738	0.503
	$\frac{b}{a}=2.0$	3	0.372	0.317	0.847	0.722
		5	0.368	0.307	0.838	0.698
		9	0.366	0.302	0.834	0.688
		13	0.366	0.302	0.834	0.687
		17	0.366	0.301	0.833	0.686
		21	0.366	0.301	0.833	0.686
		25	0.366	0.301	0.833	0.686
		29	0.366	0.301	0.833	0.686
$\frac{c}{b}=2.0$	$\frac{b}{a}=0.5$	3	0.707 (0.734*)	0.571 (0.619*)	0.818	0.661
		5	0.700 (0.726*)	0.555 (0.593*)	0.810	0.643
		9	0.697	0.547	0.807	0.633
		13	0.696	0.546	0.806	0.632
		17	0.696	0.545	0.805	0.631
		21	0.696	0.545	0.805	0.631
		25	0.696	0.545	0.805	0.631
		29	0.695 (0.714*)	0.545 (0.568*)	0.805	0.631
	$\frac{b}{a}=1.0$	3	0.581	0.520	0.886	0.793
		5	0.578	0.509	0.881	0.776
		9	0.577	0.505	0.879	0.770
		13	0.576	0.504	0.878	0.769
		17	0.576	0.504	0.878	0.769
		21	0.576	0.504	0.878	0.768
		25	0.576	0.504	0.878	0.768
		29	0.576	0.504	0.878	0.768

* Result obtained by Isida *et al.* [41]. In that study, Poisson's ratio was $\nu = 0.3$.

In this example, two interacting, parallel surface cracks of similar shape but different sizes under tension were investigated, as well as the effect of non-alignment of the cracks (cf. Fig. 3.7). The distance between the two cracks in the loading direction was fixed to 125% of the minor radius of Crack 2.

The result for the dimensionless SIFs at points A, B and C, and interaction factors for both cracks, are reported in Tables 3.4(a), 3.4(b) and 3.4(c) for α = 0, α = 0.5 and α = 1.0, respectively. The obtained interaction factors, $\gamma_{B,1}$ and $\gamma_{B,2}$, are correspondingly presented in Fig. 3.8(a) and 3.8(b). The effect of the difference in size of two interacting geometrically-similar cracks could clearly be seen. The interaction effect was more significant in the smaller crack (Crack 2) than in the larger crack (Crack 1). In all of the cases, as α increased from 0 to 1, the nature of the interaction effect changed from reduction to amplification.

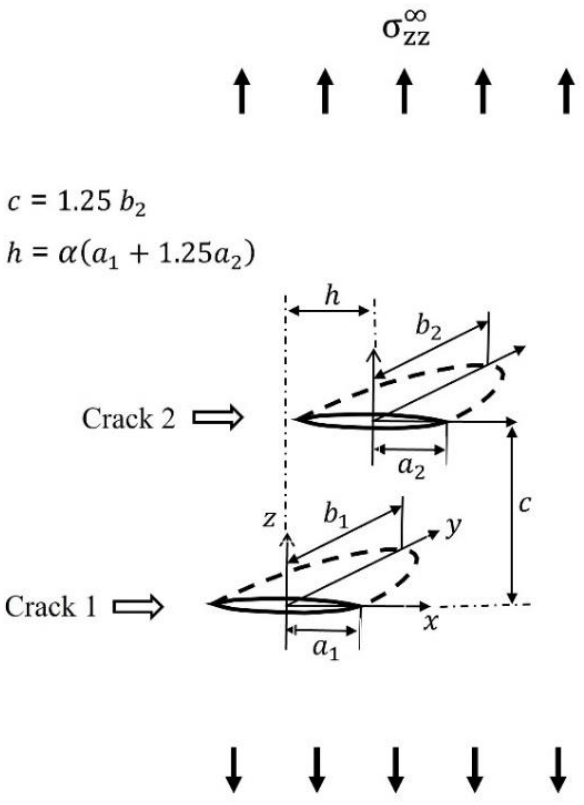

Fig. 3.7 Two staggered cracks under tension loading

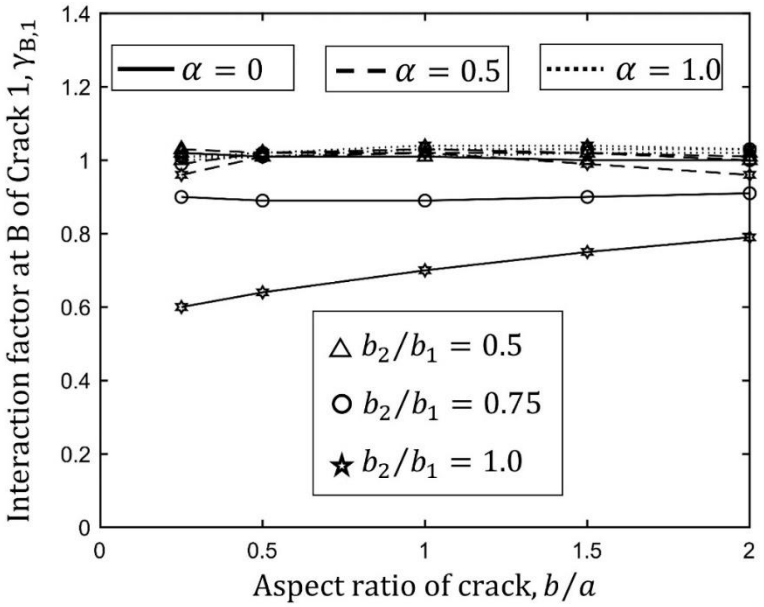

Fig. 3.8(a) Interaction factor at problem point *B* of Crack 1 in Fig. 3.7

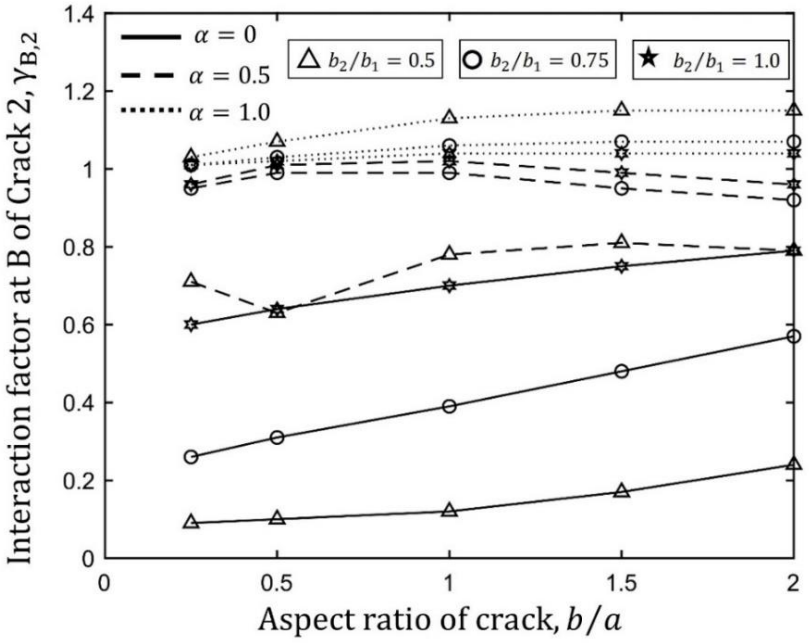

Fig. 3.8(b) Interaction factor at problem point B of Crack 2 in Fig. 3.7

Table 3.4(a) The F_{I} , γ_{A} , γ_{B} and γ_{C} for two staggered, semi-elliptical surface cracks under tension loading. $\alpha = 0$

b_2/b_1	b/a	F_{IA_1}	F_{IB_1}	F_{IC_1}	F_{IA_2}	F_{IB_2}	F_{IC_2}	γ_{A_1}	γ_{B_1}	γ_{C_1}	γ_{A_2}	γ_{B_2}	γ_{C_2}
0.5	0.25	0.47	1.04	0.47	0.00	0.09	0.00	1.01	1.02	1.01	0.002	0.09	0.00
	0.5	0.52	0.87	0.52	0.02	0.09	0.02	1.01	1.01	1.01	0.03	0.10	0.03
	1.0	0.71	0.66	0.71	0.06	0.08	0.06	1.00	1.01	1.00	0.09	0.12	0.09
	1.5	0.82	0.53	0.82	0.14	0.09	0.14	0.99	1.00	0.99	0.17	0.17	0.17
	2.0	0.89	0.44	0.89	0.23	0.11	0.23	0.99	1.00	0.99	0.26	0.24	0.26
0.75	0.25	0.42	0.92	0.42	0.04	0.27	0.04	0.91	0.90	0.91	0.09	0.26	0.09
	0.5	0.46	0.77	0.46	0.10	0.27	0.10	0.89	0.89	0.89	0.19	0.31	0.19
	1.0	0.62	0.59	0.62	0.25	0.26	0.25	0.88	0.89	0.88	0.35	0.39	0.35
	1.5	0.73	0.48	0.73	0.40	0.26	0.40	0.89	0.90	0.89	0.48	0.48	0.48
	2.0	0.80	0.40	0.80	0.52	0.25	0.52	0.89	0.91	0.89	0.57	0.57	0.57
1.0	0.25	0.24	0.62	0.24	0.24	0.62	0.24	0.51	0.60	0.51	0.51	0.60	0.51
	0.5	0.30	0.56	0.30	0.30	0.56	0.30	0.57	0.64	0.57	0.57	0.64	0.57
	1.0	0.47	0.46	0.47	0.47	0.46	0.47	0.67	0.70	0.67	0.67	0.70	0.67
	1.5	0.61	0.40	0.61	0.61	0.40	0.61	0.74	0.75	0.74	0.74	0.75	0.74
	2.0	0.70	0.35	0.70	0.70	0.35	0.70	0.78	0.79	0.78	0.78	0.79	0.78

Table 3.4(b) The F_{I} , γ_{A} , γ_{B} and γ_{C} for two staggered, semi-elliptical surface cracks under tension loading. $\alpha = 0.5$

b_2/b_1	b/a	F_{IA_1}	F_{IB_1}	F_{IC_1}	F_{IA_2}	F_{IB_2}	F_{IC_2}	γ_{A_1}	γ_{B_1}	γ_{C_1}	γ_{A_2}	γ_{B_2}	γ_{C_2}
0.5	0.25	0.53	1.06	0.47	0.54	0.73	0.03	1.15	1.03	1.01	1.18	0.71	0.06
	0.5	0.55	0.88	0.52	0.63	0.55	0.07	1.06	1.02	1.01	1.22	0.63	0.14
	1.0	0.62	0.67	0.71	0.81	0.51	0.29	0.89	1.02	1.01	1.14	0.78	0.41
	1.5	0.70	0.54	0.84	0.87	0.43	0.43	0.85	1.02	1.02	1.06	0.81	0.52
	2.0	0.78	0.45	0.91	0.89	0.35	0.51	0.87	1.01	1.02	0.99	0.79	0.57
0.75	0.25	0.40	1.02	0.46	0.47	0.98	0.12	0.86	0.99	1.00	1.02	0.95	0.25
	0.5	0.43	0.88	0.52	0.55	0.86	0.23	0.83	1.02	1.01	1.06	0.99	0.45
	1.0	0.55	0.68	0.73	0.77	0.65	0.42	0.78	1.03	1.03	1.09	0.99	0.60
	1.5	0.66	0.54	0.85	0.87	0.50	0.55	0.80	1.02	1.03	1.05	0.95	0.67
	2.0	0.74	0.44	0.92	0.90	0.40	0.63	0.83	1.00	1.02	1.00	0.92	0.70
1.0	0.25	0.28	0.99	0.46	0.46	0.99	0.28	0.59	0.96	1.00	1.00	0.96	0.59
	0.5	0.35	0.88	0.53	0.53	0.88	0.35	0.70	1.01	1.02	1.02	1.01	0.70
	1.0	0.51	0.67	0.74	0.74	0.67	0.51	0.72	1.02	1.04	1.04	1.02	0.72
	1.5	0.63	0.52	0.85	0.85	0.52	0.63	0.76	0.99	1.03	1.03	0.99	0.76
	2.0	0.71	0.42	0.90	0.90	0.42	0.71	0.79	0.96	1.00	0.99	0.96	0.79

Table 3.4(c) The F_{I} , γ_{A} , γ_{B} and γ_{C} for two staggered, semi-elliptical surface cracks under tension loading. $\alpha = 1.0$

b_2/b_1	b/a	F_{IA_1}	F_{IB_1}	F_{IC_1}	F_{IA_2}	F_{IB_2}	F_{IC_2}	γ_{A_1}	γ_{B_1}	γ_{C_1}	γ_{A_2}	γ_{B_2}	γ_{C_2}
0.5	0.25	0.46	1.03	0.46	0.47	1.05	0.49	1.01	1.00	1.00	1.02	1.03	1.05
	0.5	0.53	0.87	0.52	0.54	0.92	0.59	1.02	1.01	1.00	1.04	1.07	1.13
	1.0	0.74	0.66	0.71	0.77	0.74	0.86	1.05	1.01	1.01	1.09	1.13	1.22
	1.5	0.86	0.54	0.84	0.93	0.61	0.99	1.05	1.02	1.02	1.12	1.15	1.20
	2.0	0.93	0.45	0.91	1.01	0.50	1.04	1.04	1.02	1.02	1.13	1.15	1.16
0.75	0.25	0.47	1.03	0.46	0.47	1.04	0.48	1.01	1.01	1.00	1.01	1.01	1.03
	0.5	0.54	0.88	0.52	0.53	0.89	0.56	1.04	1.01	1.01	1.02	1.03	1.08
	1.0	0.75	0.67	0.72	0.74	0.70	0.79	1.06	1.03	1.02	1.05	1.06	1.12
	1.5	0.87	0.54	0.85	0.87	0.57	0.90	1.05	1.03	1.03	1.06	1.07	1.10
	2.0	0.92	0.45	0.92	0.95	0.47	0.95	1.03	1.03	1.03	1.06	1.07	1.06
1.0	0.25	0.47	1.03	0.46	0.46	1.03	0.47	1.02	1.01	1.00	1.00	1.01	1.02
	0.5	0.54	0.88	0.52	0.52	0.88	0.54	1.05	1.02	1.01	1.01	1.02	1.05
	1.0	0.75	0.68	0.73	0.73	0.68	0.75	1.07	1.04	1.03	1.03	1.04	1.07
	1.5	0.86	0.55	0.85	0.85	0.55	0.86	1.05	1.04	1.03	1.03	1.04	1.05
	2.0	0.91	0.45	0.93	0.93	0.46	0.92	1.02	1.03	1.03	1.03	1.04	1.02

The aspect ratio of the interacting cracks also influenced the interaction factors. In general, the nature of the interaction effect (reduction or amplification) is dependent on both the size difference and relative positions of the cracks. Based on these observations, the general perception that the interaction of two parallel and aligned cracks under tension always leads to a reduction in SIF is only valid for cracks that are geometrically similar and identical in size.

3.4 Random array of semi-elliptical surface cracks under tension

Previous examples have demonstrated the factors affecting the interaction of two cracks in proximity. However, in many practical cases, there are usually more than two cracks that form a colony, with all cracks interacting together. For example, multiple fatigue cracks initiate from surface defects during the fracture process of additively-manufactured components and cast parts. Corrosion fatigue applications are also similar examples of interaction between more than two surface cracks. In this sub-section, the combined interaction effect of surrounding cracks on a main crack is investigated. In Fig. 3.9, the main crack (Crack 1) surrounded by six neighbouring cracks was subjected to tensile loading.

The aspect ratios of the cracks and their relative positions are indicated in Fig. 3.9. The aim of the investigation was to study the interaction effect of the surrounding cracks on K_{I} of Crack 1 at points A, B and C. Firstly, each surrounding crack was paired with Crack 1, then all seven cracks were examined together. The results are reported in Table 3.5. The results revealed that due to the interaction effect of the surrounding cracks, K_{I} at points A and C of Crack 1 was no longer the same, thus predicting different crack behaviour at both ends in terms

of crack propagation or arrest. While the interaction effect gave rise to a 95% reduction in K_{I} at point A, it provoked an increase of about 9% in K_{I} at point C of Crack 1.

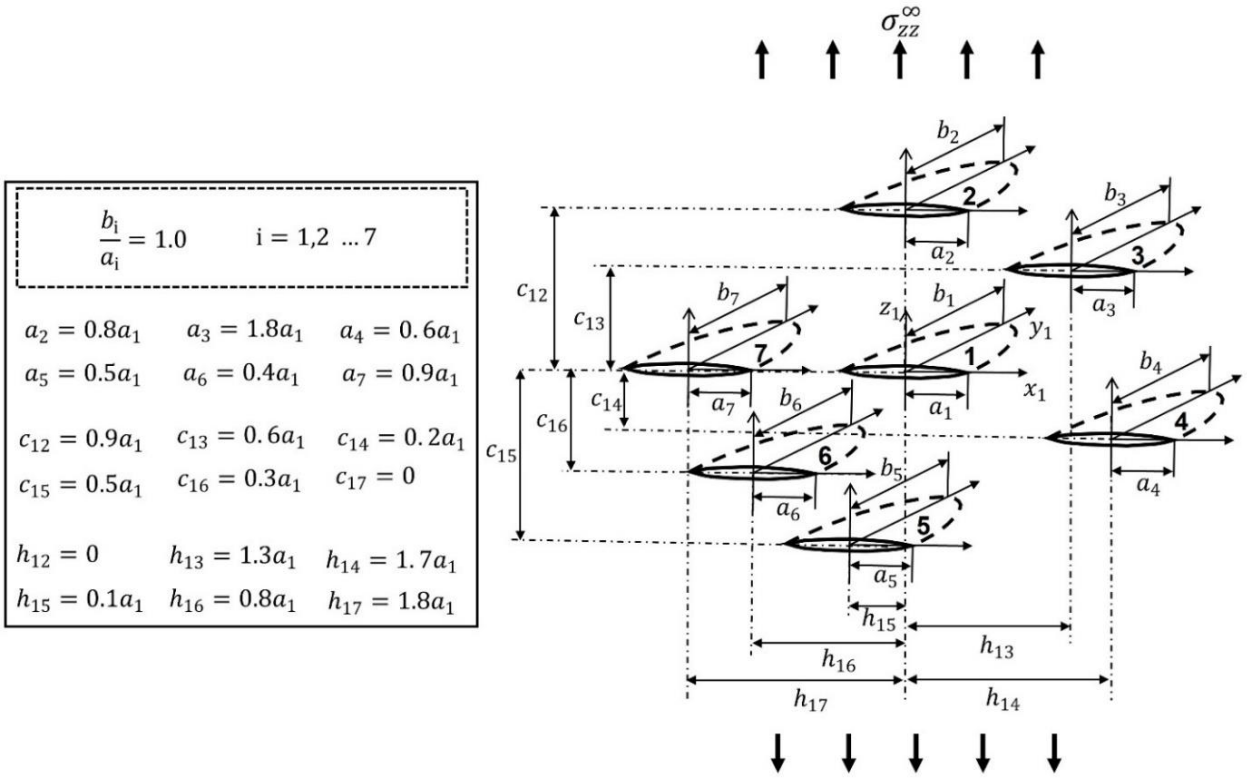

Fig. 3.9 Influence of six surrounding cracks on a main crack under tension loading.

Table 3.5 Interaction factors, γ_{A} , γ_{B} and γ_{C} for Crack 1 with surrounding cracks.

	γ_{IA}^{1}	γ_{IB}^{1}	γ_{IC}^{1}
Crack 1 and 2 only	0.86	0.87	0.86
Crack 1 and 3 only	0.36	0.65	1.14
Crack 1 and 4 only	1.08	1.02	1.02
Crack 1 and 5 only	1.00	0.99	0.98
Crack 1 and 6 only	1.01	1.01	0.97
Crack 1 and 7 only	1.05	1.06	1.25
All cracks	0.05	0.54	1.09

This suggests the likely possibility of crack arrest at point A due to the presence of the surrounding cracks, whereas the growth rate of the crack-tip at point C would have been greater than that of an isolated crack of the same size and loading condition. Furthermore, this example illustrates that all the surrounding cracks contributed to the interaction effects on the main cracks, the degree of which varied depending on their relative sizes, aspect ratios and distances. In this case, Crack 3 appears to have had the greatest influence on the interaction effect, but this cannot easily be predicted prior to the analysis. It should be noted that the blueprint for designing this example was re-constructed from an actual crack colony observed in a corrosion fatigue test reported by Kitagawa et al. [10], i.e., the locations and sizes of the cracks were measured directly according to their experimental results. For simplicity, the aspect ratio of every crack was assumed to be 1.0 because it was not reported in [10]. Assuming an aspect ratio of 1.0 is a common practise when such information cannot be estimated otherwise. Therefore, the conclusions discussed above is valid only for this particular example and should not be generalized. Nevertheless, similar study can be performed for distributed cracks with different aspect ratios.

CHAPTER 4. Characterisation of spatial distribution of surface defects

4.1 Background

In Chapter 3, it was demonstrated that when multiple cracks exist in colony, the resulting interaction effect is governed by the sizes of the cracks as well as their relative locations. There are many statistical techniques to characterise the size distribution of cracks, and some have been implemented in IDMs. On the other hand, there is no established techniques to characterise the relative locations of the cracks. The reason for lack of research in this area is because IDMs typically focus attention on interaction effect between two cracks and for those cases, there is no need for characterisation of the spatial distribution of the cracks.

In practical situation, interaction often occur among multiple distributed cracks. Therefore, in other to accurately include interaction effect in multiple crack problem, it is necessary to study suitable procedures for the quantitative characterisation of the spatial distribution of cracks. Furthermore, predictive IDMs require characteristics properties of the cracks, such as their initial sizes and initiation locations, to be known beforehand. Since cracks usually initial from pre-existing defects in the structure, it is possible to use the spatial arrangement of the pre-existing defects as a blueprint for the crack's initiation points.

In this chapter, investigation will be carried out for two Nearest Neighbour Analysis (NNA)-based procedures as suitable statistical tools to quantitatively characterise the spatial distribution of cracks, defects, or inclusions (henceforth collectively refer to as "defects"). The validity of this approach will be checked with experiment data obtained from a medium-carbon steel, previously exposed to a corrosive environment.

4.2 Theoretical formulation

4.2.1 Classification of spatial arrangement of defects

During the 1940s, NNA was developed as a practical tool for characterizing population patterns, propelled by research into the spatial distribution of plants or animals in their natural habitats [74]. The discovery that most populations are not arbitrarily distributed advanced the need for further research, to abandon the simple assumption of haphazard arrangement and to consider the degree of departure from arbitrary distribution [74]. Subsequently, NNA was successfully applied in the fields of materials science, medicine, astronomy, machine-learning, biology, and many other disciplines, generally targeted towards the realistic problems associated with the spatial arrangement of certain members of a given population. For example, Shehata and Boyd [75] applied an NNA-based procedure to compare the spatial distribution of non-metallic inclusions on the surfaces of as-cast and as-rolled steels.

The NNA-based method for characterizing the spatial distribution of feature-centroids in planes is herein provided. More complete details can be reviewed in the original publications [74, 76]. Clark and Evans [74] were the first to derive the formulae for calculation of the expected mean, $E(\bar{r}_1)$, and variance of the nearest distance, $E({s_1}^2)$, based on the features of a population, *N*, being randomly distributed over an area, *A*, with a distance measurement, r_1 , from each feature to its nearest neighbour. When the spatial distribution of features can be considered as homogeneous, the Poisson-point process, with a density of $\rho = \frac{N}{A}$, $E(\bar{r}_1)$ and $E({s_1}^2)$, are expressed by the following equations:

$$E(\bar{r}_1) = \frac{1}{2\sqrt{\rho}} \tag{4-1}$$

$$E({s_1}^2) = \frac{4-\pi}{4\pi} \cdot \frac{1}{\rho} \tag{4-2}$$

where, the observed mean, $\bar{r}_1$, and the variance of r_1, ${s_1}^2$, are formulated as follows:

$$\bar{r}_1 = \frac{\sum r_1}{N} \quad (4\text{-}3)$$

$$s_1{}^2 = \frac{\sum (r_1 - \bar{r}_1)^2}{N} \quad (4\text{-}4)$$

Using Equations (4-1)~(4-4), a simple method for categorizing the spatial distribution of a plane's features can be derived as follows: If Q is defined as the ratio of the observed and expected means, $Q = \bar{r}_1 / E(\bar{r}_1)$, with R being the ratio of observed and expected variance, $R = s_1{}^2 / E(s_1{}^2)$. The featured populations can be classified as random, regular, or clustered sets, or as clusters superimposed onto random backgrounds, via the following associations of *Q* and *R*:

- Random sets $Q = 1, \quad R = 1$
- Regular sets $Q > 1, \quad R \ll 1$
- Clustered sets $Q < 1, \quad R < 1$
- Clustered, with a superimposed background $Q < 1, \quad R > 1$

If the Q value indicates a non-random distribution of a set (*i.e.*, $Q \neq 1$), it then becomes necessary to measure the relevance of the $\bar{r}_1$ departure from $E(\bar{r}_1)$, to quantify the reliability of this procedure. Clark and Evans [74] also developed a significance test based on the normal curve. In an arbitrarily distributed population with the same ρ and N as those of the observed population, the equation for calculating the standard error of mean distance to the nearest neighbour, $\sigma_{E(\bar{r}_1)}$, is provided as follows:

$$\sigma_{E(\bar{r}_1)} = \frac{0.26136}{\sqrt{N\rho}} \quad (4\text{-}5)$$

Then, the standard variant of the normal curve, c, is offered by the ensuing equation:

$$c = \frac{\bar{r}_1 - E(\bar{r}_1)}{\sigma_{E(\bar{r}_1)}} \quad (4\text{-}6)$$

Using the calculated c value, in combination with a suitable table for normal distribution, the level of significant deviation can thus be established. In this study, to differentiate between the afore-mentioned procedure and other distance-based methods (*e.g.*, the Ripley, Brix, $\hat{L}$ estimator, Inter-event distance estimator, it is labelled herein, the QR method. Compared to others, key advantages of the QR method include its simplicity, ease of interpretation and quantitative incorporation of the degree of departure from random distribution.

4.2.2 Separation of clustered defects from background set

Schwarz and Exner [76] developed a procedure for separating cases where feature-populations involved clusters with overlapping backgrounds. By considering a compound set to comparably be an overlay of a very dense, Poisson-point process (cluster-sets) and a relatively less-dense, homogenous Poisson-point method (background-sets), a practical and simple rule was developed to determine which feature belonged to either the cluster- or background-sets. According to that procedure, ${r_1}^*$ and ${r_2}^*$ were defined by the successive equations:

$${r_1}^* = \left[\frac{1}{\pi(\rho_{c1}-\rho_{b1})} ln\left(\frac{c_1}{1-c_1}\cdot\frac{\rho_{c1}}{\rho_{b1}}\right)\right]^{1/2} \quad (4\text{-}7)$$

$${r_2}^* = \left[\frac{1}{\pi(\rho_{c2}-\rho_{b2})} ln\left(\frac{c_2}{1-c_2}\cdot\frac{{\rho_{c2}}^2}{{\rho_{b2}}^2}\right)\right]^{1/2} \quad (4\text{-}8)$$

where, $c_1, \rho_{c1}, \rho_{b1}$ and $c_2, \rho_{c2}, \rho_{b2}$ are obtained from the complete solution of Equation (4-9) and (4-10), accordingly:

$$\frac{c_1}{\sqrt{\rho_{c1}}} + \frac{1-c_1}{\sqrt{\rho_{b1}}} = 2M_1^1 \quad (4\text{-}9a)$$

$$\frac{c_1}{\rho_{c1}} + \frac{1-c_1}{\rho_{b1}} = \pi M_2^1 \quad (4\text{-}9b)$$

$$\frac{c_1}{\sqrt{\rho_{c1}{}^3}} + \frac{1-c_1}{\sqrt{\rho_{b1}{}^3}} = \frac{4\pi}{3} M_3^1 \qquad (4\text{-}9c)$$

$$\frac{c_2}{\sqrt{\rho_{c2}}} + \frac{1-c_2}{\sqrt{\rho_{b2}}} = \frac{4}{2} M_1^2 \qquad (4\text{-}10a)$$

$$\frac{c_2}{\rho_{c2}} + \frac{1-c_2}{\rho_{b2}} = \frac{\pi}{2} M_2^2 \qquad (4\text{-}10b)$$

$$\frac{c_2}{\sqrt{\rho_{c2}{}^3}} + \frac{1-c_2}{\sqrt{\rho_{b2}{}^3}} = \frac{8\pi}{15} M_3^2 \qquad (4\text{-}10c)$$

where, M_1^1, M_2^1 and M_3^1 are the observed first-three moments of the first-nearest-neighbors, whereas M_1^2, M_2^2 and M_3^2 are the observed first-three moments of the second-nearest neighbors. Insofar as a specific point is concerned (feature-centroid), if the distance to its nearest-neighbour point, r_1, is larger than ${r_1}^*$, and the distance to its second nearest-neighbour point, r_2, is greater than ${r_2}^*$, then the point is classified as belonging to background-sets. The procedure is labelled herein, the Schwarz method.

4.2.3 Example with computer generated data sets

As an illustrative example, consider the different arrangements of points as shown in Fig 4.1. The QR method that was introduced in the previous section is applied to the data sets. The following is a MATLAB code of the QR method. Table 4.1 provides the result of the simulation of the data in Fig. 4.1 (a-d).

```
function [r1_bar, E_rho, Q, v_bar, E_v, R] = Distr_Classification(Pcoord,N,A)

 % Pcoord is the x and y coordinates of the points.
 % A is the Area of the region occupied by the points.
 % N is the number of points.
 % rho is the point density of the poisson process.
 % E_rho is the expected mean.
 % E_v is the expected variance.
 % r1_bar is the observed mean.
 % v_bar is the observed variance.

 rho = N/A;
 E_rho = 1/(2*(rho)^0.5);
```

```
 E_v = ((4-pi)/(4*pi))*(1/rho);

 r = zeros(N,1);

 H(:,1) = Pcoord(:,1);
 H(:,2) = Pcoord(:,2);
for i = 1:N
    for j = 1:N
      r(j,1) = ((H(i,1)-H(j,1))^2 + (H(i,2)-H(j,2))^2)^0.5;
    end
              rp = sort(r);
          H(i,3) = rp(2,1);
          H(i,4) = rp(3,1);
end
r1_bar = mean(H(:,3));
 v_bar = var(H(:,4));

Q = r1_bar/E_rho;
R = v_bar/E_v;

End
```

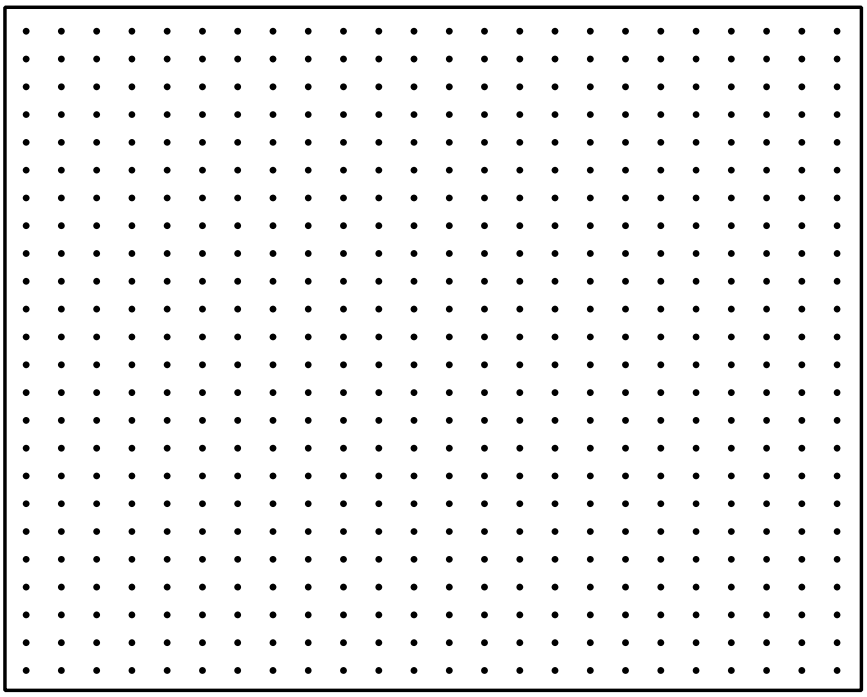

Fig. 4.1(a) Ideal regular distribution of points in a plane.

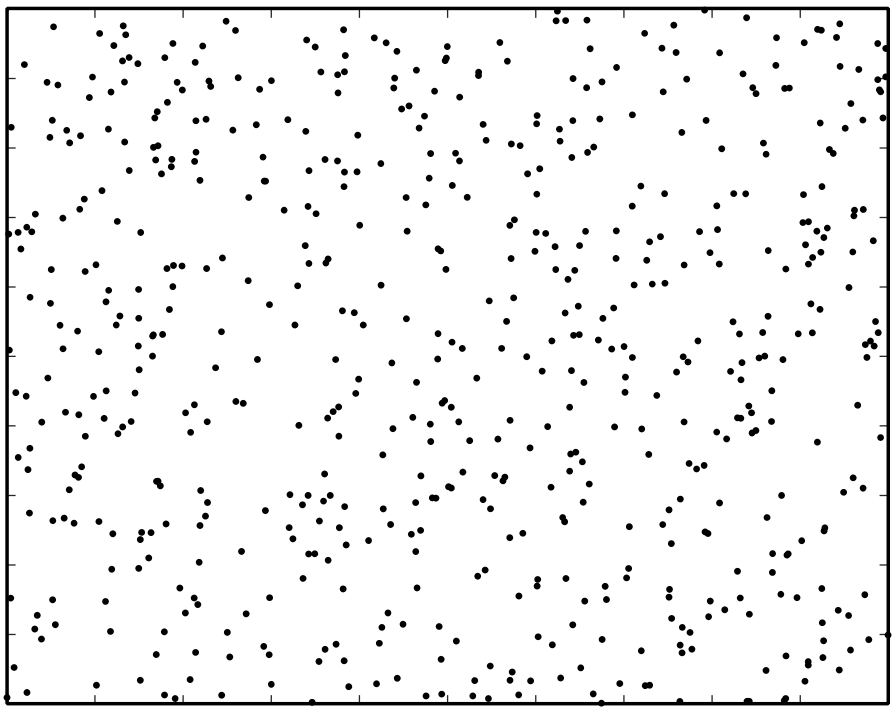

Fig. 4.1(b) Ideal random distribution of points in a plane.

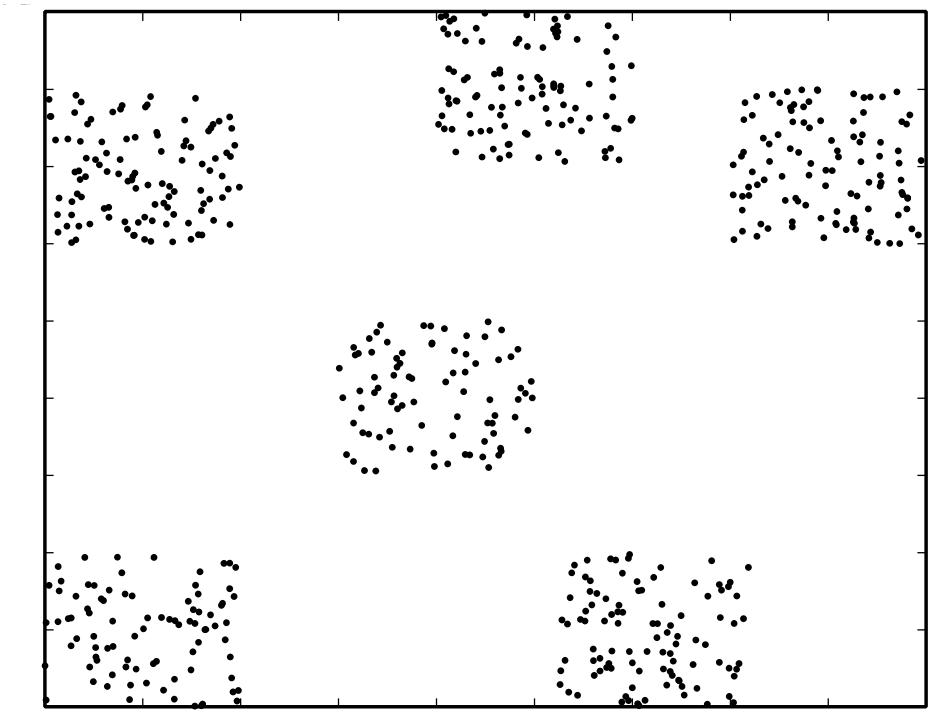

Fig. 4.1(c) Simulated arrangement of points in six isolated clusters.

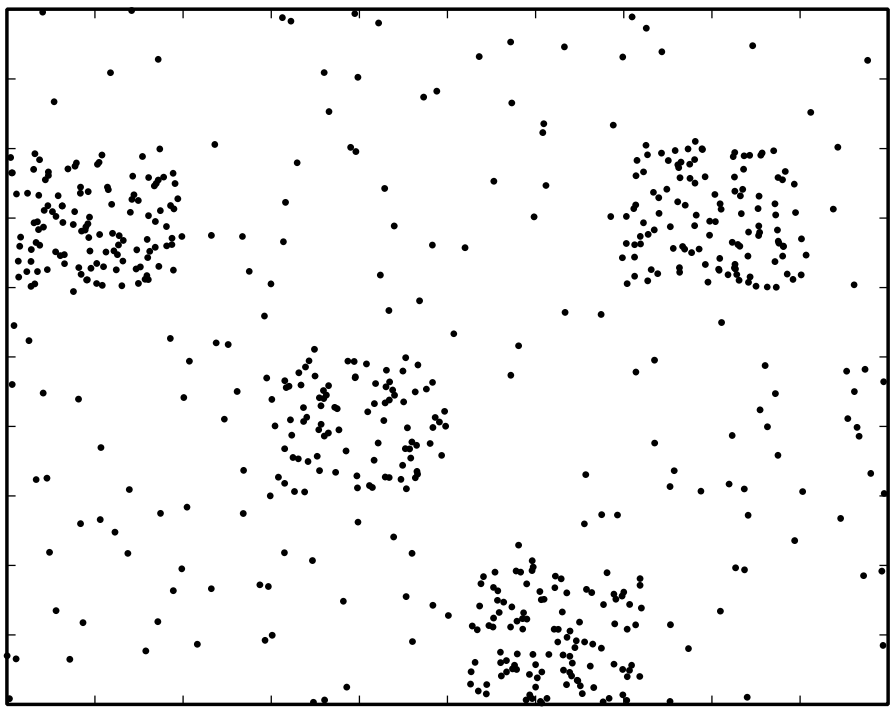

Fig. 4.1(d) Simulated arrangement of points in four isolated clusters in a background of random points.

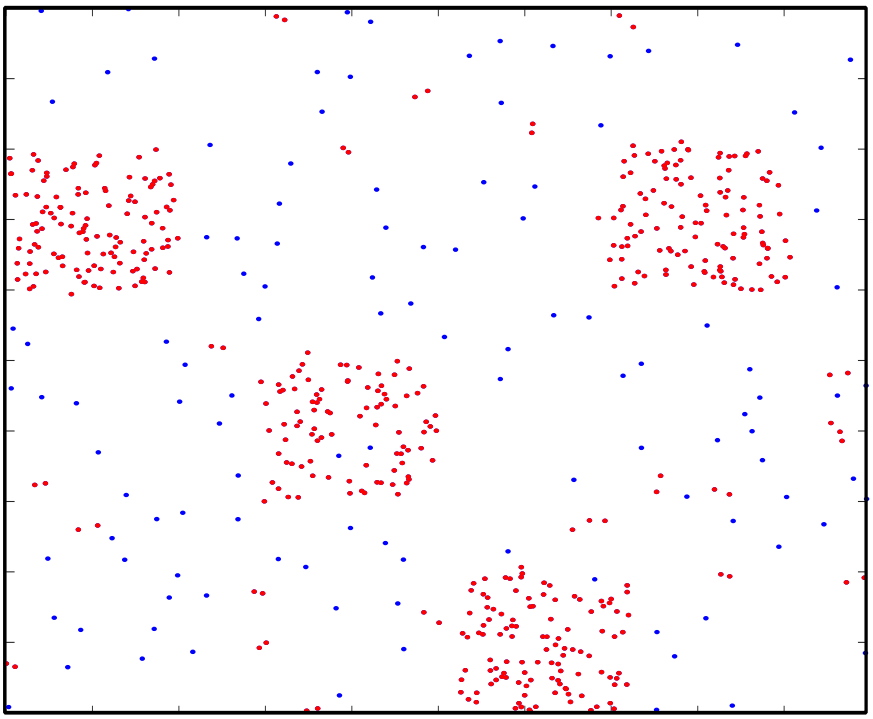

Fig. 4.1(e) Simulated arrangement of points in Fig.4.1(d) separated into cluster set and background random points. red = cluster sets and blue = background random set.

Table 4.1 Main results of the statistical analysis of Fig. 4.1, using the QR method.

Figure No.	Fig. 4.1(a)	Fig. 4.1(b)	Fig. 4.1(c)	Fig. 4.1(d)
Size of area, in unit^2	1	1	1	1
N	576	613	583	599
ρ	576	613	583	599
$\bar{r}_1$	1	0.0203	0.0533	0.0865
$E(\bar{r}_1)$	0.5208	0.0202	0.0932	0.1021
Q	1.92	1.0246	0.5720	0.8472
${s_1}^2$	0	0.00012	0.00099	0.0116
$E({s_1}^2)$	0.0741	0.00011	0.0024	0.0029
R	0	1.09	0.42	4.08

4.3 Application to corrosion pits data of a medium carbon steel

4.3.1 Materials and methods

The material selected for this study was a hot-rolled, medium-carbon, JIS-S45C steel (equivalent to DIN C45 and AISI 1045), very often used in the fabrication of machined engineering parts. Its chemical composition and mechanical properties are outlined in Tables 4.2 and 4.3, respectively. Specimens were 120 mm-long, 24 mm-wide and 1 mm-thick, extracted from the center of a 25-mm-diameter cylindrical bar. The longitudinal direction of the specimens was parallel to the rolling-direction of the base-material. One side of the specimen was mirror-polished, in conformity with the procedure proposed by Samules [77] for the removal of machined layers beneath specimen-surfaces, as part-preparation for the microscopic inspection of inclusions. The polishing process is detailed in Fig 4.2.

Prior to corrosion-testing, the unpolished sides of specimens, as well as all edges, were covered with Teflon tape, to inhibit the corrosion process. The Neutral Salt Spray Test (NSST) was then introduced as a corrosion-testing method, in accordance with JIS Z 2371 (ISO 9227:2017), and a test-solution of 3.5%-NaCl with a 7.0 pH value was selected.

Table 4.2 Chemical composition of the specimens (JIS S45C, medium-carbon steel) in wt.%.

C	Si	Mn	P	S
0.47	0.21	0.82	0.018	0.018

Table 4.3 Mechanical properties of the specimens (JIS S45C, medium-carbon steel)

Elongation, %	Reduction in area, %	0.2% proof-stress, MPa	Tensile-strength, MPa
18.5	53.8	339	620

To ensure that the pH value did not vary, it was measured both before and after testing. The temperature inside the chamber was maintained at 35°C. To investigate the evolution of pit spatial distribution in relation to time, four specimens were exposed to a corrosive environment for 0.5, 2.0, 4.0 or 6.0 hours, as documented in Table 4.4. Hereafter, the uncorroded specimen is identified as S45-0, with the corroded specimens accordingly labelled as S45-0.5, S45-2.0, S45-4.0 and S45-6.0, based on their respective exposure-times.

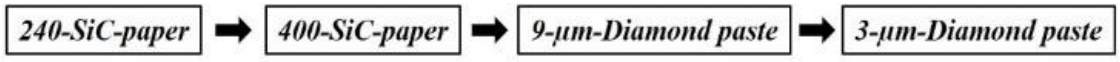

Fig. 4.2 Procedure for mechanical polishing.

Table 4.4 Identification of specimens and their corresponding exposure-times.

Specimen	S45-0	S45-0.5	S45-2.0	S45-4.0	S45-6.0
Exposure-time (hours)	0	0.5	2.0	4.0	6.0

At the outset of the tests, all specimens (except S45-0) were placed in the chamber, with each specimen removed when its individual exposure-time had been attained. Specimen S45-0 was especially reserved for inclusion in the spatial-distribution analysis. After corrosion-testing, specimen surfaces were again mirror-polished, to remove any rust which might have

rendered the microscopic pit-observation rather difficult. During the polishing process, extreme care was taken to ensure that the initiated pits had been buffed adequately.

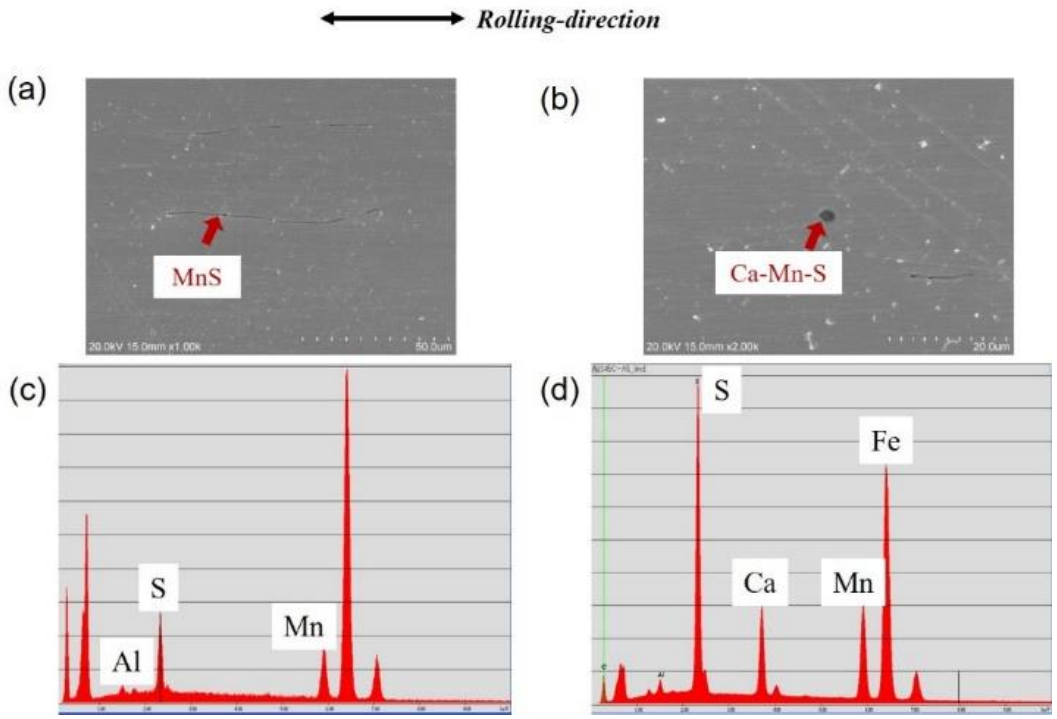

Fig. 4.3 The SEM micrographs of two types of corrosion-free inclusions in a JIS-S45C steel are presented in (a) and (b). EDX spectra of the same are reproduced in (c) and (d). Inclusions shown in (a) and (b) were determined to be MnS and Ca-Mn-S, respectively.

The progress of pit spatial distribution was subsequently observed by means of optical microscopy (OM) and scanning electron microscopy (SEM). The chemical compositions of inclusions in some specimens were identified via energy-dispersive, X-ray spectroscopy (EDX), at an acceleration voltage of 20 kV. Fig. 4.3 showcases the SEM inclusion-images at a higher magnification and at the corresponding EDX spectrum, primarily highlighting two inclusion types, *i.e.*, MnS and Ca-Mn-S. The MnS-size was relatively larger than that of the Ca-Mn-S, with the quantity of MnS superior to that of Ca-Mn-S. Spatial distribution was quantified by OM image-analysis, for which the inspection area was defined as 10×10 mm^2.

The coordinate of each pit-centroid was recorded for all visible pits and reconstructed for the later pit spatial-distribution analysis.

4.3.2 Results and discussion

The corroded specimen-surfaces, after exposure to the corrosive environment, are displayed in Fig. 4.4. Following corrosion-testing, rusted specimen-surfaces were rinsed in de-oxygenated water, later dried using a hot-air jet. Afterwards, mechanical-polishing was employed to remove rust and to prepare specimens for OM-observation. Fig. 4.5 displays examples of the polished S45-0.5 (exposure-time of 0.5 hours) and S45-6.0 (exposure-time of 6.0 hours) specimen-surfaces, after removal of corrosion-rust. While it was noted that corrosion-pits developed in large quantities at 0.5 hours, some individual pits did not really grow as much between 0.5 ~ 6.0 hours. A significant escalation in size occurred predominantly through coalescence with neighboring pits, the evidence of which can be verified via examination of the pit-shape in Fig. 4.5 (b). In fact, the coalescence of pits was already evident from as early as 0.5 hours (*cf.* Fig. 4.5 (a)) and rather obvious from 6.0 hours (*cf.* Fig. 4.5 (b)). Moreover, some coalesced-pits appeared to be elongated, that is, parallel to the rolling-direction of the material.

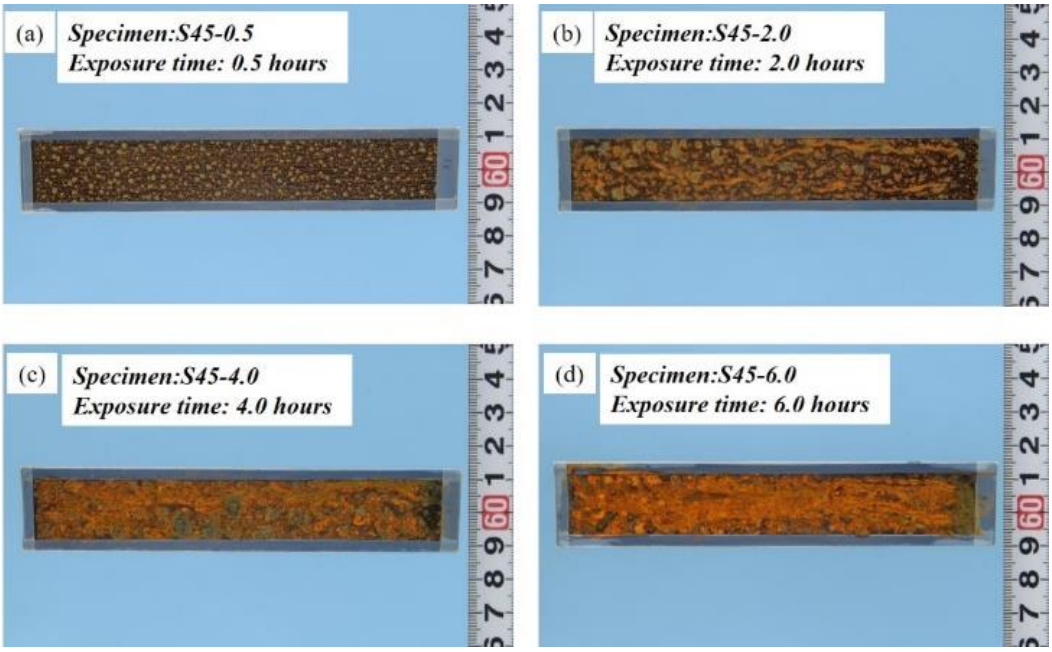

Fig. 4.4 The corroded surfaces of JIS-S45C specimens, after exposure to 3.5%-NaCl for (a) 0.5, (b) 2.0, (c) 4.0 and (d) 6.0 hours at 35°C.

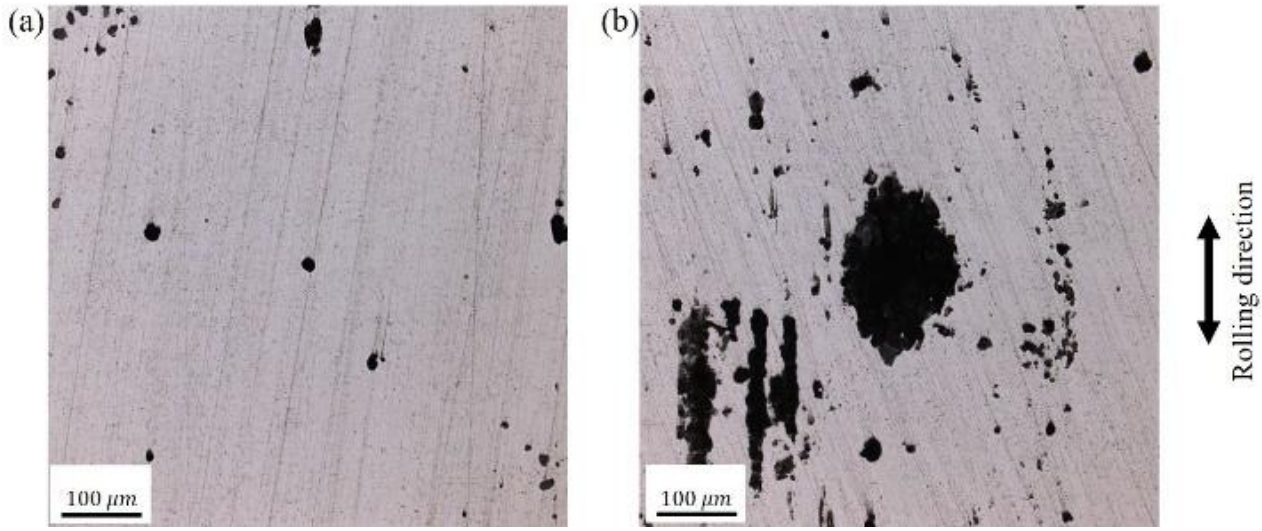

Fig. 4.5 Corrosion pits on the surfaces of JIS-S45C specimens, after exposure to 3.5%-NaCl for (a) 0.5 and (b) 6.0 hours at 35°C. The rolling-direction appeared to play a crucial role in the shaping and formation of coalesced pits.

To observe if there is influence of the underlying material microstructural phases on the observed pits and establish the mode of the corrosion that occurred, specimen S45-0.5 was etched with 3% Nital for 6 seconds to prepare it for microstructural observation. Fig. 4.6 shows

that the underlying material microstructure is combination of ferrite and pearlite phases. Corrosion pits can be found in both phases as well as at their boundaries. This suggest that the observed pits are neither due to a phase type dissolving in another nor due to dissolution at phase boundaries. It remains to show that the inclusions on the specimen surfaces play a key role in the pit initiation process. To demonstrate this, specimen S45-0, which was reserved for inclusion inspection, was exposed to the corrosion chamber for about 5 mins. For this exposure time, there was no need for polishing after the exposure, this is because general corrosion has not occurred. Only localized corrosion at some certain location can be seen. Thus, with this specimen it will be possible to observe the role played by the inclusions in the locations where localized corrosion initiated.

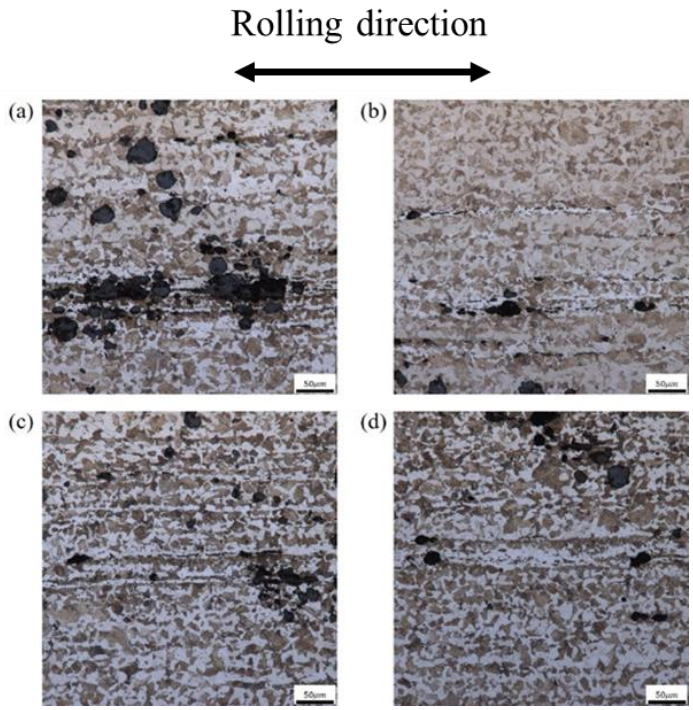

Fig. 4.6 Corrosion pits on the surface of specimen S45-0.5. Pits nucleated at both ferrite and pearlite phases, as well as at their boundaries. (a) – (d) are randomly selected locations on the specimen surface.

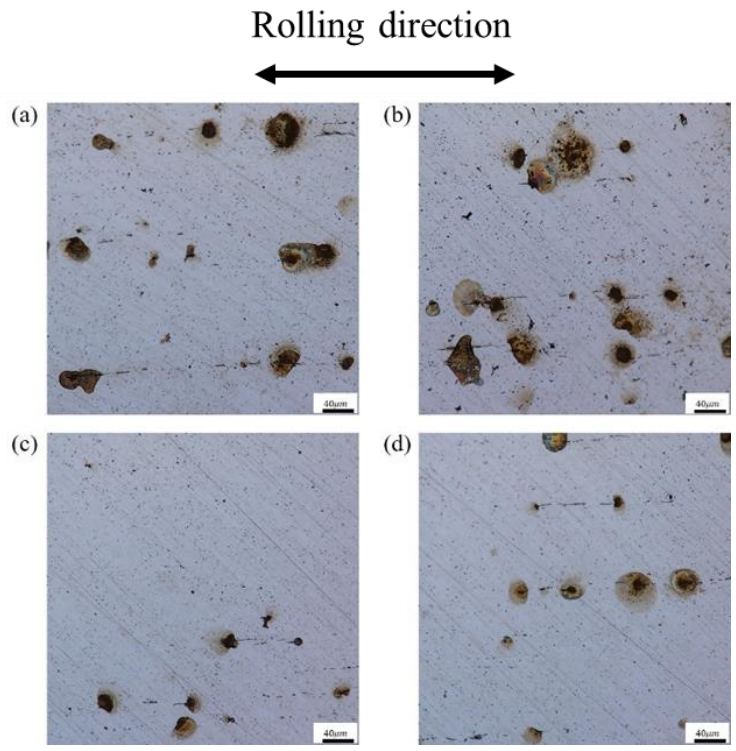

Fig. 4.7 Locations where localized corrosion and pitting occurred on the surface of specimen S45-0.5. An inclusion or cluster of inclusions can be seen at each of the locations where localized corrosion occurred. (a) – (d) are randomly selected locations on the specimen surface.

In Fig. 4.7, it can be observed that each one of the locations where localized corrosion initiated is associated with an inclusion or cluster of inclusions in their vicinity. Wranglen [56] has provided comprehensive theoretical explanation of the mechanism by which localized corrosion initiate and propagate in the vicinity of inclusions, especially sulphides. The work of Ryan et. al [61] is also another excellent work on this topic. Fig. 4.8 displays a reconstructed demonstration of the spatial location of features (inclusions/pits), with each point representing a feature-centroid within the inspection area. Coordinates were normalized according to the length of the review area and based on the data, the distances between all feature-pairs were calculated. Subsequently, according to the arrangement of each feature in ascending order of the appraised gaps, the spaces between the nearest and second-nearest neighbors were recorded.

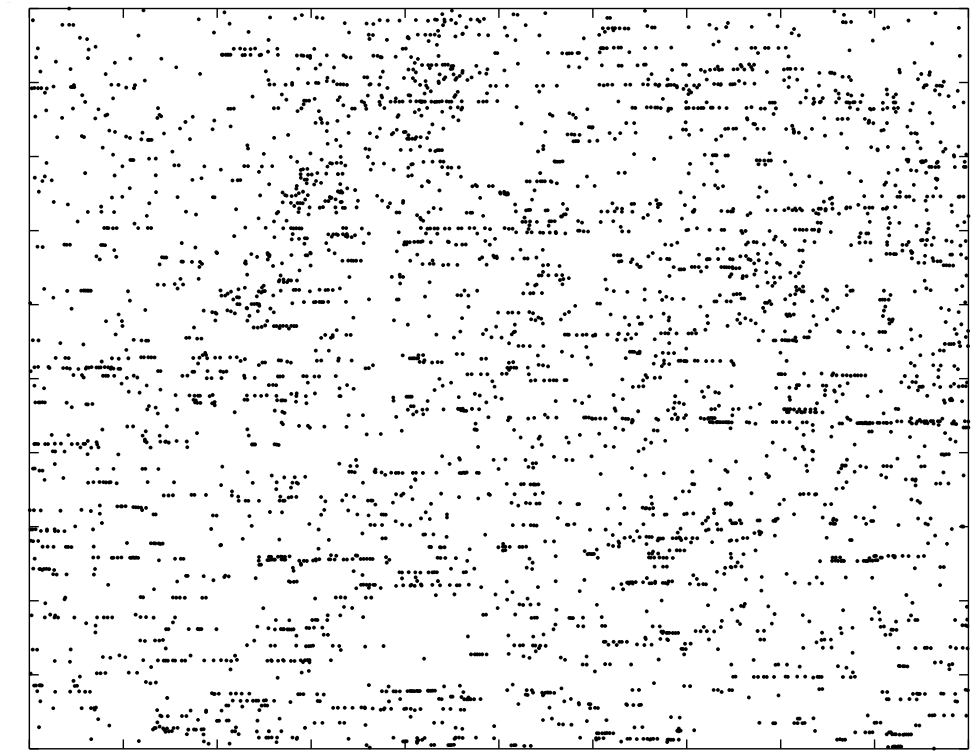

Fig. 4.8(a) Reconstructed, centroid spatial-distribution of inclusions in S45-0.

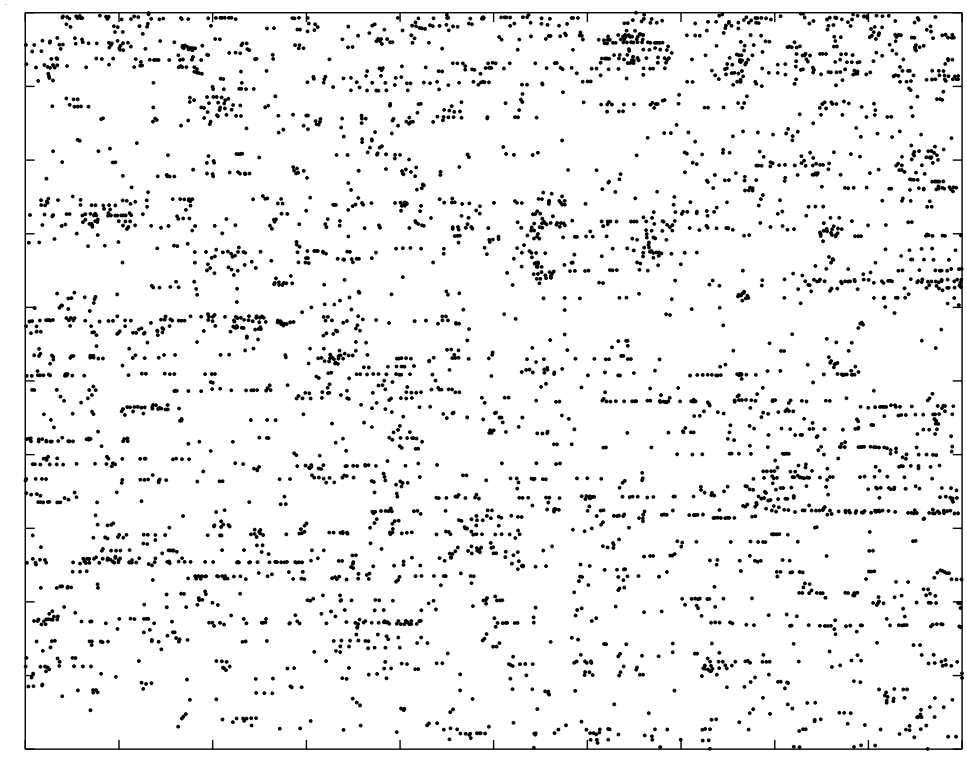

Fig. 4.8(b) Reconstructed, centroid spatial-distribution of pits in S45-0.5.

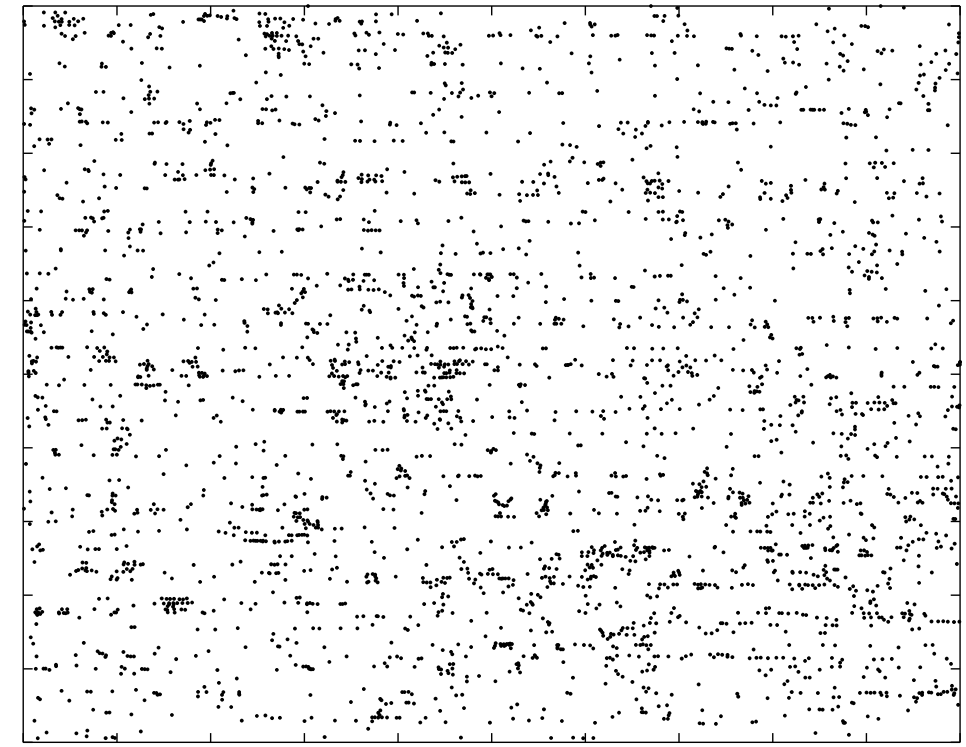

Fig. 4.8(c) Reconstructed, centroid spatial-distribution of pits in S45-2.0.

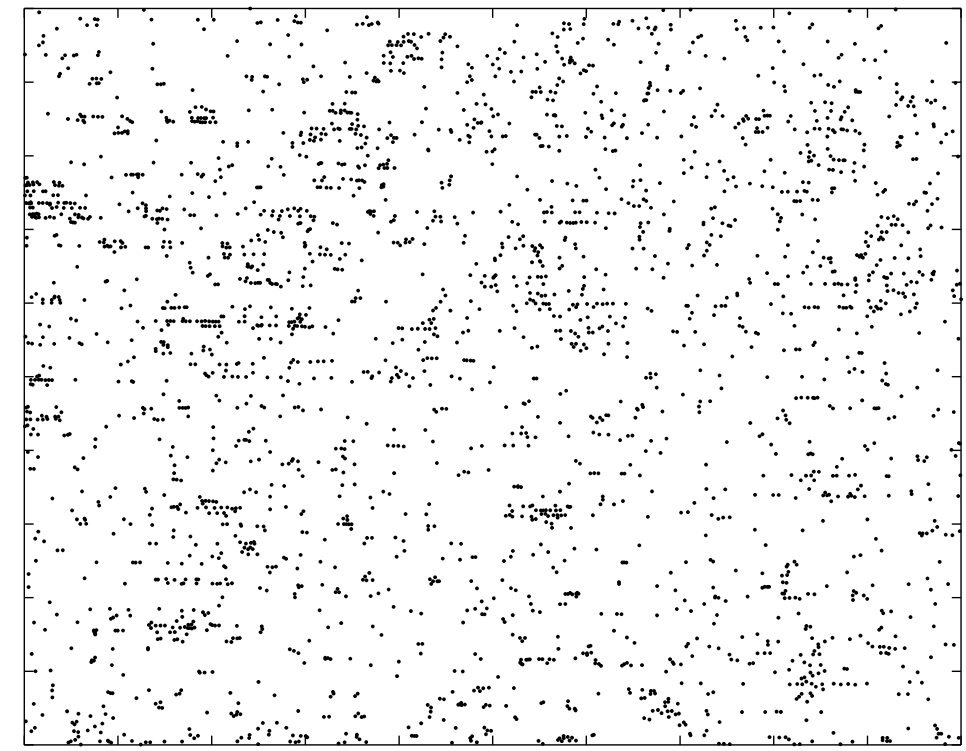

Fig. 4.8(d) Reconstructed, centroid spatial-distribution of pits in S45-4.0.

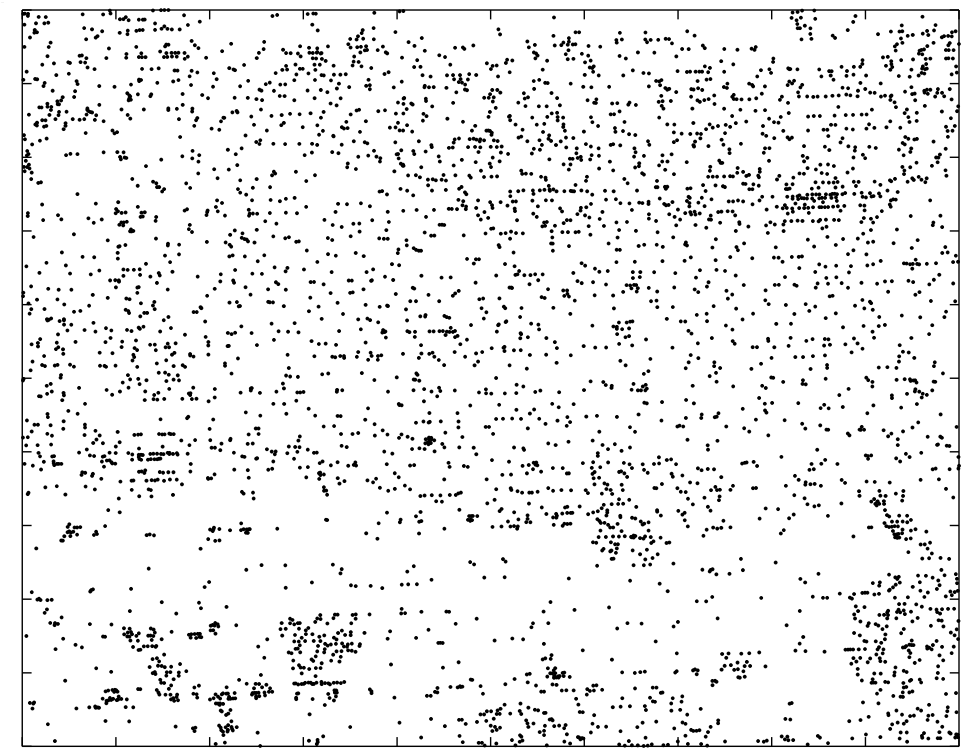

Fig. 4.8(e) Reconstructed, centroid spatial-distribution of pits in S45-6.0.

Table 4.5 Main results of the statistical analysis of pit-data, using the QR method.

Exposure-time, in hours	0	0.5	2.0	4.0	6.0
Size of area, in unit^2	1	1	1	1	1
N	3935	3773	3253	2735	4219
ρ	3935	3773	3253	2735	4219
$\bar{r}_1$	0.0061	0.006	0.0071	0.0078	0.0067
$E(\bar{r}_1)$	0.008	0.0081	0.0088	0.0096	0.0077
Q	0.77	0.74	0.81	0.82	0.87
${s_1}^2$	3.73×10^{-5}	3.81×10^{-5}	4.89×10^{-5}	5.41×10^{-5}	3.12×10^{-5}
$E({s_1}^2)$	1.74×10^{-5}	1.81×10^{-5}	2.09×10^{-5}	2.49×10^{-5}	1.62×10^{-5}
R	2.15	2.10	2.33	2.17	1.92
$\sigma_{E(\bar{r}_1)}$	6.64×10^{-5}	6.93×10^{-5}	0.80×10^{-5}	9.56×10^{-5}	6.19×10^{-5}
c	28.6	30.3	21.6	18.84	16.14
Probability of a greater difference between $\bar{r}_1$ and $E(\bar{r}_1)$	$< 1.0 \times 10^{-7}$	$< 1.0 \times 10^{-7}$	$< 1.0 \times 10^{-7}$	$< 1.0 \times 10^{-7}$	$< 1.0 \times 10^{-7}$

In terms of the quantitative characterisation of the spatial distribution of features, both the equations and the QR method were programmed into a MATLAB code and applied to the test data. The major parameter outputs are listed in Table 4.5. Similarly, the Schwarz method was

incorporated into a MATLAB code, to identify features belonging to cluster-sets. Consequently, regarding specimen S45-0, $\underline{Q}$ = 0.77 and R = 2.15, this demonstrates that the inclusion-population is clustered with a superimposed background-set. According to the Q value of 0.77, the nearest neighbors are, on average, 0.77 times further apart than would have been expected if inclusions had been distributed arbitrarily.

The (Q, R) values were $(0.74, 2.10)$, $(0.81, 2.33)$, $(0.82, 2.17)$, and $(0.87, 1.92)$, for the specimens S45-0.5, S45-2.0, S45-4.0 and S45-6.0 respectively. This data implies that their arrangement was in cluster-sets against an overlapping background. The pit-centroids belonging to the cluster-set identified by red dots, with the background set identified in blue, are both illustrated in Figs. 4.8 (b-e). The Q value for the pit-population, as seen on S45-0.5 ($Q = 0.74$), very closely approximates that of the inclusion-distribution of S45-0 ($Q = 0.77$).

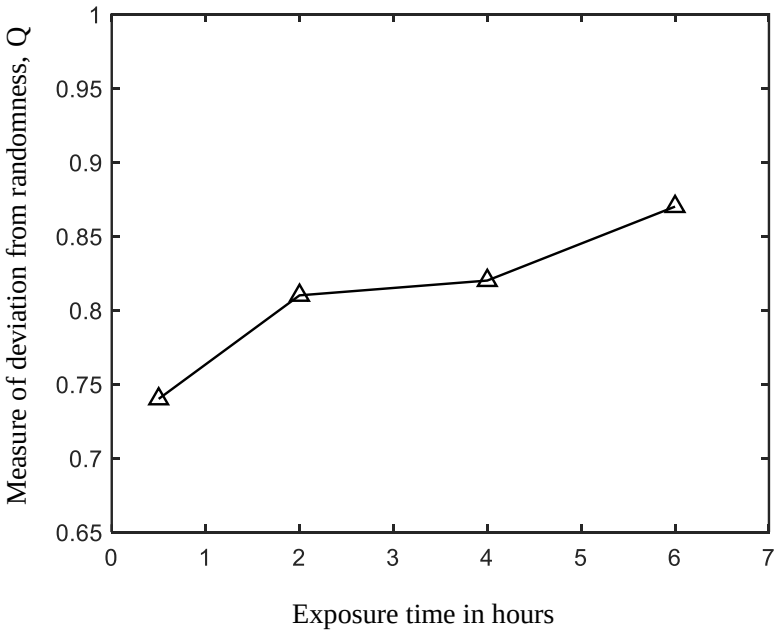

Fig. 4.9 The Q value for pit-distribution in JIS-S45C, as a function of exposure-time.

Despite the two datasets being obtained from different specimens, the divergence remains less than 4%. Such a result confirms the possibility of predicting the spatial distribution of pits

from the outset of corrosion, based on the inclusion-data registered from specimen-surfaces prior to the onset of corrosion. The reason for the compelling correlation between inclusion-population arrangement and corrosion-pits is that most corrosion-pits launch at/near inclusion-sites. This occurrence has already been acknowledged by materials science researchers [56, 59-61], whilst never having yet been used to foretell the pit-population arrangement at the outset of the corrosion process. Furthermore, within the context of exposure-time to a corrosive environment, Fig. 4.9 details the evolution of the Q value, surging from 0.74 to 0.87 within a timeframe of 0.5 ~ 6 hours. Such an event indicates that the increase in exposure-time results in changes to the spatial distribution of corrosion-pits, ranging from randomly distributed clusters with superimposed background-sets to non-homogeneous random distribution. This change is primarily due to the coalescence of corrosion-pits, in close-enough proximity to form larger pits.

Cawley and Harlow [78] attempted to characterise the spatial distribution of inclusions on the surface of a 2024-T3 aluminum alloy and its corrosion-pits, after exposure to a 0.5M-(3.5%)-NaCl environment for 10 ~ 72 hours. Qualitative characterisation was accomplished by comparison of the second, reduced-moment function of inclusion/corrosion-pit centroids, $K(t)$, within the anticipated secondary, reduced-moment function of the complete spatial-randomness (CSR) model. Fig 10 presents $K(t)$, along with experimental data for inclusions and corrosion as functions of *t*, where *t* is the distance between the centroids of inclusion-/corrosion-pits [69]. Since the estimated, corrosion-pit data curves all fell below the diagonal line of the CSR model, it was presumed that the pit-centroids had been distributed regularly. Furthermore, since most portions of the estimated inclusion-data curve fell above the diagonal line of the CSR model, it was inferred that the inclusion-centroids displayed a cluster-type distribution. The approach by Cawley *et al.* is similar in principle to the QR method. The diagonal line of the CSR model is equivalent to $Q = 1$, whereby the curve that shifts above and

below the diagonal line corresponds to $Q < 1$ and $Q > 1$, respectively. From such a viewpoint, it appears that Cawley *et al.* accurately classified the spatial corrosion-pit distribution as an evolution into something perfectly regular that corresponds with time.

In Fig. 4.10, the estimated pit-curves shift further away from the diagonal straight-line, with an increase in corrosion-time corresponding to a heightened value of Q. However, the inclusions data was merely classified as clustered sets, which might not necessarily be correct. More correct classification for the inclusions can be cluster sets with superimposed background set. Namely, if all the portion of the estimated curve for the inclusions lies above the diagonal line, then the data can be classified as cluster sets, but if some part of the curve lies above the diagonal line and the other part below it (see the data for "as polished: 216 particles" in Fig. 4.10), it is more appropriate to classify them as cluster sets with superimposed background set. However, Cawley and Harlow attributed the section of the estimated inclusion-data curve situated below the diagonal line of the CSR model to measurement limitations of the microscope used. By employing a quantitative approach (*e.g.*, the QR method), such a classification error could be avoided - a definite advantage of the proposed technique.

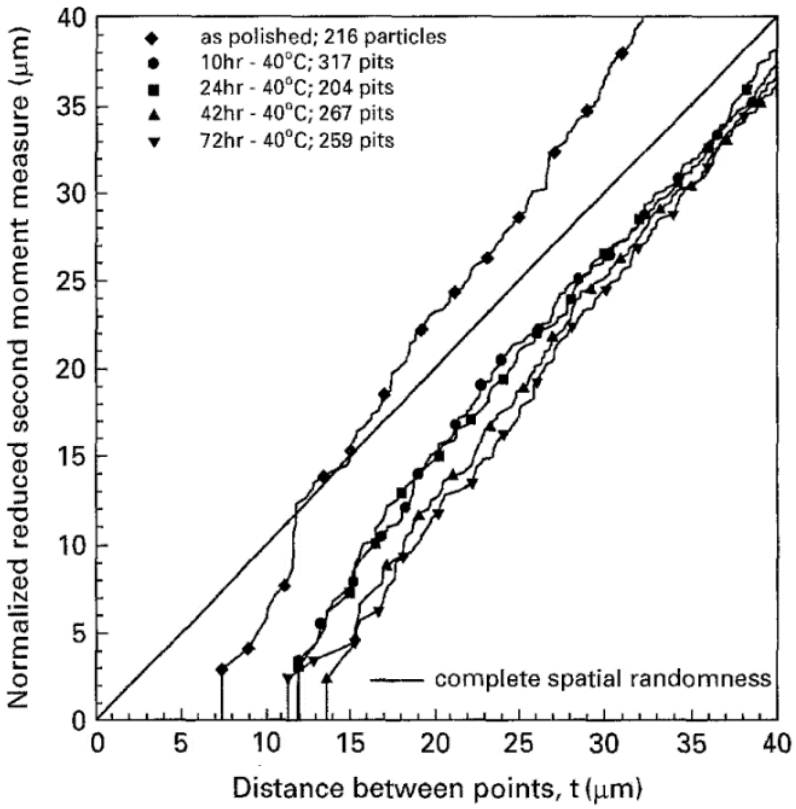

Fig. 4.10 Estimation of *K* for 2024-T3 aluminum alloy-specimens, before and after exposure to a 0.5M-NaCl solution for 10, 24, 42 and 72 hours at 40°C [69].

4.4 A new cleanliness rating method suitable for materials operating in a corrosive environment

Used for the quality-control of materials, the conventional standards for inclusion-rating (i.e., ISO 4967, JIS-G-0555, ASTM E45 and DIN 50602) focus primarily on the shape, density, and size of inclusions, to determine the cleanliness index of metal samples. Although those guidelines may be appropriate for materials to be used in air, they are not suitable for those destined for use in corrosive environments, where pitting is the driving force behind most failure mechanisms. This is because the spatial distribution of inclusions plays a more crucial role in corrosion pit-arrangement/-growth [62-73], as opposed to size. Once pits initiate at/near inclusion-sites, their growth is driven mainly by coalescence with neighboring pits. This

phenomenon should be considered for inclusion-rating, especially when the materials are destined for corrosive environments. Therefore, a combination of the QR and Schwarz methods is proposed as a novel, inclusion-rating system.

Assuming two set of samples of similar material from different batches (Batch A and Batch B) are to be subjected to quality control analysis. According to the Q*R* method, if samples from Batch A and B has a *Q* value of 0.93 and 0.65 respectively. Then, Batch B would consequently be expected to be more clustered than Batch A. If samples from both Batches A and B were to be placed in identical corrosive environments for an equivalent period of exposure, the Batch B sample would be expected to generate larger corrosion-pits. Therefore, Batch A could be judged to be cleaner than Batch B.

Additionally, in cases where *Q* and *R* values are close for both Batches, the Schwarz method can additionally be used to identify inclusions belonging to the cluster sets for further analysis. Moreover, by analyzing the shape of the cluster sets, very important deduction can be made. For example, let us presume that Batch A contains cluster sets that are mostly circular in shape while Batch B contains cluster sets that are mostly arranged in a line perpendicular to loading direction. The former can be judged as superior in view of corrosion fatigue strength. This is because if we regard their resulting coalesced pits as mechanically-equivalent to small cracks, as proposed by Murakami [22], the projected area of coalesced pit from Batch B will be larger than Batch A, as a result, the stress intensity of coalesced pits from Batch B will be larger than Batch A.

CHAPTER 5. Applications to some practical problems

5.1 Quality control of materials with defects

It is an established fact that material cleanliness plays a crucial role in the structural strength of components. This is because material defects such as non-metallic inclusions, voids, cavities, and corrosion pits often act as the primary roots of fracture. Conventional standards for the ranking of materials for quality control (e.g., ISO 4967 [53], JIS G-0555 [54] and ASTM E45 [55]) typically fall into two categories. One is the qualitative approach which promotes the visual comparison of the sizes of defects found on a sample surface, while the other is rather quantitative, involving the measurement of the size and number of defects in an inspection area. However, the application limitations of these procedures have been pointed out by Murakami [2]. The primary problem is that these methods for evaluating material cleanliness do not take the fracture processes into account. Hence, the results obtained via the existing techniques cannot always be useful for ranking materials against the real fracture phenomena. Murakami [2] proposed to apply the statistics of extremes to the prediction of the maximum defect size (e.g., non-metallic inclusion) contained in a given control volume in materials.

The noteworthy merit of statistics of extremes is that it can allow for the effect of control volume, i.e., the maximum defects included in a manufactured components naturally increase with a rise in sample population. This fact is completely ignored in the aforementioned conventional standards. However, the Murakami's method does not consider the spatial distribution of defects and therefore cannot evaluate the possible interaction effects of cracks that might initiate from the defects, this makes it invalid for engineering fracture processes where interacting multiple cracks plays a predominant role. This type of scenario has been

reported in corrosion fatigue problems where fatigue cracks initiate from distributed corrosion pits formed by chemical reactions between inclusions and a corrosive environment [10, 56, 57]. It was also reported that, in additively-manufactured and cast components, crack interactions cannot be ignored for the colony of surface cracks initiated from defects [2, 5]. In such cases, the quality control of materials should bear in mind the spatial distribution of defects and cracks. As a solution, the numerical analysis developed in the present study can be a novel ranking methodology, used in conjunction with the Monte Carlo simulation technique. The following case study will provide context for demonstrating the procedure.

On a monthly basis, a particular company received thousands of batches of certain load-carrying cast components from Supplier A. However, due to changes in the company's policy, the management decided to switch from Supplier A to Supplier B. Inclusion analysis for batches from the respective suppliers showed that inclusions over an inspected area in Batch A were larger in size than those in Batch B, although they were less dense in A than in B. The aim of this study was to determine which batch was cleaner from the viewpoint of the fracture process, when a component was primarily subjected to tensile loading, as shown in Fig. 5.1. Such a judgement should include the statistical nature of both the sizes and locations of the defects in the materials. The results from quantitative inclusion measurements using polished samples from Batches A and B are recorded in Table 5.1.

Table 5.1 Quantitative inclusion measurements of samples from Batches A and B.

	Density of inclusions	Mean of lengths of inclusions, μm	Standard deviation of lengths of inclusions
Batch A (Supplier A)	69.5	9.19	1.61
Batch B (Supplier B)	89.0	6.78	1.47

Assuming that the non-metallic inclusions were randomly distributed in both batches, any cracks initiating from those inclusions would be expected to follow a similar spatial distribution, i.e., the spatial distribution of inclusions can serve as a blueprint for that of

initiated cracks. In this analysis, semi-elliptical surface cracks with aspect ratios of 0.5 were presumed for both batches. The Monte-Carlo simulation procedure was then incorporated. For each batch, 100 "virtual" specimens were generated by the Monte-Carlo engine for two containers, namely Containers A and B, fabricated from Batches A and B, respectively. In other words, 200 "virtual" specimens were generated in total. Next, 25 cracks were distributed on the surfaces of each specimen, with the statistical distribution of the crack sizes and locations reflecting the statistical data reported in Table 5.1.

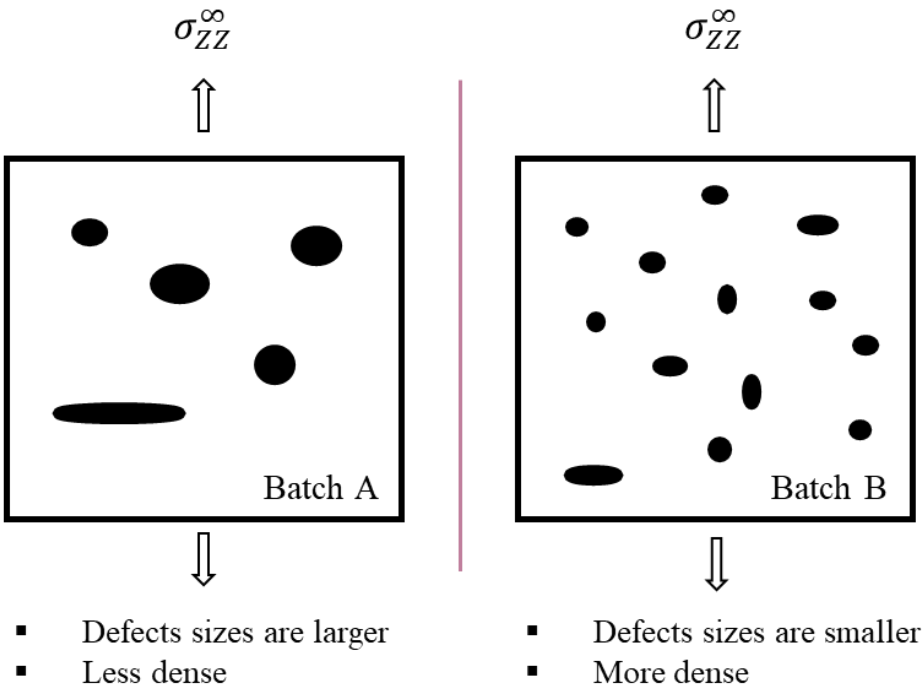

Fig. 5.1 Inclusions from two different batches.

The simulation included 100 iterations, with each iteration using a pair of "virtual" specimens, one extracted from container A and the other from container B. Under tension, the maximum SIFs in the specimens from containers A and B, $K_{\mathrm{I,A}}^{\max}$ and $K_{\mathrm{I,B}}^{\max}$, were reported for each run. After n iterations, n_A is the number of times for $K_{\mathrm{I,A}}^{\max} < K_{\mathrm{I,B}}^{\max}$ similarly n_{B} is that for $K_{\mathrm{I,B}}^{\max} < K_{\mathrm{I,A}}^{\max}$ The output results after each iteration were:

$Prob_{\mathrm{B}} = \frac{n_{\mathrm{B}}}{N}$, Probability that Batch B was cleaner than Batch A.

$Prob_{\mathrm{A}} = \frac{n_{\mathrm{A}}}{N}$, Probability that Batch A was cleaner than Batch B

The result from the 100 iterations is reported in Fig. 5.2. The entire simulation took about 13 hours to complete when perform on a typical desktop computer with prevalent CPU (e.g., Intel(R) Core (TM) i3-8100 CPU 3.60 GHz). It was intriguing to follow how the probabilities evolved with the number of iterations. During the first 10 iterations, the contest was nearly a draw, but a difference began to emerge after about 20 iterations and stabilized after about 40. Statistically, the conclusion to be drawn from the simulation is that there was a 0.77 probability that a random sample from Batch B was cleaner than one from Batch A; hence, Batch B was judged to be "cleaner" under the present circumstances.

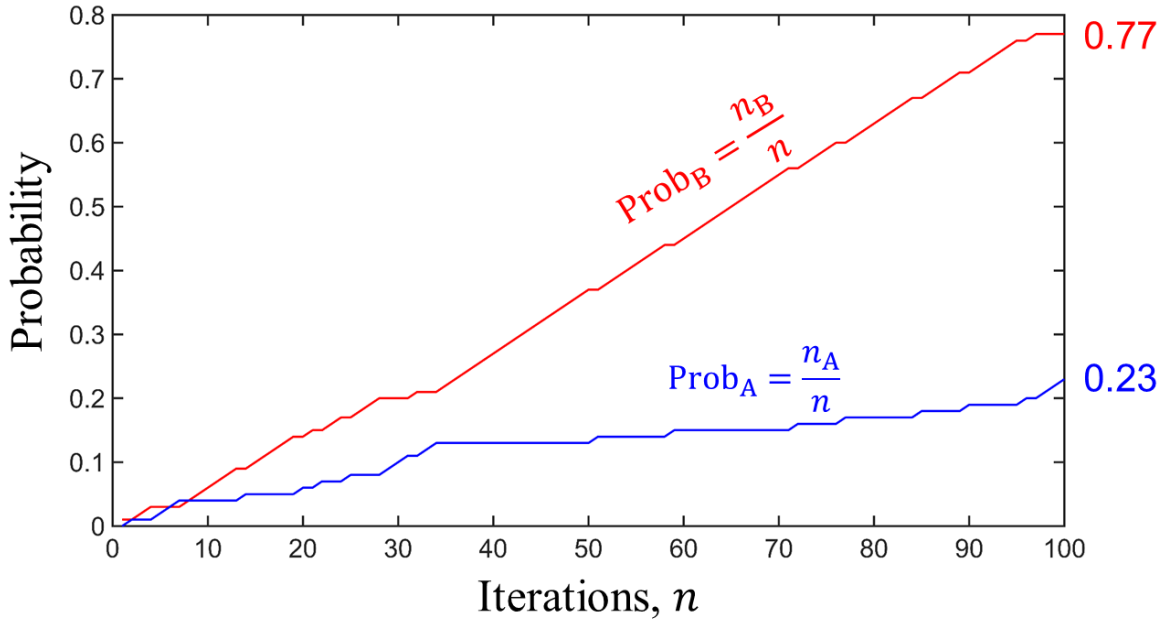

Fig. 5.2 Monte-Carlo simulation of virtual samples from Batches A and B

The result predicted that if 100 real tensile tests were to be performed using pairs of specimens from the two batches, the breaking load for Batch B would exceed that of Batch A

in 77 cases. It is also noted that another advantage of the method proposed here is that it can consider the effect of the actual loading type in the determination of a cleanliness ranking. Indeed, it would be interesting if a similar simulation were to be conducted for shear loading and multiaxial loading. Such a study could lead to remarkable findings about the effects of loading types on material quality assessment.

5.2 Corrosion-fatigue prediction model

Larrosa et al. [58] comprehensively reviewed several models for the prediction of corrosion fatigue-strength in machines and structures subjected to cyclic-loading in corrosive environments, the main limitations of which were already explored in the introductory section of this study i.e., they are of the SDM type. Although essentially quite thorough, a major theory proposed by Kitagawa et al. [10] was nevertheless overlooked in the Larrosa investigation. In fact, the Kitagawa approach to the problem of corrosion fatigue-strength seems to be the most appropriate, based on the actual mechanism of corrosion-fatigue failure. The Kitagawa model (KM) involves the statistical simulation of numerous distributed cracks, while also accounting for the interaction effect of their Stress Intensity Factors (SIFs), the simulation variables being the sizes and spatial locations of cracks. However, from a practical standpoint, there are four key limitations to the KM: (i) the spatial-distribution parameters of corrosion fatigue-cracks must be identified prior to simulation; (ii) the size-distribution criteria of corrosion-fatigue cracks need to be understood before replication; (iii) the crack-propagation stage is not included; (iv) during the SIF computation of cracks, the interaction factors of two-dimensional cracks in an infinite plate are to be used, as opposed to those of multiple, three-dimensional surface cracks. These limitations must first be addressed to ensure that the KM is useful to engineers during the design stage of components to be used in corrosive environments, most

of the necessary input data (e.g., size, and spatial distribution of corrosion-pits) not being available at the outset.

To experimentally validate KM, Kitagawa et al. [10] performed corrosion-fatigue tests on a high-strength steel plate with a tensile strength of σ_{UTS} = 530 MPa. The stress ratio and test frequency were 0.04 and 10 Hz, respectively. The corrosive environment was distilled water, with a pH value ranging from 5.6 ~ 6.0, run at a flowrate of 0.25 cm^3/s . Initially proposed by Masuko et al. [79], the Homogeneity function method was applied by Kitagawa et al. to determine the spatial distribution of cracks for statistical simulation. Based on the Masuko concept, the degree of departure of a population's spatial distribution from an ideal homogeneous arrangement, *D*, can be determined by subtracting the *H* value of a uniformly-random distribution, H_random, from that of the population, H_population. The formulae for the calculation of *H* can be found in [10], [79]. In principle, the *D* value in the Homogeneity function method is similar to the *Q* value in the QR method: D = 0 corresponds to *Q* = 1, both indicating that the population is an ideal uniformly random distribution. Likewise, $D > 0$ is equivalent to $Q > 1$, both implying a deviation from ideal randomness towards regularity. However, a difference emerges in the case where $D < 0$ (i.e., $Q < 1$). According to the Homogeneity function method, a negative *D* value implies a deviation from ideal randomness towards clustering. Nevertheless, the Homogeneity function method cannot differentiate between regular cluster sets and those with a superimposed background distribution, since both scenarios register $D < 0$. On the other hand, using the *R* value via the *QR* approach, one can separate between the two.

A test result from the Kitagawa study [10] is presented in Fig. 5.3. It displays the spatial distribution of corrosion-pits and cracks on a specimen surface, at a stress range of 235 MPa after 1×10^6 cycles. H_population and H_random for Fig. 5.3 were respectively reported to be 8.4039 and 8.5608, corresponding to the *D* value of −0.0569. However, cracks were still

classified according to uniform-random distribution. Since the inherent difference between them was small, Kitagawa et al. argued that both *H* values could be considered equal (*D* = 0). However, this premise may not be acceptable, since even a *D* value of −0.008 is enough to classify a distribution as “clustered”, according to the Homogeneity function method [79].

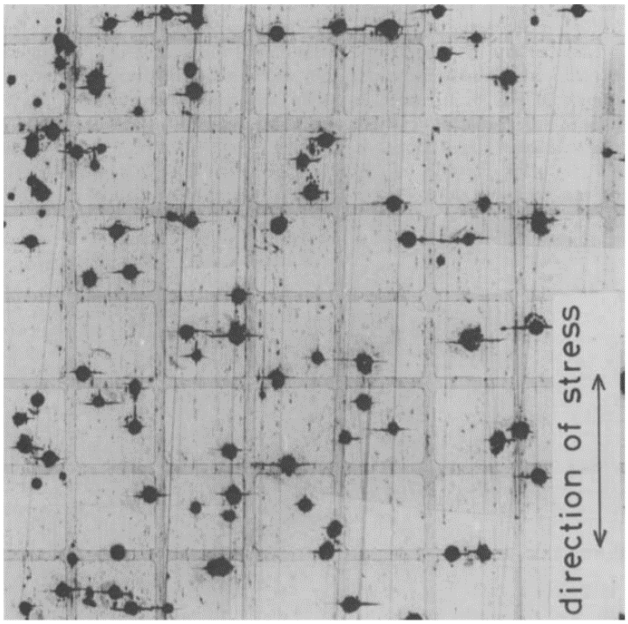

Fig. 5.3 Multiple corrosion-fatigue cracks on the surface of a high-strength-steel plate, after exposure to a corrosive environment at a stress-range of 235 MPa after one million cycles. All the cracks initiated from corrosion-pits [10].

In most practical cases, since the distribution of inclusions and corrosion-pits often stem from the superposition of clusters and incidental background-sets, the QR method is deemed to be the most appropriate. Furthermore, based on the observations recorded in this study, it is proposed that in the KM-context, the spatial distribution of inclusions be substituted for that of corrosion fatigue-cracks, thereby providing a solution to the first, afore-mentioned limitation. Information about the spatial distribution of inclusions in materials can be obtained by following the experimental procedures outlined in this study. Further investigations into the

other three identified drawbacks are of critical import if a model for the prediction of corrosion fatigue-strength is to be developed based on the fracture-process and will feature in our future research.

5.3 Crack size dominance or crack interaction dominance fracture process

IDM are more challenging to implement than SDM because the former requires the estimation of interaction factors among multiple distributed cracks. In Chapter 2, it was shown that estimation of the interaction effects of multiple distributed cracks is a challenging and computationally expensive task. Due to its simplicity and ease of implementation, SDM is usually preferred by researchers and engineers, this is also for cases where IDM is clearly more appropriate. The reasoning behind this approach is the assumption that maximum Mode I SIF should occur at the largest crack, hence the presence of the other cracks can be ignored. The validity of this assumption has not been previously checked.

Numerical results from Chapter 3 shows that exclusion of interaction factor can result to significant error in the estimation of the maximum K_{I} of the largest crack, if such interaction effect is indeed present. The aim of this section is to address the following research questions.

- Is the assumption that $K_{\mathrm{I,max}}$ should occur at the crack with the largest size always valid ?
- What is the influence of crack density on $K_{\mathrm{I,max}}$ on the crack interaction?
- What is the estimation error when interaction effect is ignored in calculation of $K_{\mathrm{I,max}}$?

The virtual specimens are semi-infinite body consisting of randomly distributed semi-elliptical surface cracks having aspect ratio, $\frac{b}{a}$ of 1. The spatial arrangement of the surface

cracks is assumed to be random distribution. The spatial distribution density ρ, number of crack per unit area, varies ranges from 5 to 100. For each specimen, the cracks are of similar size except one, whose size is multiple times of the others. The size ratio of the largest crack to the other cracks is phi, φ. Tensile stress is applied at infinity as shown in Fig. 5.4.

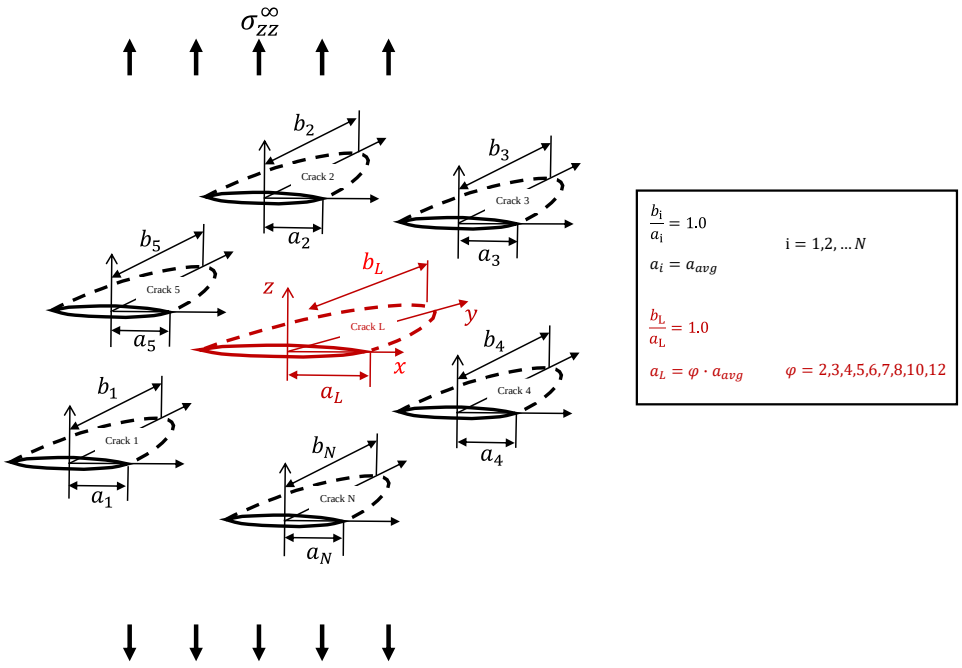

Fig. 5.4 Distributed surface cracks in a semi-infinite body under tensile stress.

In total, 731 virtual specimens are involved in the experiments. These specimens are divided into 6 groups depending on their spatial density, ρ. Within each of the group, the specimens are further grouped based on the value of their size ratio, φ as shown in Fig. 5.5(a-f). It should be noted that each of the 731 specimens possesses own unique spatial arrangements of the cracks. These arrangements are generated within MATLAB with a random point generator. Similarly, the location of the largest crack is randomly selected for each specimens. By so doing, the aim is to include in this study how defects are naturally distributed on material surfaces in this study.

(a) Density, ρ = 5. Number of arrangements = 180, 20 arrangements for each of the 9 size ratios, φ

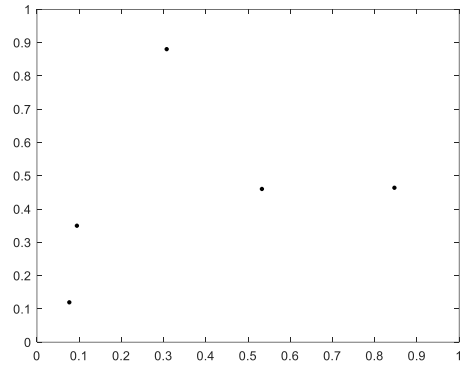

(b) Density, ρ = 10. Number of arrangements = 180, 20 arrangements for each of the 9 size ratios, φ

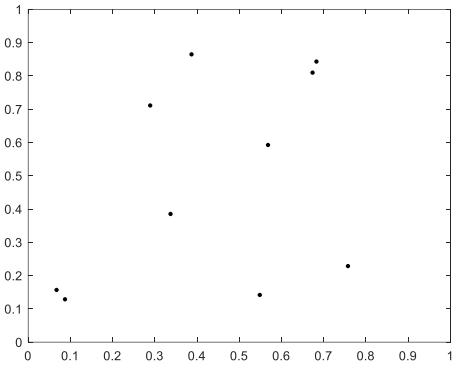

(c) Density, ρ = 15. Number of arrangements = 180, 20 arrangements for each of the 9 size ratios, φ

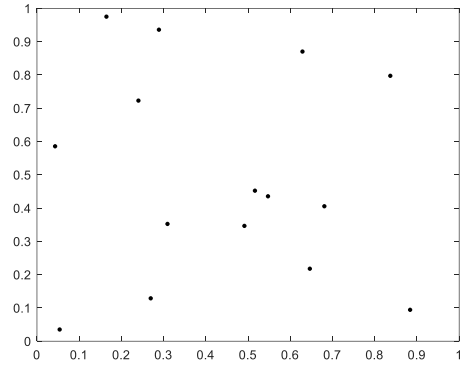

(d) Density, ρ = 20. Number of arrangements = 180, 20 arrangements for each of the 9 size ratios, φ

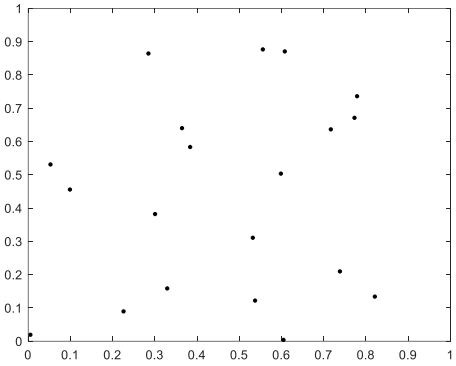

(e) Density, ρ = 50. Number of arrangements = 9., 0ne arrangement for each of the 9 size ratios, φ

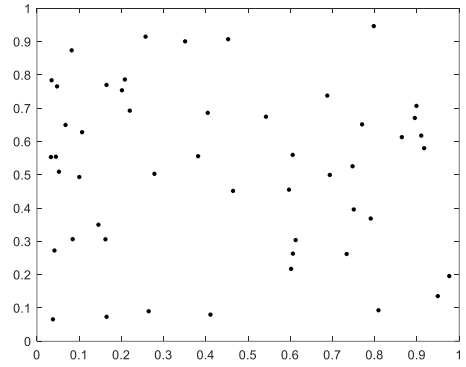

(f) Density, ρ = 100. Number of arrangements = 2, one arrangement for size ratio, $\varphi = 4$ and $\varphi = 7$

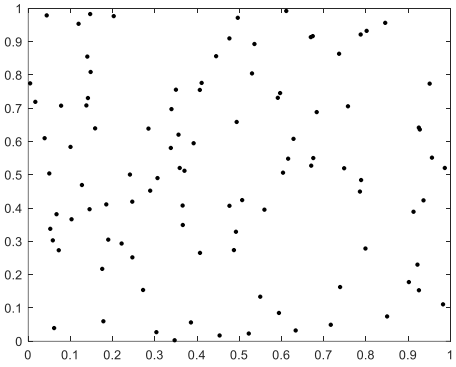

Fig. 5.5 Different possible arrangements of cracks in the 731 virtual specimens.

For each of the 731 specimens, the maximum Mode I SIF, $K_{\mathrm{I,max}}^{\text{all cracks}}$ when tensile stress is applied is recorded, the result is divided by the maximum Mode I SIF, $K_{\mathrm{I,max}}^{\text{largest crack only}}$ if only the largest crack was present on the specimen surface. The outcome, interaction factor γ, represent the interaction effect of the surrounding cracks on the largest crack in the specimens. When the interaction factor is less than 1, it represents a decrease in the maximum Mode I SIF of the largest crack i.e., positive interaction effect. When the interaction factor is greater than 1, it represents an increase in the maximum Mode I SIF of the largest crack i.e., negative interaction effect.

The results for all the different size ratios and crack densities are shown in Fig 5.6 .Some of the key findings are highlighted below.

- For a fixed Size ratio, φ there is no correlation between interaction factor, γ and crack density, ρ.
- When $\varphi < 4$, there exist arrangements where $K_{\mathrm{I,max}}$ did not occur at the largest crack, rather at one of the smaller sized crack.
- When $\varphi \geq 4$, the maximum Mode I SIF, $K_{\mathrm{I,max}}$ always occur at the crack with the largest crack.

As the Size ratio increases, the limits (upper and lower) of the interaction factor, approaches a value of 1, i.e., the interaction effect diminishes as Size ratio increases. The regions in Fig. 5.6 can be divided into two zones depending on where $K_{\mathrm{I,max}}$ is expected to be located. Since it is not possible to predict beforehand where $K_{\mathrm{I,max}}$ will be located when $\varphi < 4$, this zone can be referred to as Interaction Dominant Zone, IDZ. In this zone, SDM is not applicable, i.e., estimation of $K_{\mathrm{I,max}}$ for fracture assessment must involve 3D crack analysis that includes the interactions effect among the cracks. On the other hand, when $\varphi \geq 4$, the maximum Mode I SIF, $K_{\mathrm{I,max}}$ always occur at the crack with the largest crack. This zone can be referred to Size Dominant Zone, SDZ. In this zone, it is possible to apply SDM models because the location of

$K_{\mathrm{I,max}}$ is known. Furthermore, the upper and lower bounds of the interaction factor can be estimated from Table 5.2.

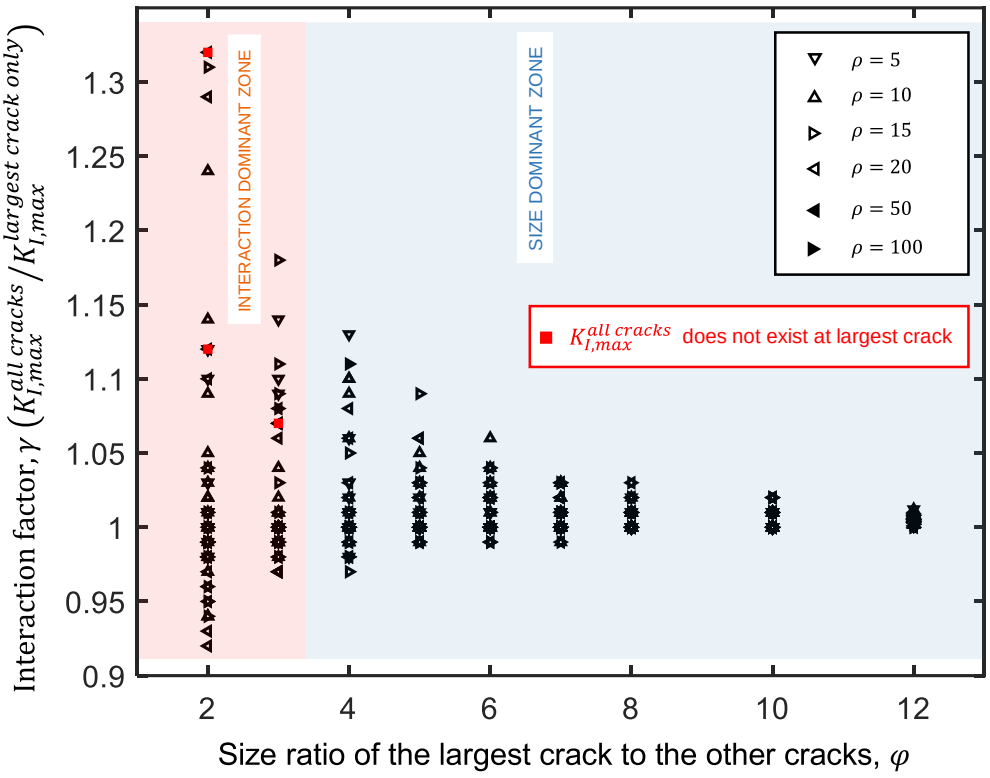

Fig. 5.6 Interaction factors for different size ratios as given in problem Fig. 5.4

Table 5.2 Upper and lower bounds of the interaction factor of problem in Fig. 5.4

φ	Lower bound	Upper bound
4	0.97	1.13
5	0.99	1.09
6	0.99	1.06
7	0.99	1.03
8	1.00	1.03
10	1.00	1.02
12	1.00	1.001

In summary, Fig. 5.6 provides a simple graphical tool to determine when SDM is applicable to multiple crack problems and also a method to include the interaction effect in SDM without performing 3D crack interaction analysis which are usually computationally challenging and expensive. In future research, the method proposed in this section will be extended to other loading types, arbitrary crack orientations and internal cracks.

According to the result discussion above, the following are the answers to the research questions of this section.

- Is assumption that $K_{\mathrm{I,max}}$ should occur at the crack with the largest size always valid?

  Not always valid. If the largest size is less than 4 times the average size, $K_{\mathrm{I,max}}$ could exist outside the largest crack (Interaction Dominant Zone, IDZ). When the largest size is at least 4 times the average size, $\mathrm{K_{I,max}}$ always exist at the largest crack (Size Dominant Zone, SDZ).

- What is the influence of crack density on $\mathrm{K_{I,max}}$?

  Crack density have minor influence on $\mathrm{K_{I,max}}$.

- What is the estimation error when interaction effect is ignored in calculation of $K_{\mathrm{I,max}}$?

  According to Fig. 5.6, the estimation error diminishes as size ratio, φ increases. In SDZ, upper and lower bound of the estimate error is given in Table 5.2.

CHAPTER 6. General conclusion

6.1 Major contributions and findings from this study

This study aimed to advance fracture mechanic based models that are used in the assessment of engineering problems whose fracture processes are dominated by multiple interacting cracks. The primary focus was the development of an efficient method for numerical analysis of SIFs for multiple, 3-D, distributed, semi-elliptical cracks on the surface of a semi-infinite elastic body under arbitrary loading condition. A complementary objective was to develop a method for quantitative characterisation of the spatial distribution of surface defects and cracks. The following are the main findings and conclusions drawn from the results of the present study.

A novel method for the numerical analysis of stress intensity factors (SIFs) was developed for multiple, 3-D-distributed, semi-elliptical cracks on the surface of a semi-infinite elastic body under arbitrary loading conditions. Emphasis was placed on the nature of interactions between cracks, with examination by the distributed infinitesimal dislocation loop technique, an eigenstrain method. SIFs of 100 distributed surface cracks were acquired in approximately 15 min when calculated on a standard personal computer, owing to the numerical integration approaches and meshing procedure adopted.

Some examples were implemented to elucidate the effects of aspect ratio, spacing distance in the loading direction, difference in size and non-alignment of parallel cracks on the nature of the interaction effect. The innovative multiple 3-D crack analysis procedure was combined with the Monte-Carlo simulation approach to develop a new method for material quality assessment, in consideration of the interaction effect of distributed material defects and loading types. As another practical application, the novel numerical analysis was utilized to develop a

simple graphical tool to determine when multiple crack problems could be transformed to single crack problem, hereby focusing on the crack with the largest size.

Analytical and experimental approach was utilized to establish a Nearest-Neighbour Analysis (NNA)-based procedure, identified as the QR method, as a suitable method to quantitatively characterise the spatial distribution of surface features such as cracks, inclusions, and corrosion pits. Depending on the respective values of Q and R, the featured surface-populations can be classified as random, clustered, or regular sets, or clusters with superimposed backgrounds. Another NNA-based procedure known as the Schwartz method was introduced to identify clusters of surface features from background-sets. After the exposure of a carbon steel to a 3.5%-NaCl-solution mist, the results derived from observation of corrosion-pit initiation and growth were used to justify the applicability of this approach. The combined QR/Schwartz method was suggested as a novel procedure for inclusion-rating and quality-control of materials destined for use in applications where multiple crack problem is an issue. For example, steel structures that will experience operation in corrosive environments. These techniques have potential for determining the spatial distribution of corrosion fatigue-cracks, using fracture mechanics-based, corrosion-fatigue, strength-prediction models such as those proposed by Kitagawa *et al.* and Cawley *et al.* [10, 78]

6.2 Recommendations for future work

The major outcome from the present study is the fast and computationally efficient tool for the numerical analysis of stress intensity factors (SIFs) for multiple, 3-D-distributed cracks in an elastic body under arbitrary loading conditions. The equations developed in the basic formulation is generic in nature and applicable to all 3-D cracks in an infinite and semi-infinite body under arbitrary loading condition. In addition, it is independent of the geometry of the

cracks and applicable to surface cracks and internal cracks. However, subsequent numerical formulation focused on semi-elliptical surface cracks in a semi-infinite body. Future research should focus on expanding the tool to be capable of analysis for cracks of arbitrary shapes.

Furthermore, the basic formulation does not include friction and penetration condition for the faces of the cracks. This means that effect of crack surface friction is not included in the analysis. It also implies that the upper and lower faces of a crack can penetrate each other when the interacting cracks are extremely close. Therefore, without additional surface-to-surface contact boundary condition in the basic formulation, there is limitation to how close the cracks can be to avoid the penetration effect. For distributed semi-elliptical surface cracks under tension, Fig. 6.1 provides a practical guideline to estimate how close the neighbouring cracks needs to be before this additional condition becomes necessary.

In most practical cases, the interacting cracks will fulfil the criteria in Fig. 6.1. Nevertheless, future research should focus on extension of the basic formulation to include surface-to surface contact condition. This will enable study on interacting effect of multiple cracks under combined loading such as combination of compressive stress and shear stress. This is type of loading is often encountered in rolling contact fatigue where multiple cracks initiate at distributed inclusion sites subjected to cyclic shear stress and static compressive stress [2].

In fatigue crack growth models, the estimation of SIFs is an essential step in the analysis. Nearly all existing models do not include interaction effect in their SIFs estimation. This study proposes that although only the major crack is growing, the presence of the other minor cracks has effect on the K_{I} of the major crack. The effect could be positive (reduction in K_{I}) or negative (increase in K_{I}). Therefore, including the interaction effect will result to significant

improvement in the performance and accuracy of these models. Future study should correlate the predictions and claims from this study to actual fatigue life.

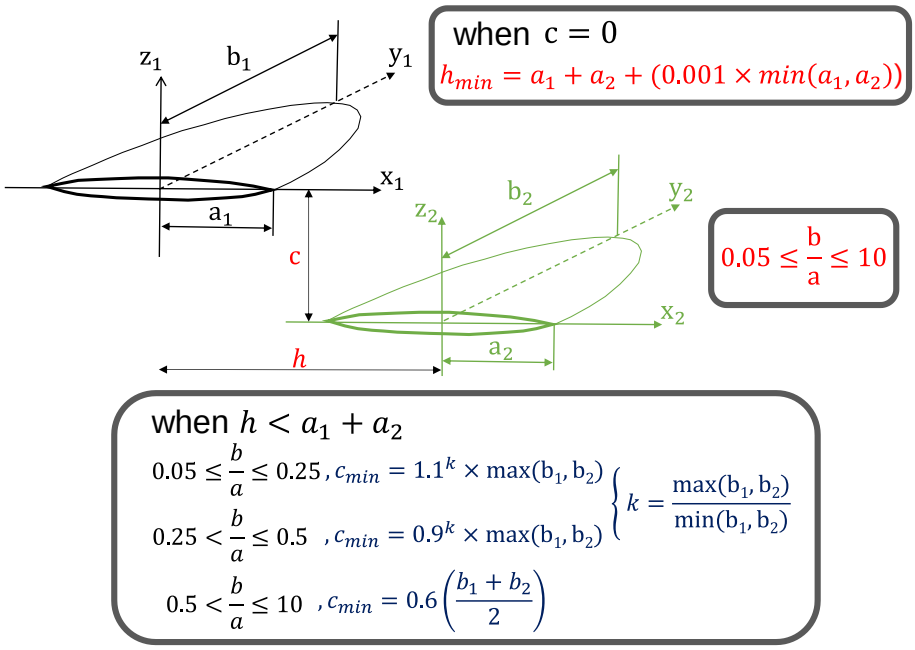

Fig. 6.1 Threshold distance of two interacting elliptical crack without surface-to-surface contact boundary condition.

REFERENCES

1. McAdam Jr. D.J, Fatigue and Corrosion Fatigue of Metals, Proc. Int. Cong. Testing Materials 1927;1.305.
2. Murakami Y, Metal Fatigue: Effects of Small Defects and Nonmetallic Inclusions, Elsevier, Oxford, UK, 2002.
3. Kawai S, Kasai K, Consideration of allowable stress of corrosion fatigue (focused on the influence of pitting), Fatigue Fract. Engng. Mater. 1985; 8: 115−127.
4. Yamashita Y, Murakami T, Mihara R, Okada M, Murakami Y. Defect analysis and fatigue design basis for Ni-based superalloy 718 manufactured by selective laser melting. Int J Fatigue 2018;117:485-95.
5. Molaei R, Fatemi A. Crack paths in additive manufactured metallic materials subjected to multiaxial cyclic loads including surface roughness, HIP, and notch effects. Int J Fatigue 2019;124:558-70.
6. Madia M, Schork B, Bernhard J, Kaffenberger M. Multiple crack initiation and propagation in weldments under fatigue loading. Procedia Struct Integr 2017;7:423-30.
7. Åman M, Wada K, Matsunaga H, Remes H, Marquis G. The influence of interacting small defects on the fatigue limits of a pure iron and a bearing steel. Int J Fatigue 2020;135:105560.
8. Åman M, Okasaki S, Matsunaga H, Marquis GB, Remes H. Interaction effect of adjacent small defects on the fatigue limit of a medium carbon steel. Fatigue Fract Eng Mater Struct 2017;40:130-44.
9. Molaei R, Fatemi A. Crack paths in additive manufactured metallic materials subjected to multiaxial cyclic loads including surface roughness, HIP, and notch effects. Int J Fatigue 2019;124:558-70.

10. Kitagawa H, Fujita T, Miyazawa K. Small Randomly Distributed Cracks in Corrosion Fatigue, Corrosion-Fatigue Technology, ASTM STP. 1978;642:98−114.
11. Zerbst U, Madia M, Klinger C, Bettge D, Murakami Y. Defects as the root cause of fatigue failure of metallic components. Part I: Basic aspects. Engng Failure Anal 2019; 97:777–92.
12. Zerbst U, Madia M, Klinger C, Bettge D, Murakami Y. Defects as the root cause of fatigue failure of metallic components. Part II: Non-metallic inclusions. Engng Failure Anal 2019; 98:228–39.
13. Zerbst U, Madia M, Klinger C, Bettge D, Murakami Y. Defects as the root cause of fatigue failure of metallic components. Part III: Cavities, dents, corrosion pits, scratches. Engng Failure Anal 2019; 97:759–76.
14. Panasyuk VV, Andreikiv AE, Stadnik MM. Three-dimensional static crack problems solution (a review). Eng Fract Mech 1981;14(2):245-60.
15. Isida M, Tsuru H, Noguchi H. An Analysis for Three Dimensional Cracks. Fatigue Fract Eng Mater Struct 1994;17(7):737-49.
16. Weaver J. Three-dimensional crack analysis. Int J Solids Struct 1977;13(4):321-30.
17. Isida M, Tokumoto A, Noguchi H. Oblique semi-elliptical surface crack in semi-infinite solid subjected to tension. Eng Fract Mech 1990;36(6):889-92.
18. Murakami Y, Isida M. Analysis of Mixed Mode Stress Intensity Factors for Arbitrarily Shaped Inclined Surface Cracks. Trans Japan Soc Mech Eng A 1984;50(455):1359-66.
19. Matsunaga H, Muramoto S, Shomura N, Endo M. Shear Mode Growth and Threshold of Small Fatigue Cracks in SUJ2 Bearing Steel Journal of the Society of Materials Science Japan 2009; 58 (9): 773-780.
20. Kassir M.K, Sih G.C. Three-Dimensional Stress Distribution Around an Elliptical Crack Under Arbitrary Loadings. J Appl Mech 1966;33(3):601-11.

21. Murakami Y. Analysis of stress intensity factors of modes I, II and III for inclined surface cracks of arbitrary shape. Eng Fract Mech 1985;22(1):101-14.
22. Isida M, Noguchi H, Yoshida T. Tension and bending of finite thickness plates with a semi-elliptical surface crack. Int J Fract 1984;26:157-88.
23. Benthem J.P. State of stress at the vertex of a quarter-infinite crack in a half-space. Int J Solids Struct 1977;13(5):479-92.
24. Noda N.A, Kihara T, Beppu D. Variations of stress intensity factor of a semi-elliptical surface crack subjected to mixed mode loading. Int J Fract 2004;127:167-91.
25. He M.Y, Hutchinson J.W. Surface crack subject to mixed mode loading. Eng Fract Mech 2000;65(1):1-14.
26. Murakami Y, Natsume H. Stress Singularity at the Corner Point of 3-D Surface Crack under Mode II Loading. JSME Int J A-Solid M 2002;45(2):161-9.
27. Pook L.P, Berto F, Campagnolo A. State of the art of corner point singularities under in-plane and out-of-plane loading. Eng Fract Mech 2017;174:2-9.
28. Noda N.A, Miyoshi S. Variation of stress intensity factor and crack opening displacement of semi-elliptical surface crack. Int J Fract 1996;75:19-48.
29. Ruiz C, Epstein J. On the variation of the stress intensity factor along the front of a surface flaw. Int J Fract 1985;28:231-8.
30. Chan S.K, Tuba IS, Wilson W.K. On the finite element method in linear fracture mechanics. Eng Fract Mech 1970;2(1):1-17.
31. Kachanov M, Laures J.P. Three-dimensional problems of strongly interacting arbitrarily located penny-shaped cracks. Int J Fract 1989;41:289-313.
32. Fabrikant V.I. Close interaction of coplanar circular cracks under shear loading. Computational Mech 1989;4:181-97.

33. Zhan S, Wang T. Interactions of Penny-shaped Cracks in Three-dimensional Solids. Acta Mech Solida Sin 2006;22:341-53.
34. O'Donoghue P.E, Nishioka T, Atluri S.N. Multiple coplanar embedded elliptical cracks in an infinite solid subject to arbitrary crack face tractions. International Journal of Numerical Methods Eng. 1985;21(3):437-49.
35. Hasib M.A, Sonobe Y, Saimoto A. Improvement of Stress Intensity Factor Analysis Using Overall Defined Basic Density Function on Crack Face. J Multiscale Model 2018;9(1):1750006.
36. Kachanov M. Elastic solids with many cracks: A simple method of analysis. Int J Solids Struct 1987;23(1):23-43.
37. Horii H, Nemat-Nasser S. Elastic fields of interacting inhomogeneities. Int J Solids Struct 1985; 21(7):731-45.
38. Okazaki S, Okuma S, Kevinsanny, Ogawa Y, Kawashima H, Funakoshi Y, Matsunaga H. Unforeseen, negative interaction-effect of adjacent circumferential notches on the fatigue limit of Ni-based superalloy 718. Eng Fract Mech 2021;257:108015.
39. Murakami Y, Nemat-Nasser S. Interacting dissimilar semi-elliptical surface flaws under tension and bending. Eng Fract Mech 1982;16(3):373-86.
40. Murakami Y, Nemat-Nasser S. Growth, and stability of interacting surface flaws of arbitrary shape.
41. Isida M, Yoshida T, Noguchi H. Parallel array of semi-elliptical surface cracks in semi-infinite solid under tension. Eng Fract Mech 1991;39(5):845-50. Eng Fract Mech 1983;17(3):193-210.
42. Moussa W.A, Bell R, Tan C.L. The interaction of two parallel non-coplanar identical surface cracks under tension and bending. Int J Press Vessels Pip 1999;76(3):135-45.

43. Åman M, Berntsson K, Marquis G. An efficient stress intensity factor evaluation method for interacting arbitrary shaped 3D cracks. Theory Appl Fract Mech 2020;109:102767.
44. Hills D.A, Kelly P.A, Dai D.N, Korsunsky A.M. Solution of Crack Problems: The Distributed Dislocation Technique. 1st ed. Netherlands: Springer Dordrecht; 1996.
45. Mura T. Micromechanics of Defects in Solids. 1st ed. The Hague: Martinus Nijhoff Publishers; 1982.
46. Bacon D.J, Groves P.P. The Dislocation in a Semi-Infinite Isotropic Medium. In: Simmons JA, de Witt R, Bullough R, editors. Fundamental Aspects of Dislocation Theory, Washington DC: National Bureau of Standards Special Publication 317, vol. I; 1970, p. 35-45.
47. Mindlin R.D. Force at a point in the interior of a semi-infinite solid. Physics 1936;7:195-202.
48. Hadamard J. Lectures on Cauchy's Problem in Linear Partial Differential Equations. New York: Dover Publications Inc; 1952.
49. Hills D.A, Kelly P.A, Dai D.N, Korsunsky A.M. Solution of Crack Problems: The Distributed Dislocation Technique. 1st ed. Netherlands: Springer Dordrecht; 1996.
50. Bažant Z.P, Estenssoro L.F. Surface singularity and crack propagation. Int J Solids Struct 1979;15(5):405-26.
51. Benthem J.P. The quarter-infinite crack in a half space; Alternative and additional solutions. Int J Solids Struct 1980;16(2):119-30.
52. Murakami Y, Takahashi K, Yamashita T. Quantitative Evaluation of the Effect of Surface Roughness on Fatigue Strength: Effect of Depth and Pitch of Roughness. Trans Jpn Soc Mech Eng A 1997;63(612):1612-19.

53. ISO 4967:2013, Steel- Determination of content of non-metallic inclusions – Micrographic method using standard diagrams. International Organization for Standardization.
54. JIS G 0555:2003, Microscopic testing method for the non-metallic inclusions in steel. Japanese Standards Association.
55. ASTM E45-13, Standard Test Methods for Determining the Inclusion Content of Steel. ASTM International (American Section of the International Association for Testing Materials).
56. Wranglen G. Pitting and Sulphide inclusions in steel, Corrosion Sci. 1974;14:331−349.
57. Boukerrou A, Cottis R.A, Crack Initiation in the corrosion fatigue of structural steels in salt solutions, Corrosion Sci. 1993;35:577−585.
58. Larrosa N.O, Akid R, Ainsworth R.A. Corrosion-fatigue: a review of damage tolerance models, International Materials Review. 2018;63:283−308.
59. Baker M.A, Castle J.E. The initiation of pitting corrosion at MnS inclusions, Corrosion Sci. 1993;34:667−682.
60. Punckt C, Bölscher M, Rotermund H.H, Mikhailov A.S, Organ L, Budiansky N, Scully J.R, Hudson J.L. Sudden onset of pitting corrosion on stainless steel as a critical phenomenon, Science. 2004;305:1133−1136.
61. Ryan M.P, Williams D.E, Chater R.J, Hutton B.M, McPhail D.S. Why stainless steel corrodes, Nature. 2002;415:770−774.
62. López De La Cruz J, Kuniewski S.P, Van Noortwijk J.M, Gutiérrez M.A. Spatial Nonhomogeneous Poisson Process in Corrosion Management, J. Electrochem. Soc. 2008;155:C396−C406.

63. Budiansky N.D, Organ L, Hudson J.L, Scully J.R. Detection of interactions among localised pitting sites on stainless steel using spatial statistics, J. Electrochem. Soc. 2005;152:B152−B160.
64. López De La Cruz J, Gutiérrez M.A. Spatial statistics of pitting corrosion patterning: Quadrant counts and the non-homogeneous Poisson process, Corrosion Sci. 2008;50:1441−1448.
65. Wu B, Scully J.R, Hudson J.L. Cooperative Stochastic Behavior in Localized Corrosion: I. Model, J. Electrochem. Soc. 1997;144:1614.
66. Lunt T.T, Pride T, Scully J.R, Hudson J.L. Cooperative Stochastic Behavior in Localized Corrosion: II. Experiments, J. Electrochem. Soc. 1997;144:1620.
67. Lunt T.T, Scully J.R, Brusamarello V, Mikhailov A.S, Hudson J.L. Spatial Interactions among Localized Corrosion Sites: Experiments and Modelling, J. Electrochem. Soc. 2002;149:B163.
68. Budiansky N.D, Hudson J.L, Scully J.R. Origins of Persistent Interaction among Localized Corrosion Sites on Stainless Steel, J. Electrochem. Soc. 2004;151:B233.
69. Organ L, Scully J.R, Mikhailov A.S, Hudson J.L. A Spatiotemporal model of interactions among metastable pits and the transition to pitting corrosion, Electrochim. Acta 2005;51:225-241.
70. Organ L, Tiwary Y, Scully J.R, Mikhailov A.S, Hudson J.L. Interactions among metastable pits on heterogenous electrodes, Electrochim. Acta 2007;3:873-885.
71. Jain S, Lim M.L.C, Hudson J.L, Scully J.R. Spreading of intergranular corrosion on the surfaces of sensitized Al-4.4Mg alloys: a general finding, Corros. Sci. 2012;59:136-147.

72. Jain S., Hudson J.L, Scully J.R. Effects of constituent particles and sensitization on surface spreading of intergranular corrosion on a sensitized AA5083 alloy, Electrochim. Acta 2013;108:253-264.
73. Scully J.R, Budiansky N.D, Tiwary Y, Mikhailov A.S, Hudson J.L. An alternative explanation for the abrupt increase at the pitting potential, Corros. Sci. 2008;50:316-324.
74. Clark P.J, Evans F.C. Distance to nearest neighbour as a measure of spatial relationships in population, Ecology. 1954;35:445−453.
75. Shehata M.T, Boyd J.D. Measurement of spatial distribution of inclusions, Inclusions, and their influence on material behaviours, ASM International 1988;123−131.
76. Schwartz H, Exner H.E. The characterisation of the arrangement of feature centroids in planes and volumes, J. Microscopy. 1983;129:155−169.
77. Samuels L.E. Metallographic Polishing by Mechanical Means, Sir Isaac Pitman & Sons Ltd., Melbourne & London, 1967.
78. Cawley N.R, Harlow D.G. Spatial statistics of particles and corrosion pits in 2024-T3 aluminum alloy, J. Mater. Sci. 1996;31:5127−5134.
79. Kawarada H, Masuko N, Yamanagida H. Journal of the Faculty of Engineering, University of Tokyo. 1972;31.

APPENDIX

Appendix A

Derivatives of Stress Components from Points Load - Green Function

$$\frac{d\sigma_{zz}^{P}}{d\zeta}=\frac{1}{8\pi(1-\nu)}\left[-\frac{3(1-2\nu)(z-\zeta)^2}{R_1^5}+\frac{1-2\nu}{R_1^3}+\frac{3(1-2\nu)(5-4\nu)(z-\zeta)^2}{R_2^5}-\frac{(1-2\nu)(5-4\nu)}{R_2^3}+\frac{9(z-\zeta)^2}{R_1^5}-\frac{15(z-\zeta)^4}{R_1^7}-\frac{15(3-4\nu)(z-\zeta)^4}{R_2^7}+\frac{9(3-4\nu)(z-\zeta)^2}{R_2^5}+\frac{12(1-2\nu)(1-\nu)}{R_2(R_2+y+\eta)^2}-\frac{24(1-2\nu)(1-\nu)(z-\zeta)^2}{{R_2}^2(R_2+y+\eta)^3}-\frac{12(1-2\nu)(1-\nu)(z-\zeta)^2}{{R_2}^3(R_2+y+\eta)^2}+\frac{12(1-2\nu)(1-\nu)(3R_2+y+\eta)(z-\zeta)^4}{{R_2}^4(R_2+y+\eta)^4}-\frac{12(1-2\nu)(1-\nu)(z-\zeta)^4}{{R_2}^4(R_2+y+\eta)^3}-\frac{12(1-2\nu)(1-\nu)(3R_2+y+\eta)(z-\zeta)^2}{{R_2}^3(R_2+y+\eta)^3}+\frac{12(1-2\nu)(1-\nu)(3R_2+y+\eta)(z-\zeta)^4}{{R_2}^5(R_2+y+\eta)^3}+\frac{90\eta^2(z-\zeta)^2}{R_2^7}-\frac{18\eta^2}{R_2^5}-\frac{30(3-2\nu)(y+\eta)(z-\zeta)^2}{R_2^7}+\frac{6(3-2\nu)\eta(y+\eta)}{R_2^5}+\frac{210y\eta(z-\zeta)^4}{R_2^9}-\frac{90y\eta(z-\zeta)^2}{R_2^7}\right] \quad [A.1]$$

$$\frac{d\sigma_{zz}^{Q}}{d\xi}=\frac{1}{8\pi(1-\nu)}\left[-\frac{1-2\nu}{R_1^3}+\frac{3(1-2\nu)(x-\xi)^2}{R_1^5}+\frac{3(1-2\nu)(3-4\nu)(x-\xi)^2}{R_2^5}-\frac{(1-2\nu)(3-4\nu)}{R_2^3}+\frac{3(z-\zeta)^2}{R_1^5}-\frac{15(x-\xi)^2(z-\zeta)^2}{R_1^7}-\frac{15(3-4\nu)(x-\xi)^2(z-\zeta)^2}{R_2^7}+\frac{3(3-4\nu)(z-\zeta)^2}{R_2^5}+\frac{4(1-2\nu)(1-\nu)}{R_2(R_2+y+\eta)^2}-\frac{8(1-2\nu)(1-\nu)(x-\xi)^2}{{R_2}^2(R_2+y+\eta)^3}-\frac{4(1-2\nu)(1-\nu)(x-\xi)^2}{{R_2}^3(R_2+y+\eta)^2}+\frac{12(1-2\nu)(1-\nu)(3R_2+y+\eta)(x-\xi)^2(z-\zeta)^2}{{R_2}^4(R_2+y+\eta)^4}-\frac{12(1-2\nu)(1-\nu)(x-\xi)^2(z-\zeta)^2}{{R_2}^4(R_2+y+\eta)^3}-\frac{4(1-2\nu)(1-\nu)(3R_2+y+\eta)(z-\zeta)^2}{{R_2}^3(R_2+y+\eta)^3}+\frac{12(1-2\nu)(1-\nu)(3R_2+y+\eta)(x-\xi)^2(z-\zeta)^2}{{R_2}^5(R_2+y+\eta)^3}+\frac{30\eta^2(x-\xi)^2}{R_2^7}-\frac{6\eta^2}{R_2^5}-\frac{30(1-2\nu)(y+\eta)(x-\xi)^2}{R_2^7}+\frac{6(1-2\nu)\eta(y+\eta)}{R_2^5}+\frac{210y\eta(x-\xi)^2(z-\zeta)^2}{R_2^9}-\frac{30y\eta(z-\zeta)^2}{R_2^7}\right] \quad [A.2]$$

$$\frac{d\sigma_{zz}^{R}}{d\eta}=\frac{1}{8\pi(1-\nu)}\left[-\frac{1-2\nu}{R_1^3}+\frac{3(1-2\nu)(y-\eta)^2}{R_1^5}+\frac{3(z-\zeta)^2}{R_1^5}-\frac{15(y-\eta)^2(z-\zeta)^2}{R_1^7}-\frac{3(1-2\nu)(y+\eta)(4\nu y+4\nu\eta+3\eta-3y)}{R_2^5}-\frac{(1-2\nu)(3-4\nu)}{R_2^3}+\frac{6\eta(2\nu y-y+2\nu\eta)+3(3-4\nu)(z-\zeta)^2-6(1-2\nu)\eta(y+\eta)}{R_2^5}-\frac{15(y+\eta)\left((y-\eta)(z-\zeta)^2(3-4\nu)+2\eta(y+\eta)(2\nu y-y+2\eta\nu)\right)}{R_2^7}+\frac{30\eta(y+\eta)(z-\zeta)^2}{R_2^7}+\frac{30y\eta(z-\zeta)^2}{R_2^7}-\frac{210y\eta(y-\eta)^2(z-\zeta)^2}{R_2^9}-\frac{4(1-2\nu)(1-\nu)(y+\eta)}{R_2^3(R_2+y+\eta)}-\frac{4\left(\frac{y+\eta}{R_2}+1\right)(1-2\nu)(1-\nu)}{R_2(R_2+y+\eta)^2}+\frac{8(1-2\nu)(1-\nu)(y+\eta)(z-\zeta)^2}{R_2^4(R_2+y+\eta)^2}+\frac{8(1-2\nu)(1-\nu)(z-\zeta)^2\left(\frac{y+\eta}{R_2}+1\right)}{R_2^2(R_2+y+\eta)^3}+\frac{12(1-2\nu)(1-\nu)(y+\eta)(z-\zeta)^2}{R_2^5(R_2+y+\eta)}+\frac{4(1-2\nu)(1-\nu)(z-\zeta)^2\left(\frac{y+\eta}{R_2}+1\right)}{R_2^3(R_2+y+\eta)^2}\right] \quad [A.3]$$

$$\frac{d\sigma_{zz}^{P}}{d\xi}=\frac{1}{8\pi(1-\nu)}\left[-\frac{3(1-2\nu)(z-\zeta)(x-\xi)}{R_1^5}+\frac{3(1-2\nu)(5-4\nu)(z-\zeta)(x-\xi)}{R_2^5}-\frac{15(z-\zeta)^3(x-\xi)}{R_1^7}-\frac{15(3-4\nu)(z-\zeta)^3(x-\xi)}{R_2^7}-\frac{24(1-2\nu)(1-\nu)(z-\zeta)(x-\xi)}{{R_2}^2(R_2+y+\eta)^3}-\frac{12(1-2\nu)(1-\nu)(z-\zeta)(x-\xi)}{{R_2}^3(R_2+y+\eta)^2}+\frac{12(1-2\nu)(1-\nu)(3R_2+y+\eta)(z-\zeta)^3(x-\xi)}{{R_2}^4(R_2+y+\eta)^4}-\frac{12(1-2\nu)(1-\nu)(z-\zeta)^3(x-\xi)}{{R_2}^4(R_2+y+\eta)^3}+\frac{12(1-2\nu)(1-\nu)(3R_2+y+\eta)(z-\zeta)^3(x-\xi)}{{R_2}^5(R_2+y+\eta)^3}+\frac{90\eta^2(z-\zeta)(x-\xi)}{R_2^7}-\frac{30(3-2\nu)(y+\eta)(z-\zeta)(x-\xi)}{R_2^7}+\frac{210y\eta(z-\zeta)^3(x-\xi)}{R_2^9}\right] \quad [A.4]$$

$$\frac{d\sigma_{zz}^{Q}}{d\zeta}=\frac{1}{8\pi(1-\nu)}\left[\frac{3(1-2\nu)(z-\zeta)(x-\xi)}{R_1^5}+\frac{3(1-2\nu)(3-4\nu)(z-\zeta)(x-\xi)}{R_2^5}+\frac{6(z-\zeta)(x-\xi)}{R_1^5}-\frac{15(z-\zeta)^3(x-\xi)}{R_1^7}-\frac{15(3-4\nu)(z-\zeta)^3(x-\xi)}{R_2^7}+\frac{6(3-4\nu)(z-\zeta)(x-\xi)}{R_2^5}-\frac{8(1-2\nu)(1-\nu)(z-\zeta)(x-\xi)}{{R_2}^2(R_2+y+\eta)^3}-\frac{4(1-2\nu)(1-\nu)(z-\zeta)(x-\xi)}{{R_2}^3(R_2+y+\eta)^2}+\frac{12(1-2\nu)(1-\nu)(3R_2+y+\eta)(z-\zeta)^3(x-\xi)}{{R_2}^4(R_2+y+\eta)^4}-\frac{12(1-2\nu)(1-\nu)(z-\zeta)^3(x-\xi)}{{R_2}^4(R_2+y+\eta)^3}-\frac{8(1-2\nu)(1-\nu)(3R_2+y+\eta)(z-\zeta)(x-\xi)}{{R_2}^3(R_2+y+\eta)^3}+\frac{12(1-2\nu)(1-\nu)(3R_2+y+\eta)(z-\zeta)^3(x-\xi)}{{R_2}^5(R_2+y+\eta)^3}+\frac{30\eta^2(z-\zeta)(x-\xi)}{R_2^7}-\frac{30(1-2\nu)\eta(y+\eta)(z-\zeta)(x-\xi)}{R_2^7}+\frac{210y\eta(z-\zeta)^3(x-\xi)}{R_2^9}-\frac{60\eta y(z-\zeta)(x-\xi)}{R_2^7}\right] \quad [A.5]$$

$$\frac{d\sigma_{zz}^{P}}{d\eta}=\frac{1}{8\pi(1-\nu)}\left[-\frac{3(1-2\nu)(z-\zeta)(y-\eta)}{R_1^5}+\frac{3(1-2\nu)(5-4\nu)(z-\zeta)(y+\eta)}{R_2^5}-\frac{15(z-\zeta)^3(y-\eta)}{R_1^7}-\frac{15(3-4\nu)(z-\zeta)^3(y+\eta)}{R_2^7}-\frac{12(1-2\nu)(1-\nu)(z-\zeta)(y+\eta)}{{R_2}^3(R_2+y+\eta)^2}-\frac{24(1-2\nu)(1-\nu)(z-\zeta)\left(\frac{y+\eta}{R_2}+1\right)}{R_2(R_2+y+\eta)^2}-\frac{4(1-2\nu)(1-\nu)(z-\zeta)^3\left(\frac{3(y+\eta)}{R_2}+1\right)}{{R_2}^3(R_2+y+\eta)^3}+\frac{12(1-2\nu)(1-\nu)(z-\zeta)^3(y+\eta)(3R_2+y+\eta)}{{R_2}^5(R_2+y+\eta)^3}+\frac{12(1-2\nu)(1-\nu)(z-\zeta)^3(3R_2+y+\eta)\left(\frac{y+\eta}{R_2}+1\right)}{{R_2}^3(R_2+y+\eta)^4}+\frac{90\eta(z-\zeta)(y-\eta)^2}{R_2^7}+\frac{6\eta(3-2\nu)(z-\zeta)}{R_2^5}-\frac{30(3-2\nu)(z-\zeta)(y+\eta)^2}{R_2^7}-\frac{30\eta(z-\zeta)^3}{R_2^7}+\frac{210y\eta(z-\zeta)^3(y+\eta)}{R_2^9}\right] \quad [A.6]$$

$$\frac{d\sigma_{zz}^{R}}{d\zeta}=\frac{1}{8\pi(1-\nu)}\left[\frac{3(1-2\nu)(z-\zeta)(y-\eta)}{R_1^5}+\frac{6(z-\zeta)(y-\eta)}{R_1^5}-\frac{15(z-\zeta)^3(y-\eta)}{R_1^7}-\frac{3(1-2\nu)(z-\zeta)(4\nu y+4\nu\eta+3\eta-3y)}{R_2^5}-\frac{15(z-\zeta)\left[(3-4\nu)(y-\eta)(z-\zeta)^2+2\eta(2\nu\eta-y+2\nu\eta)(y+\eta)\right]}{R_2^7}+\frac{6(3-4\nu)(z-\zeta)(y-\eta)}{R_2^5}-\frac{210y\eta(z-\zeta)^3(y+\eta)}{R_2^9}+\frac{60\eta y(z-\zeta)(y+\eta)}{R_2^7}-\frac{12(1-2\nu)(1-\nu)(z-\zeta)}{{R_2}^2(R_2+y+\eta)^2}+\frac{12(1-2\nu)(1-\nu)(z-\zeta)^3}{{R_2}^4(R_2+y+\eta)^2}+\frac{8(1-2\nu)(1-\nu)(z-\zeta)^3}{{R_2}^3(R_2+y+\eta)^3}-\frac{12(1-2\nu)(1-\nu)(z-\zeta)}{{R_2}^3(R_2+y+\eta)}+\frac{12(1-2\nu)(1-\nu)(z-\zeta)^3}{{R_2}^5(R_2+y+\eta)}\right] \quad [A.7]$$

$$\frac{d\tau_{xz}^{P}}{d\zeta}=\frac{1}{8\pi(1-\nu)}\left[-\frac{3(1-2\nu)(z-\zeta)(x-\xi)}{R_1^5}+\frac{3(1-2\nu)(z-\zeta)(x-\xi)}{R_2^5}+\frac{6(z-\zeta)(x-\xi)}{R_1^5}-\frac{15(z-\zeta)^3(x-\xi)}{R_1^7}-\frac{15(3-4\nu)(z-\zeta)^3(x-\xi)}{R_2^7}+\frac{6(3-4\nu)(z-\zeta)(x-\xi)}{R_2^5}-\frac{8(1-2\nu)(1-\nu)(z-\zeta)(x-\xi)}{{R_2}^2(R_2+y+\eta)^3}-\frac{4(1-2\nu)(1-\nu)(z-\zeta)(x-\xi)}{{R_2}^3(R_2+y+\eta)^2}+\frac{12(1-2\nu)(1-\nu)(3R_2+y+\eta)(z-\zeta)^3(x-\xi)}{{R_2}^4(R_2+y+\eta)^4}-\frac{12(1-2\nu)(1-\nu)(z-\zeta)^3(x-\xi)}{{R_2}^4(R_2+y+\eta)^3}-\frac{8(1-2\nu)(1-\nu)(3R_2+y+\eta)(z-\zeta)(x-\xi)}{{R_2}^3(R_2+y+\eta)^3}+\frac{12(1-2\nu)(1-\nu)(3R_2+y+\eta)(z-\zeta)^3(x-\xi)}{{R_2}^5(R_2+y+\eta)^3}-\frac{30y\eta(z-\zeta)(x-\xi)}{R_2^7}+\frac{210y\eta(z-\zeta)^3(x-\xi)}{R_2^9}-\frac{60\eta y(z-\zeta)(x-\xi)}{R_2^7}\right] \quad [A.8]$$

$$\frac{d\tau_{xz}^{Q}}{d\xi}=\frac{1}{8\pi(1-\nu)}\left[-\frac{3(1-2\nu)(z-\zeta)(x-\xi)}{R_1^5}+\frac{3(1-2\nu)(z-\zeta)(x-\xi)}{R_2^5}+\frac{6(z-\zeta)(x-\xi)}{R_1^5}-\frac{15(x-\xi)^3(z-\zeta)}{R_1^7}-\frac{15(3-4\nu)(x-\xi)^3(z-\zeta)}{R_2^7}+\frac{6(3-4\nu)(z-\zeta)(x-\xi)}{R_2^5}-\frac{8(1-2\nu)(1-\nu)(z-\zeta)(x-\xi)}{{R_2}^2(R_2+y+\eta)^3}-\frac{4(1-2\nu)(1-\nu)(z-\zeta)(x-\xi)}{{R_2}^3(R_2+y+\eta)^2}+\frac{12(1-2\nu)(1-\nu)(3R_2+y+\eta)(x-\xi)^3(z-\zeta)}{{R_2}^4(R_2+y+\eta)^4}-\frac{12(1-2\nu)(1-\nu)(x-\xi)^3(z-\zeta)}{{R_2}^4(R_2+y+\eta)^3}-\frac{8(1-2\nu)(1-\nu)(3R_2+y+\eta)(z-\zeta)(x-\xi)}{{R_2}^3(R_2+y+\eta)^3}+\frac{12(1-2\nu)(1-\nu)(3R_2+y+\eta)(z-\zeta)^3(x-\xi)}{{R_2}^5(R_2+y+\eta)^3}-\frac{30y\eta(z-\zeta)(x-\xi)}{R_2^7}+\frac{210y\eta(x-\xi)^3(z-\zeta)}{R_2^9}-\frac{60\eta y(z-\zeta)(x-\xi)}{R_2^7}\right] \quad [A.9]$$

$$\frac{d\tau_{xz}^{R}}{d\eta}=\frac{1}{8\pi(1-\nu)}\left[\frac{3(z-\zeta)(x-\xi)}{R_1^5}-\frac{15(z-\zeta)(x-\xi)(y-\eta)^2}{R_1^7}+\frac{3(3-4\nu)(z-\zeta)(x-\xi)}{R_2^5}-\frac{15(3-4\nu)(z-\zeta)(x-\xi)(y-\eta)(y+\eta)}{R_2^7}+\frac{8(1-2\nu)(1-\nu)(z-\zeta)(x-\xi)(y+\eta)}{{R_2}^4(R_2+y+\eta)^2}+\frac{8(1-2\nu)(1-\nu)(z-\zeta)(x-\xi)\left(\frac{y+\eta}{R_2}+1\right)}{{R_2}^2(R_2+y+\eta)^3}+\frac{12(1-2\nu)(1-\nu)(z-\zeta)(x-\xi)(y+\eta)}{{R_2}^5(R_2+y+\eta)}+\frac{4(1-2\nu)(1-\nu)(z-\zeta)(x-\xi)\left(\frac{y+\eta}{R_2}+1\right)}{{R_2}^3(R_2+y+\eta)^2}+\frac{30\eta(z-\zeta)(x-\xi)(y+\eta)}{R_2^7}+\frac{30y\eta(z-\zeta)(x-\xi)}{R_2^7}-\frac{210y\eta(z-\zeta)(x-\xi)(y+\eta)^2}{R_2^9}\right] \quad [A.10]$$

$$\frac{d\tau_{xz}^{P}}{d\xi}=\frac{1}{8\pi(1-\nu)}\left[\frac{1-2\nu}{R_1^3}+\frac{3(1-2\nu)(x-\xi)^2}{R_1^5}-\frac{(1-2\nu)}{R_2^3}+\frac{3(1-2\nu)(x-\xi)^2}{R_2^5}+\frac{3(z-\zeta)^2}{R_1^5}-\frac{15(x-\xi)^2(z-\zeta)^2}{R_1^7}-\frac{15(3-4\nu)(x-\xi)^2(z-\zeta)^2}{R_2^7}+\frac{3(3-4\nu)(z-\zeta)^2}{R_2^5}+\frac{4(1-2\nu)(1-\nu)}{R_2(R_2+y+\eta)^2}-\frac{8(1-2\nu)(1-\nu)(x-\xi)^2}{{R_2}^2(R_2+y+\eta)^3}-\frac{4(1-2\nu)(1-\nu)(x-\xi)^2}{{R_2}^3(R_2+y+\eta)^2}+\frac{12(1-2\nu)(1-\nu)(3R_2+y+\eta)(x-\xi)^2(z-\zeta)^2}{{R_2}^4(R_2+y+\eta)^4}-\frac{12(1-2\nu)(1-\nu)(x-\xi)^2(z-\zeta)^2}{{R_2}^4(R_2+y+\eta)^3}-\frac{4(1-2\nu)(1-\nu)(3R_2+y+\eta)(z-\zeta)^2}{{R_2}^3(R_2+y+\eta)^3}+\frac{12(1-2\nu)(1-\nu)(3R_2+y+\eta)(x-\xi)^2(z-\zeta)^2}{{R_2}^5(R_2+y+\eta)^3}+\frac{6y\eta}{R_2^5}-\frac{30y\eta(x-\xi)^2}{R_2^7}+\frac{210y\eta(x-\xi)^2(z-\zeta)^2}{R_2^9}-\frac{30y\eta(z-\zeta)^2}{R_2^7}\right] \quad [A.11]$$

$$\frac{d\tau_{xz}^{Q}}{d\zeta}=\frac{1}{8\pi(1-\nu)}\left[\frac{1-2\nu}{R_1^3}+\frac{3(1-2\nu)(z-\zeta)^2}{R_1^5}-\frac{(1-2\nu)}{R_2^3}+\frac{3(1-2\nu)(z-\zeta)^2}{R_2^5}+\frac{3(x-\xi)^2}{R_1^5}-\frac{15(x-\xi)^2(z-\zeta)^2}{R_1^7}-\frac{15(3-4\nu)(x-\xi)^2(z-\zeta)^2}{R_2^7}+\frac{3(3-4\nu)(x-\xi)^2}{R_2^5}+\frac{4(1-2\nu)(1-\nu)}{R_2(R_2+y+\eta)^2}-\frac{8(1-2\nu)(1-\nu)(z-\zeta)^2}{{R_2}^2(R_2+y+\eta)^3}-\frac{4(1-2\nu)(1-\nu)(z-\zeta)^2}{{R_2}^3(R_2+y+\eta)^2}+\frac{12(1-2\nu)(1-\nu)(3R_2+y+\eta)(x-\xi)^2(z-\zeta)^2}{{R_2}^4(R_2+y+\eta)^4}-\frac{12(1-2\nu)(1-\nu)(x-\xi)^2(z-\zeta)^2}{{R_2}^4(R_2+y+\eta)^3}-\frac{4(1-2\nu)(1-\nu)(3R_2+y+\eta)(x-\xi)^2}{{R_2}^3(R_2+y+\eta)^3}+\frac{12(1-2\nu)(1-\nu)(3R_2+y+\eta)(x-\xi)^2(z-\zeta)^2}{{R_2}^5(R_2+y+\eta)^3}+\frac{6y\eta}{R_2^5}-\frac{30y\eta(z-\zeta)^2}{R_2^7}+\frac{210y\eta(x-\xi)^2(z-\zeta)^2}{R_2^9}-\frac{30y\eta(x-\xi)^2}{R_2^7}\right] \quad [A.12]$$

$$\frac{d\tau_{xz}^{P}}{d\eta}=\frac{1}{8\pi(1-\nu)}\left[-\frac{3(1-2\nu)(x-\xi)(y-\eta)}{R_1^5}+\frac{3(1-2\nu)(x-\xi)(y+\eta)}{R_2^5}-\frac{15(z-\zeta)^2(x-\xi)(y-\eta)}{R_1^7}-\frac{15(3-4\nu)(z-\zeta)^2(x-\xi)(y+\eta)}{R_2^7}-\frac{4(1-2\nu)(1-\nu)(x-\xi)(y+\eta)}{{R_2}^3(R_2+y+\eta)^2}-\frac{8(1-2\nu)(1-\nu)(x-\xi)\left(\frac{y+\eta}{R_2}+1\right)}{R_2(R_2+y+\eta)^2}-\frac{4(1-2\nu)(1-\nu)(z-\zeta)^2(x-\xi)\left(\frac{3(y+\eta)}{R_2}+1\right)}{{R_2}^3(R_2+y+\eta)^3}+\frac{12(1-2\nu)(1-\nu)(z-\zeta)^2(x-\xi)(y+\eta)(3R_2+y+\eta)}{{R_2}^5(R_2+y+\eta)^3}+\frac{12(1-2\nu)(1-\nu)(z-\zeta)^2(x-\xi)(3R_2+y+\eta)\left(\frac{y+\eta}{R_2}+1\right)}{{R_2}^3(R_2+y+\eta)^4}-\frac{30y\eta(x-\xi)(y-\eta)}{R_2^7}+\frac{6\eta(x-\xi)}{R_2^5}-\frac{30\eta(z-\zeta)^2(x-\xi)}{R_2^7}+\frac{210y\eta(z-\zeta)^2(x-\xi)(y+\eta)}{R_2^9}\right] \quad [A.13]$$

$$\frac{d\tau_{xz}^{R}}{d\zeta}=\frac{1}{8\pi(1-\nu)}\left[\frac{3(x-\xi)(y-\eta)}{R_1^5}-\frac{15(z-\zeta)^2(x-\xi)(y-\eta)}{R_1^7}-\frac{15(3-4\nu)(z-\zeta)^2(x-\xi)(y-\eta)}{R_2^7}+\frac{3(3-4\nu)(x-\xi)(y-\eta)}{R_2^5}-\frac{4(1-2\nu)(1-\nu)(x-\xi)}{{R_2}^2(R_2+y+\eta)^2}+\frac{8(1-2\nu)(1-\nu)(z-\zeta)^2(x-\xi)}{{R_2}^4(R_2+y+\eta)^2}+\frac{8(1-2\nu)(1-\nu)(z-\zeta)^2(x-\xi)}{{R_2}^3(R_2+y+\eta)^3}-\frac{4(1-2\nu)(1-\nu)(x-\xi)}{{R_2}^3(R_2+y+\eta)}+\frac{4(1-2\nu)(1-\nu)(z-\zeta)^2(x-\xi)}{{R_2}^4(R_2+y+\eta)^2}+\frac{12(1-2\nu)(1-\nu)(z-\zeta)^2(x-\xi)}{{R_2}^5(R_2+y+\eta)}-\frac{210y\eta(z-\zeta)^2(x-\xi)(y+\eta)}{R_2^9}+\frac{30y\eta(x-\xi)(y+\eta)}{R_2^7}\right] \quad A.14]$$

$$\frac{d\tau_{yz}^{P}}{d\zeta}=\frac{1}{8\pi(1-\nu)}\left[-\frac{3(1-2\nu)(z-\zeta)(y-\eta)}{R_1^5}+\frac{3(1-2\nu)(z-\zeta)(y-\eta)}{R_2^5}+\frac{6(z-\zeta)(y-\eta)}{R_1^5}-\frac{15(z-\zeta)^3(y-\eta)}{R_1^7}+\frac{6(3-4\nu)(z-\zeta)(y+\eta)}{R_2^5}-\frac{15(3-4\nu)(z-\zeta)^3(y+\eta)}{R_2^7}-\frac{30y\eta(z-\zeta)(y+\eta)}{R_2^7}+\frac{30(1-2\nu)(z-\zeta)^3\eta}{R_2^7}-\frac{12(1-2\nu)\eta(z-\zeta)}{R_2^5}-\frac{60\eta y(z-\zeta)(y+\eta)}{R_2^7}+\frac{210y\eta(x-\xi)^3(z-\zeta)}{R_2^9}\right] \quad [A.15]$$

$$\frac{d\tau_{yz}^{Q}}{d\xi}=\frac{1}{8\pi(1-\nu)}\left[\frac{3(z-\zeta)(y-\eta)}{R_1^5}-\frac{15(z-\zeta)(x-\xi)^2(y-\eta)}{R_1^7}+\frac{3(3-4\nu)(z-\zeta)(y+\eta)}{R_2^5}-\frac{15(3-4\nu)(z-\zeta)(x-\xi)^2(y+\eta)}{R_2^7}+\frac{30(1-2\nu)\eta(z-\zeta)(x-\xi)^2}{R_2^7}-\frac{6(1-2\nu)(z-\zeta)\eta}{R_2^5}-\frac{30y\eta(z-\zeta)(y+\eta)}{R_2^7}+\frac{210y\eta(z-\zeta)(x-\xi)^2(y+\eta)}{R_2^9}\right] \quad [A.16]$$

$$\frac{d\tau_{yz}^{R}}{d\eta}=\frac{1}{8\pi(1-\nu)}\left[-\frac{3(1-2\nu)(z-\zeta)(y-\eta)}{R_1^5}+\frac{3(1-2\nu)(z-\zeta)(y+\eta)}{R_2^5}+\frac{6(z-\zeta)(y-\eta)}{R_1^5}-\frac{15(y-\eta)^3(z-\zeta)}{R_1^7}-\frac{3(z-\zeta)[3\eta-(3-4\nu)(y+\eta)-(3-4\nu)y]}{R_2^5}+\frac{15(z-\zeta)(y+\eta)[\eta(3y+\eta)-(3-4\nu)(y+\eta)y]}{R_2^7}-\frac{210y\eta(y+\eta)^3(z-\zeta)}{R_2^9}+\frac{60\eta y(z-\zeta)(y+\eta)}{R_2^7}+\frac{30(z-\zeta)(y+\eta)^2\eta}{R_2^7}\right] \quad [A.17]$$

$$\frac{d\tau_{yz}^{P}}{d\xi}=\frac{1}{8\pi(1-\nu)}\left[-\frac{3(1-2\nu)(x-\xi)(y-\eta)}{R_1^5}+\frac{3(1-2\nu)(x-\xi)(y-\eta)}{R_2^5}-\frac{15(z-\zeta)^2(x-\xi)(y-\eta)}{R_1^7}-\frac{15(3-4\nu)(z-\zeta)^2(x-\xi)(y+\eta)}{R_2^7}-\frac{30y\eta(x-\xi)(y-\eta)}{R_2^7}+\frac{30(1-2\nu)\eta(z-\zeta)^2(x-\xi)}{R_2^7}+\frac{210y\eta(z-\zeta)^2(x-\xi)(y+\eta)}{R_2^9}\right] \quad [A.18]$$

$$\frac{d\tau_{yz}^{Q}}{d\zeta}=\frac{1}{8\pi(1-\nu)}\left[\frac{3(x-\xi)(y-\eta)}{R_1^5}-\frac{15(x-\xi)(z-\zeta)^2(y-\eta)}{R_1^7}+\frac{3(3-4\nu)(x-\xi)(y+\eta)}{R_2^5}-\frac{15(3-4\nu)(x-\xi)(z-\zeta)^2(y+\eta)}{R_2^7}+\frac{30(1-2\nu)\eta(x-\xi)(z-\zeta)^2}{R_2^7}-\frac{6(1-2\nu)(x-\xi)\eta}{R_2^5}-\frac{30y\eta(x-\xi)(y+\eta)}{R_2^7}+\frac{210y\eta(x-\xi)(z-\zeta)^2(y+\eta)}{R_2^9}\right] \quad [A.19]$$

$$\frac{d\tau_{yz}^{P}}{d\eta}=\frac{1}{8\pi(1-\nu)}\left[-\frac{3(1-2\nu)(y-\eta)^2}{R_1^5}+\frac{1-2\nu}{R_1^3}-\frac{1-2\nu}{R_2^3}+\frac{3(1-2\nu)(y-\eta)(y+\eta)}{R_2^5}+\frac{3(z-\zeta)^2}{R_1^5}-\frac{15(y-\eta)^2(z-\zeta)^2}{R_1^7}-\frac{15(3-4\nu)(y+\eta)^2(z-\zeta)^2}{R_2^7}+\frac{3(3-4\nu)(z-\zeta)^2}{R_2^5}+\frac{6\eta(y+\eta)}{R_2^5}+\frac{6y\eta}{R_2^5}-\frac{30y\eta(y+\eta)^2}{R_2^7}+\frac{30(1-2\nu)(z-\zeta)^2(y+\eta)\eta}{R_2^7}+\frac{210y\eta(y+\eta)^2(z-\zeta)^2}{R_2^9}-\frac{30y\eta(z-\zeta)^2}{R_2^7}-\frac{30\eta(z-\zeta)^2(y+\eta)}{R_2^7}\right] \quad [A.20]$$

$$\frac{d\tau_{yz}^{R}}{d\zeta}=\frac{1}{8\pi(1-\nu)}\left[-\frac{3(1-2\nu)(z-\zeta)^2}{R_1^5}+\frac{1-2\nu}{R_1^3}-\frac{1-2\nu}{R_2^3}+\frac{3(1-2\nu)(z-\zeta)^2}{R_2^5}+\frac{3(y-\eta)^2}{R_1^5}-\frac{15(y-\eta)^2(z-\zeta)^2}{R_1^7}+\frac{15(z-\zeta)^2[\eta(3y+\eta)-y(y+\eta)(3-4\nu)]}{R_2^7}-\frac{3\eta(3y+\eta)-3y(3-4\nu)(y+\eta)}{R_2^5}+\frac{30y\eta(y+\eta)^2}{R_2^7}-\frac{210y\eta(y+\eta)^2(z-\zeta)^2}{R_2^9}\right] \quad [A.21]$$

Where,

$$R_1=\sqrt{(x-\xi)^2+(y-\eta)^2+(z-\zeta)^2}$$

$$R_2=\sqrt{(x-\xi)^2+(y+\eta)^2+(z-\zeta)^2}$$

Appendix B

MATLAB code for SIF analysis of distributed, semi-elliptical, surface cracks in a semi-infinite body

Description:

```
function [SIFscrack1,SIFscrack2] =
SIFs_EllipticSurfaceCrack(SigmaZZInf,SigmaXZInf,SigmaYZInf)
tic;
G = 79300 ;
v = 0; % Poisson ratio is zero
Num = 3 ;    %Each crack is divided into Num elements.
n = 2;       % Number of cracks.
Ne = Num*n;  % Total Number of elements.

a1 = 1.0; % Major radius of the first crack
a2 = 1*a1;

b1 = 1.0;  % Minor radius of the first crack
b2 = 1*b1;

xorigin_coord = [0;0];
yorigin_coord = [0;0];
zorigin_coord = [0;0.5];
MajorRadius = [a1;a2];
MinorRadius = [b1;b2];

[K_matrix,Major_Radius,Minor_Radius,ElementData] =
Kmatrix(v,G,xorigin_coord,yorigin_coord,zorigin_coord,MajorRadius,MinorRadius,n,Num);

a = Major_Radius;
b = Minor_Radius;

SIGMA = Stresses_ColloPoints(Ne,SigmaZZInf,SigmaXZInf,SigmaYZInf);

Sigma   = SIGMA*-1;
     fn = K_matrix\Sigma;


fn_bar = (G*fn)/(4*pi);

% For i = 1 crack

KI_1   =zeros(Num,1);
KII_1  =zeros(Num,1);
KIII_1 =zeros(Num,1);

    for j = 1 : Num
       xcn  = ElementData(j,13);
       ycn  = ElementData(j,14);
       beta = atan((a(j,1)*ycn)/(b(j,1)*xcn));
       ell=((sin(beta)*sin(beta))+(((b(j,1)^2)/(a(j,1)^2))*cos(beta)*cos(beta)))^0.25;
       KI_1(j,1)   = ((2*pi*fn_bar(j,1))/b(j,1))*ell;
```

```
       KII_1(j,1)  = ((2*pi*fn_bar(Ne+j,1))/b(j,1))*ell;
       KIII_1(j,1) = ((2*pi*fn_bar(Ne+Ne+j,1))/b(j,1))*ell;
    end

% Resolve shear components (x and y) to normal and tangential

KII1 = zeros(Num,1);
KIII1 = zeros(Num,1);
Ang = zeros(Num,1);

for i = 1 : Num

    KII1(i,1) = (KII_1(i,1)*cos(ElementData(i,15)))  +
(KIII_1(i,1)*sin(ElementData(i,15))) ;
   KIII1(i,1) = (KII_1(i,1)*-sin(ElementData(i,15))) +
(KIII_1(i,1)*cos(ElementData(i,15))) ;
   Ang(i,1)  = ElementData(i,15)/(pi/180);

end

SIFscrack1 = [Ang KI_1 KII1 KIII1];

% For i = n/2 crack (Crack in the second position)

KI_2   =zeros(Num,1);
KII_2  =zeros(Num,1);
KIII_2 =zeros(Num,1);

    for j = 1 : Num
       xcn  = ElementData(j,13);
       ycn  = ElementData(j,14);
       beta = atan((a(j+Num,1)*ycn)/(b(j+Num,1)*xcn));

ell=((sin(beta)*sin(beta))+(((b(j+Num,1)^2)/(a(j+Num,1)^2))*cos(beta)*cos(beta)))^0.25;
       KI_2(j,1)   = ((2*pi*fn_bar(Num+j,1))/b(j+Num,1))*ell;
       KII_2(j,1)  = ((2*pi*fn_bar(Ne+Num+j,1))/b(j+Num,1))*ell;
       KIII_2(j,1) = ((2*pi*fn_bar(Ne+Ne+Num+j,1))/b(j+Num,1))*ell;
    end

% Resolve shear components (x and y) to normal and tangential

KIIm = zeros(Num,1);
KIIIm = zeros(Num,1);
Ang = zeros(Num,1);

for i = 1 : Num

    KIIm(i,1) = (KII_2(i,1)*cos(ElementData(i,15)))  +
(KIII_2(i,1)*sin(ElementData(i,15))) ;
   KIIIm(i,1) = (KII_2(i,1)*-sin(ElementData(i,15))) +
(KIII_2(i,1)*cos(ElementData(i,15))) ;
   Ang(i,1)  = ElementData(i,15)/(pi/180);

end

SIFscrack2 = [Ang KI_2 KIIm KIIIm];

toc
```

```
end
```

Description:

```
function [SIGMA] = Stresses_ColloPoints(Ne,SigmaZZInf,SigmaXZInf,SigmaYZInf)

SigmaZZ = ones(Ne,1)*SigmaZZInf;
SigmaXZ = ones(Ne,1)*SigmaXZInf;
SigmaYZ = ones(Ne,1)*SigmaYZInf;
SIGMA   = [SigmaZZ; SigmaXZ; SigmaYZ];

end
```

Description:

```
function [MESHdata] = EllipseMesh(MajorRadius,MinorRadius,Num)
MESHdata = zeros(Num,15);
EvalPoints = zeros(Num,2);
Edata = zeros(Num+2,3);

tdeg = zeros(Num,1);
thetaEVAL_rad = zeros(Num,1);

a = MajorRadius;
b = MinorRadius;

stepRAD = 180/Num;
tdeg0 = 0;
teval0 = stepRAD/2;

    for j = 0 : Num

      tdeg(j+1,1) = (tdeg0 + (stepRAD*j))*(pi/180);

    end

t = tdeg;

    for j = 0 : Num-1

      thetaEVAL_rad(j+1,1) = (teval0 + (stepRAD*j))*(pi/180);

    end

Edata(1,1) = 1 ;
Node = 1 ;
```

```
    for j = 1 : Num+1
      Node = Node + 1 ;
      Edata(Node,1) = Node;
      if t(j,1)< pi/2
         Edata(Node,2) = (a*b)/(( (b^2) + ((a^2)*(tan(t(j,1)))^2) )^0.5);
         Edata(Node,3) = (a*b)/(( (a^2) + ((b^2)/(tan(t(j,1)))^2) )^0.5);
      else
         Edata(Node,2) = -1*(a*b)/(( (b^2) + ((a^2)*(tan(t(j,1)))^2) )^0.5);
         Edata(Node,3) = (a*b)/(( (a^2) + ((b^2)/(tan(t(j,1)))^2) )^0.5);
      end

    end

Element = 0;
p = 1;
q = 2;

    for i = 1 : Num
      Element = Element+1 ;
      MESHdata(Element,1) = 1 ;
      MESHdata(Element,3) = p+i ;
      MESHdata(Element,2) = q+i ;
    end

    for i = 1 : Num

      MESHdata(i,4) = Edata(MESHdata(i,1),2);
      MESHdata(i,5) = Edata(MESHdata(i,2),2);
      MESHdata(i,6) = Edata(MESHdata(i,3),2);
      MESHdata(i,7) = Edata(MESHdata(i,1),3);
      MESHdata(i,8) = Edata(MESHdata(i,2),3);
      MESHdata(i,9) = Edata(MESHdata(i,3),3);

    end

    for j = 1 : Num

      if thetaEVAL_rad(j,1)< pi/2
         EvalPoints(j,1) = (a*b)/(( (b^2) + ((a^2)*(tan(thetaEVAL_rad(j,1)))^2)
)^0.5);
         EvalPoints(j,2) = (a*b)/(( (a^2) + ((b^2)/(tan(thetaEVAL_rad(j,1)))^2)
)^0.5);
      else
         EvalPoints(j,1) = -1*(a*b)/(( (b^2) +
((a^2)*(tan(thetaEVAL_rad(j,1)))^2) )^0.5);
         EvalPoints(j,2) = (a*b)/(( (a^2) + ((b^2)/(tan(thetaEVAL_rad(j,1)))^2)
)^0.5);
      end

    end

    for i = 1:Num
        x1 = MESHdata(i,4);
        x2 = MESHdata(i,5);
        x3 = MESHdata(i,6);
        y1 = MESHdata(i,7);
        y2 = MESHdata(i,8);
        y3 = MESHdata(i,9);
```

```
        xcoord = [x1 x2 x3];
        ycoord = [y1 y2 y3];

        polyin = polyshape(xcoord,ycoord);
        [MESHdata(i,10),MESHdata(i,11)] = centroid(polyin);
        MESHdata(i,12) = polyarea(xcoord,ycoord);
        MESHdata(i,13) = EvalPoints(i,1);
        MESHdata(i,14) = EvalPoints(i,2);
        MESHdata(i,15) = thetaEVAL_rad(i,1);
    end

end
```

Description:

```
function q = KNN1_alt(x_1,x_2,x_3,y_1,y_2,y_3,MajorRadius,MinorRadius,xcn,ycn)

a = MajorRadius;
b = MinorRadius;

w = @(x,y) (1-(x.^2./a.^2)-(y.^2./b.^2)).^(0.5);
w_cn = w_value(MajorRadius,MinorRadius,xcn,ycn);
[wdiff_x,wdiff_y] = wdiff_value(MajorRadius,MinorRadius,xcn,ycn);

w1 = @ (x,y) w(x,y) - w_cn - ((x-xcn).*(wdiff_x)) - ((y-ycn).*(wdiff_y));
 r = @(x,y) ((x-xcn).^2 + (y-ycn).^2).^(0.5);

fun = @(x,y) w1(x,y)./(r(x,y).^2);
polarfun = @(theta,r) fun(r.*cos(theta),r.*sin(theta));

x1 = x_1-xcn;
y1 = y_1-ycn;
node1ang = atan(y1/x1);

x2 = x_2-xcn;
y2 = y_2-ycn;
node2ang = atan(y2/x2);

x3 =x_3-xcn;
y3 =y_3-ycn;
node3ang = atan(y3/x3);

if     sign(x1)==1 && sign(y1)==1
    node1angle = node1ang;
 elseif sign(x1)==-1 && sign(y1)==1
    node1angle = pi - abs(node1ang);
 elseif sign(x1)==-1 && sign(y1)==-1
    node1angle = pi + abs(node1ang);
 elseif sign(x1)==1 && sign(y1)==-1
    node1angle = (2*pi) - abs(node1ang);
else
```

```
end


if     sign(x2)==1 && sign(y2)==1
    node2angle = node2ang;
 elseif sign(x2)==-1 && sign(y2)==1
    node2angle = pi - abs(node2ang);
 elseif sign(x2)==-1 && sign(y2)==-1
    node2angle = pi + abs(node2ang);
 elseif sign(x2)==1 && sign(y2)==-1
    node2angle = (2*pi) - abs(node2ang);
else

end

if     sign(x3)==1 && sign(y3)==1
    node3angle = node3ang;
 elseif sign(x3)==-1 && sign(y3)==1
    node3angle = pi - abs(node3ang);
 elseif sign(x3)==-1 && sign(y3)==-1
    node3angle = pi + abs(node3ang);
 elseif sign(x3)==1 && sign(y3)==-1
    node3angle = (2*pi) - abs(node3ang);
else

end

m12 = (y2-y1)/(x2-x1);
c12 = y2 - (m12*x2);
R_102 = @(theta) c12./(sin(theta)-(m12.*cos(theta)));

m23 = (y2-y3)/(x2-x3);
c23 = y3 - (m23*x3);
R_302 = @(theta) c23./(sin(theta)-(m23.*cos(theta)));

m31 = (y3-y1)/(x3-x1);
c31 = y1 - (m31*x1);
R_103 = @(theta) c31./(sin(theta)-(m31.*cos(theta)));

nodeXangle = zeros(3,1);
nodeXangle(1,1) = node1angle;
nodeXangle(2,1) = node2angle;
nodeXangle(3,1) = node3angle;
Nang = sort(nodeXangle);

if Nang(1,1)==node1angle && Nang(2,1)==node2angle && Nang(3,1)==node3angle
    L1 =@(theta) R_103(theta);
    L2 =@(theta) R_102(theta);
    L3 =@(theta) R_302(theta);
elseif Nang(1,1)==node1angle && Nang(2,1)==node3angle && Nang(3,1)==node2angle
    L1 =@(theta) R_102(theta);
    L2 =@(theta) R_103(theta);
    L3 =@(theta) R_302(theta);
elseif Nang(1,1)==node2angle && Nang(2,1)==node1angle && Nang(3,1)==node3angle
    L1 =@(theta) R_302(theta);
    L2 =@(theta) R_102(theta);
    L3 =@(theta) R_103(theta);
elseif Nang(1,1)==node2angle && Nang(2,1)==node3angle && Nang(3,1)==node1angle
    L1 =@(theta) R_102(theta);
```

```
    L2 =@(theta) R_302(theta);
    L3 =@(theta) R_103(theta);
elseif Nang(1,1)==node3angle && Nang(2,1)==node1angle && Nang(3,1)==node2angle
    L1 =@(theta) R_302(theta);
    L2 =@(theta) R_103(theta);
    L3 =@(theta) R_102(theta);
elseif Nang(1,1)==node3angle && Nang(2,1)==node2angle && Nang(3,1)==node1angle
    L1 =@(theta) R_103(theta);
    L2 =@(theta) R_302(theta);
    L3 =@(theta) R_102(theta);
else
end

rmax1 = @(theta) L1(theta);
rmax2 = @(theta) L2(theta);
rmax3 = @(theta) L3(theta);

t1 = Nang(1,1);
t2 = Nang(2,1);
t3 = Nang(3,1);

q1 = integral2(polarfun,0,t1,0,rmax1) ;
q2 = integral2(polarfun,t1,t2,0,rmax2) ;
q3 = integral2(polarfun,t2,t3,0,rmax3) ;
q4 = integral2(polarfun,t3,2*pi,0,rmax1);

q = q1+q2+q3+q4;

end
```

Description:

```
function KNN2 = Knn2(x1,x2,x3,y1,y2,y3,MajorRadius,MinorRadius,xcn,ycn)
syms x y

a = MajorRadius;
b = MinorRadius;

w_cn = weight(xcn,ycn,a,b);

w = (1-(x^2/a^2)-(y^2/b^2))^(1/2);
dw_x = diff(w,x);
dw_y = diff(w,y);

x = xcn ;
y = ycn ;
dwx_cn = double(subs(dw_x));
dwy_cn = double(subs(dw_y));

[L, M1, M2] = LineIntegral(x1,x2,x3,y1,y2,y3,xcn,ycn);

KNN2 = L*w_cn + M1*dwx_cn + M2*dwy_cn ;

end
```

Description:

```
function [L,M1,M2] = LineIntegral(x_1,x_2,x_3,y_1,y_2,y_3,xcn,ycn)
syms ti

x1 = x_1-xcn;
y1 = y_1-ycn;
node1ang = atan(y1/x1);

x2 = x_2-xcn;
y2 = y_2-ycn;
node2ang = atan(y2/x2);

x3 =x_3-xcn;
y3 =y_3-ycn;
node3ang = atan(y3/x3);

if     sign(x1)==1 && sign(y1)==1
    node1angle = node1ang;
 elseif sign(x1)==-1 && sign(y1)==1
    node1angle = pi - abs(node1ang);
 elseif sign(x1)==-1 && sign(y1)==-1
    node1angle = pi + abs(node1ang);
 elseif sign(x1)==1 && sign(y1)==-1
    node1angle = (2*pi) - abs(node1ang);
else

end


if     sign(x2)==1 && sign(y2)==1
    node2angle = node2ang;
 elseif sign(x2)==-1 && sign(y2)==1
    node2angle = pi - abs(node2ang);
 elseif sign(x2)==-1 && sign(y2)==-1
    node2angle = pi + abs(node2ang);
 elseif sign(x2)==1 && sign(y2)==-1
    node2angle = (2*pi) - abs(node2ang);
else

end

if     sign(x3)==1 && sign(y3)==1
    node3angle = node3ang;
 elseif sign(x3)==-1 && sign(y3)==1
    node3angle = pi - abs(node3ang);
 elseif sign(x3)==-1 && sign(y3)==-1
    node3angle = pi + abs(node3ang);
 elseif sign(x3)==1 && sign(y3)==-1
    node3angle = (2*pi) - abs(node3ang);
else

end

m12 = (y2-y1)/(x2-x1);
c12 = y2 - (m12*x2);
```

```
R_102 = c12/(sin(ti)-(m12*cos(ti)));

m23 = (y2-y3)/(x2-x3);
c23 = y3 - (m23*x3);
R_302 = c23/(sin(ti)-(m23*cos(ti)));

m31 = (y3-y1)/(x3-x1);
c31 = y1 - (m31*x1);
R_103 = c31/(sin(ti)-(m31*cos(ti)));

nodeXangle = zeros(3,1);
nodeXangle(1,1) = node1angle;
nodeXangle(2,1) = node2angle;
nodeXangle(3,1) = node3angle;
Nang = sort(nodeXangle);

if Nang(1,1)==node1angle && Nang(2,1)==node2angle && Nang(3,1)==node3angle
    L1 = R_103;
    L2 = R_102;
    L3 = R_302;
elseif Nang(1,1)==node1angle && Nang(2,1)==node3angle && Nang(3,1)==node2angle
    L1 = R_102;
    L2 = R_103;
    L3 = R_302;
elseif Nang(1,1)==node2angle && Nang(2,1)==node1angle && Nang(3,1)==node3angle
    L1 = R_302;
    L2 = R_102;
    L3 = R_103;
elseif Nang(1,1)==node2angle && Nang(2,1)==node3angle && Nang(3,1)==node1angle
    L1 = R_102;
    L2 = R_302;
    L3 = R_103;
elseif Nang(1,1)==node3angle && Nang(2,1)==node1angle && Nang(3,1)==node2angle
    L1 = R_302;
    L2 = R_103;
    L3 = R_102;
elseif Nang(1,1)==node3angle && Nang(2,1)==node2angle && Nang(3,1)==node1angle
    L1 = R_103;
    L2 = R_302;
    L3 = R_102;
else
end

ng = 3;
a1 = 0;
b1 = Nang(1,1);
[x,w]=lgwt(ng,a1,b1);
La = 0;
M1a = 0 ;
M2a = 0 ;

   for  j = 1 : ng
     ti = x(j,1);
     Wj = w(j,1);
     La = La + ((1/double(subs(L1)))*Wj);
     M1a = M1a + ((cos(ti)*log(double(subs(L1))))*Wj);
     M2a = M2a + ((sin(ti)*log(double(subs(L1))))*Wj);
   end
```

```
a2 = Nang(1,1);
b2 = Nang(2,1);
[x,w]=lgwt(ng,a2,b2);
Lb = 0;
M1b = 0;
M2b = 0;

   for  j = 1 : ng
     ti = x(j,1);
     Wj = w(j,1);
     Lb = Lb + ((1/double(subs(L2)))*Wj);
     M1b = M1b + ((cos(ti)*log(double(subs(L2))))*Wj);
     M2b = M2b + ((sin(ti)*log(double(subs(L2))))*Wj);
   end

a3 = Nang(2,1);
b3 = Nang(3,1);
[x,w]=lgwt(ng,a3,b3);
Lc = 0;
M1c = 0;
M2c = 0;

   for  j = 1 : ng
     ti = x(j,1);
     Wj = w(j,1);
     Lc = Lc + ((1/double(subs(L3)))*Wj);
     M1c = M1c + ((cos(ti)*log(double(subs(L3))))*Wj);
     M2c = M2c + ((sin(ti)*log(double(subs(L3))))*Wj);
   end

a4 = Nang(3,1);
b4 = 2*pi ;
[x,w]=lgwt(ng,a4,b4);
Ld = 0;
M1d = 0;
M2d = 0;

   for  j = 1 : ng
     ti = x(j,1);
     Wj = w(j,1);
     Ld = Ld + ((1/double(subs(L1)))*Wj);
     M1d = M1d + ((cos(ti)*log(double(subs(L1))))*Wj);
     M2d = M2d + ((sin(ti)*log(double(subs(L1))))*Wj);
   end

   L = -1 * (La + Lb + Lc + Ld) ;
   M1 = M1a + M1b + M1c + M1d ;
   M2 = M2a + M2b + M2c + M2d ;

end
```

Description:

```
function [x,w]=lgwt(N,a,b)
```

```
N=N-1;
N1=N+1; N2=N+2;

xu=linspace(-1,1,N1)';
y=cos((2*(0:N)'+1)*pi/(2*N+2))+(0.27/N1)*sin(pi*xu*N/N2);

L=zeros(N1,N2);
Lp=zeros(N1,N2);

y0=2;

while max(abs(y-y0))>eps

    L(:,1)=1;
    Lp(:,1)=0;

    L(:,2)=y;
    Lp(:,2)=1;

    for k=2:N1
        L(:,k+1)=( (2*k-1)*y.*L(:,k)-(k-1)*L(:,k-1) )/k;
    end

    Lp=(N2)*( L(:,N1)-y.*L(:,N2) )./(1-y.^2);

    y0=y;
    y=y0-L(:,N2)./Lp;

end

x=(a*(1-y)+b*(1+y))/2;

w=(b-a)./((1-y.^2).*Lp.^2)*(N2/N1)^2;

end
```

Description:

```
function [rIzz, rIIzz, rIIIzz, rIxz, rIIxz, rIIIxz, rIyz, rIIyz, rIIIyz] =
IntgTriangle(MajorRadius,MinorRadius,x1,x2,x3,y1,y2,y3,z,x_cm,y_cm,z_cm)
a = MajorRadius;
b = MinorRadius;
v = 0;   %Poisson ratio

fIzz    = @(x,y) (((1-(x.^2./a.^2)-(y.^2./b.^2)).^(1./2))./((((x-x_cm).^2+(y-
y_cm).^2+(z-z_cm).^2).^0.5).^3)).*( 1 + (6.*((z-z_cm).^2)./(((((x-x_cm).^2+(y-
y_cm).^2+(z-z_cm).^2).^0.5).^2))) - (15.*((z-z_cm).^4)./(((((x-x_cm).^2+(y-
y_cm).^2+(z-z_cm).^2).^0.5).^4)))) ;
fIIzz   = @(x,y) (((1-(x.^2./a.^2)-(y.^2./b.^2)).^(1./2))./((((x-x_cm).^2+(y-
y_cm).^2+(z-z_cm).^2).^0.5).^3)).*3.*(x-x_cm).*(((z-z_cm)./(((((x-x_cm).^2+(y-
```

```
y_cm).^2+(z-z_cm).^2).^0.5).^2))) - (5.*((z-z_cm).^3)./(((((x-x_cm).^2+(y-
y_cm).^2+(z-z_cm).^2).^0.5).^4)))) ;
fIIIzz  = @(x,y) (((1-(x.^2./a.^2)-(y.^2./b.^2)).^(1./2))./((((x-x_cm).^2+(y-
y_cm).^2+(z-z_cm).^2).^0.5).^3)).*3.*(y-y_cm).*(((z-z_cm)./(((((x-x_cm).^2+(y-
y_cm).^2+(z-z_cm).^2).^0.5).^2))) - (5.*((z-z_cm).^3)./(((((x-x_cm).^2+(y-
y_cm).^2+(z-z_cm).^2).^0.5).^4)))) ;

fIxz    = @(x,y) (((1-(x.^2./a.^2)-(y.^2./b.^2)).^(1./2))./((((x-x_cm).^2+(y-
y_cm).^2+(z-z_cm).^2).^0.5).^3)).*3.*(x-x_cm).*(((z-z_cm)./(((((x-x_cm).^2+(y-
y_cm).^2+(z-z_cm).^2).^0.5).^2))) - (5.*((z-z_cm).^3)./(((((x-x_cm).^2+(y-
y_cm).^2+(z-z_cm).^2).^0.5).^4)))) ;
fIIxz   = @(x,y) (((1-(x.^2./a.^2)-(y.^2./b.^2)).^(1./2))./((((x-x_cm).^2+(y-
y_cm).^2+(z-z_cm).^2).^0.5).^3)).*( (1+v) - (3.*v.*((y-y_cm).^2)./(((((x-
x_cm).^2+(y-y_cm).^2+(z-z_cm).^2).^0.5).^2))) - (15.*(x-x_cm).^2.*((z-
z_cm).^2)./(((((x-x_cm).^2+(y-y_cm).^2+(z-z_cm).^2).^0.5).^4)))) ;
fIIIxz  = @(x,y) (((1-(x.^2./a.^2)-(y.^2./b.^2)).^(1./2))./((((x-x_cm).^2+(y-
y_cm).^2+(z-z_cm).^2).^0.5).^3)).*3.*(x-x_cm).*(y-y_cm).*((v./(((((x-
x_cm).^2+(y-y_cm).^2+(z-z_cm).^2).^0.5).^2))) - (5.*((z-z_cm).^2)./(((((x-
x_cm).^2+(y-y_cm).^2+(z-z_cm).^2).^0.5).^4)))) ;

fIyz    = @(x,y) (((1-(x.^2./a.^2)-(y.^2./b.^2)).^(1./2))./((((x-x_cm).^2+(y-
y_cm).^2+(z-z_cm).^2).^0.5).^3)).*3.*(y-y_cm).*(((z-z_cm)./(((((x-x_cm).^2+(y-
y_cm).^2+(z-z_cm).^2).^0.5).^2))) - (5.*((z-z_cm).^3)./(((((x-x_cm).^2+(y-
y_cm).^2+(z-z_cm).^2).^0.5).^4)))) ;
fIIyz   = @(x,y) (((1-(x.^2./a.^2)-(y.^2./b.^2)).^(1./2))./((((x-x_cm).^2+(y-
y_cm).^2+(z-z_cm).^2).^0.5).^3)).*3.*(x-x_cm).*(y-y_cm).*((v./(((((x-
x_cm).^2+(y-y_cm).^2+(z-z_cm).^2).^0.5).^2))) - (5.*((z-z_cm).^2)./(((((x-
x_cm).^2+(y-y_cm).^2+(z-z_cm).^2).^0.5).^4)))) ;
fIIIyz  = @(x,y) (((1-(x.^2./a.^2)-(y.^2./b.^2)).^(1./2))./((((x-x_cm).^2+(y-
y_cm).^2+(z-z_cm).^2).^0.5).^3)).*( (1+v) - (3.*v.*((x-x_cm).^2)./(((((x-
x_cm).^2+(y-y_cm).^2+(z-z_cm).^2).^0.5).^2))) - (15.*(y-y_cm).^2.*((z-
z_cm).^2)./(((((x-x_cm).^2+(y-y_cm).^2+(z-z_cm).^2).^0.5).^4)))) ;

t = zeros(3,2);

t(1,1) = x1;
t(1,2) = y1;

t(2,1) = x2;
t(2,2) = y2;

t(3,1) = x3;
t(3,2) = y3;

rIzz = intm2(fIzz, t);
rIIzz = intm2(fIIzz, t);
rIIIzz = intm2(fIIIzz, t);

rIxz = intm2(fIxz, t);
rIIxz = intm2(fIIxz, t);
rIIIxz = intm2(fIIIxz, t);

rIyz = intm2(fIyz, t);
rIIyz = intm2(fIIyz, t);
rIIIyz = intm2(fIIIyz, t);

end
```

Description:

```
function r = intm2(f, t)
% f: function
% t: three points of a triangle
% r: integration of f over t
a = t(1,:);
b = t(2,:);
c = t(3,:);

jg = abs((b(1)-a(1))*(c(2)-a(2))-(c(1)-a(1))*(b(2)-a(2)));
ftilda = @(u,v) f(a(1)+u*(b(1)-a(1))+v*(c(1)-a(1)), a(2)+u*(b(2)-a(2))+v*(c(2)-
a(2)));

fy = @(x) 1-x;
r = jg * integral2(ftilda, 0,1, 0,fy);

end
```

Description:

```
function
[Kmn_HSIzz,Kmn_HSIIzz,Kmn_HSIIIzz,Kmn_HSIxz,Kmn_HSIIxz,Kmn_HSIIIxz,Kmn_HSIyz,Kmn
_HSIIyz,Kmn_HSIIIyz] =
KmnHS(v,MajorRadius,MinorRadius,x1,x2,x3,y1,y2,y3,z,xc,yc,zc)
a = MajorRadius;
b = MinorRadius;
R2 = @(x,y) ((xc-x).^2+(yc+y).^2+(z-zc).^2).^0.5;

fIzzb = @(x,y) ((2.*v-1).*(4*v-5)./((8.*pi).*(v-1))).*((1./(R2(x,y).^3))-
((3.*(z-zc).^2)./(R2(x,y).^5)));
fIzzd = @(x,y) (((z-zc).^2).*(12.*v-9)./((8.*pi).*(v-1))).*(((5.*(z-
zc).^2)./(R2(x,y).^7))-(3./(R2(x,y).^5)));
fIzze = @(x,y) ((12.*(2*v-1))./((8.*pi).*((y+yc+R2(x,y)).^2).*R2(x,y))).*(1-
((2.*(z-zc).^2)./((y+yc+R2(x,y)).*R2(x,y)))-(((z-zc).^2)./(R2(x,y).^2)));
fIzzf = @(x,y) (3.*((z-
zc).^2)./(2.*pi.*((y+yc+R2(x,y)).^3))).*(((y+yc+3.*R2(x,y)).*((z-
zc).^2)./((y+yc+R2(x,y)).*R2(x,y).^4)) + ((y+yc+3.*R2(x,y)).*((z-
zc).^2)./R2(x,y).^5) - (((z-zc).^2)./R2(x,y).^4) -
((y+yc+3.*R2(x,y))./((R2(x,y).^3)))) ;
fIzzg = @(x,y) ((3.*y.*(3.*y+(2.*v-3).*(y+yc)))./(4.*pi.*(v-
1).*R2(x,y).^5)).*(1-(5.*((z-zc).^2)./(R2(x,y).^2)));
fIzzh = @(x,y) ((15.*y.*yc.*(z-zc).^2)./(4.*pi.*(v-1).*R2(x,y).^7)).*(3-(7.*((z-
zc).^2)./(R2(x,y).^2)));
 fIzz = @(x,y) (((1-(x.^2./a.^2)-(y.^2./b.^2)).^(1./2))).*((fIzzb(x,y)-
fIzzd(x,y)-fIzze(x,y)+fIzzf(x,y)+fIzzg(x,y)+fIzzh(x,y))) ;

fIIzza =  @(x,y)  (1/(8.*pi)).*( ((24.*(xc-x).*(zc-z))./(R2(x,y).^5)) + (-
1.*(90.*(xc-x).*((zc-z).^3))./(R2(x,y).^7)) );
fIIzzb =  @(x,y)  (1/(8.*pi)).*( ((120.*y.^2.*(xc-x).*(zc-z))./(R2(x,y).^7)) +
(-1.*(16.*(xc-x).*(zc-z))./(R2(x,y).^3.*(R2(x,y)+y+yc).^2)) );
fIIzzc =  @(x,y)  (1/(8.*pi)).*( (-1.*(32.*(xc-x).*(zc-
z))./(R2(x,y).^2.*(R2(x,y)+y+yc).^3)) + (-1.*(24.*(xc-x).*(zc-
z).^3)./(R2(x,y).^4.*(R2(x,y)+y+yc).^3)) );
```

```
fIIzzd =  @(x,y)  (1/(8.*pi)).*( (-1.*(60.*y.*yc.*(xc-x).*(zc-z))./(R2(x,y).^7))
+ ((420.*y.*yc.*(xc-x).*(zc-z).^3)./(R2(x,y).^9)) ) ;
fIIzze =  @(x,y)  (1/(8.*pi)).*( (-1.*(8.*(xc-x).*(zc-
z).*(3.*R2(x,y)+y+yc))./(R2(x,y).^3.*(R2(x,y)+y+yc).^3)) + ((24.*(xc-x).*(zc-
z).^3.*(3.*R2(x,y)+y+yc))./(R2(x,y).^4.*(R2(x,y)+y+yc).^4)) );
fIIzzf =  @(x,y)  (1/(8.*pi)).*( ((24.*(xc-x).*(zc-
z).^3.*(3.*R2(x,y)+y+yc))./(R2(x,y).^5.*(R2(x,y)+y+yc).^3)) + (-1.*(120.*y.*(xc-
x).*(zc-z).*(yc+y))./(R2(x,y).^7)) );
fIIzzg =  @(x,y)  (1/(8.*pi)).*( (0) + (0) ) ;
fIIzzh =  @(x,y)  (1/(8.*pi)).*( (0) + (0) );
fIIzzi =  @(x,y)  (1/(8.*pi)).*( (0) + (0) );
 fIIzz =  @(x,y) (((1-(x.^2./a.^2)-
(y.^2./b.^2)).^(1./2))).*((fIIzza(x,y)+fIIzzb(x,y)+fIIzzc(x,y)+fIIzzd(x,y)+fIIzz
e(x,y)+fIIzzf(x,y)+fIIzzg(x,y)+fIIzzh(x,y)+fIIzzi(x,y))) ;

fIIIzza = @(x,y)  (1/(8.*pi)).*( ((27.*(yc-y).*(zc-z))./(R2(x,y).^5)) +
((12.*(zc-z).^3)./(R2(x,y).^4.*(R2(x,y)+y+yc).^2)) );
fIIIzzb = @(x,y)  (1/(8.*pi)).*( ((12.*(zc-z).^3)./(R2(x,y).^5.*(R2(x,y)+y+yc)))
+ ((8.*(zc-z).^3)./(R2(x,y).^3.*(R2(x,y)+y+yc).^3)) );
fIIIzzc = @(x,y)  (1/(8.*pi)).*( ((15.*(zc-z).*(yc+y))./(R2(x,y).^5)) + ((-
1.*(45.*(zc-z).^3.*(yc+y)))./(R2(x,y).^7)) );
fIIIzzd = @(x,y)  (1/(8.*pi)).*( ((-1.*(30.*y.*(zc-z).^3))./(R2(x,y).^7)) +
(15.*(zc-z).*(((-3.*(zc-z).^2.*(yc-y))+(2.*y.*yc.*(y+yc)))./(R2(x,y).^7))) ) ;
fIIIzze = @(x,y)  (1/(8.*pi)).*( ((18.*y.*(zc-z))./(R2(x,y).^5)) + (-
1.*(12.*(zc-z))./(R2(x,y).^2.*(R2(x,y)+y+yc).^2)) );
fIIIzzf = @(x,y)  (1/(8.*pi)).*( (-1.*(12.*(zc-
z))./(R2(x,y).^3.*(R2(x,y)+y+yc))) + (-1.*(24.*(zc-
z))./(R2(x,y).^2.*(R2(x,y)+y+yc).^2)) );
fIIIzzg = @(x,y)  (1/(8.*pi)).*( ((12.*(zc-
z).^3.*(3.*R2(x,y)+y+yc))./(R2(x,y).^4.*(R2(x,y)+y+yc).^3)) + (-1.*(12.*(zc-
z).*(yc+y))./(R2(x,y).^3.*(R2(x,y)+y+yc).^2)) ) ;
fIIIzzh = @(x,y)  (1/(8.*pi)).*( (-1.*(4.*(zc-
z).^3.*(R2(x,y)+3.*y+3.*yc))./(R2(x,y).^4.*(R2(x,y)+y+yc).^3)) + (-
1.*(90.*y.*(zc-z).*(y+yc).^2)./(R2(x,y).^7)) );
fIIIzzi = @(x,y)  (1/(8.*pi)).*( ((90.*y.^2.*(zc-z).*(y+yc))./(R2(x,y).^7)) +
((12.*(zc-z).^3.*(y+yc).*(3.*R2(x,y)+y+yc))./(R2(x,y).^5.*(R2(x,y)+y+yc).^3)) +
((60.*y.*yc.*(zc-z).*(y+yc))./(R2(x,y).^7)) );
 fIIIzz = @(x,y) (((1-(x.^2./a.^2)-
(y.^2./b.^2)).^(1./2))).*((fIIIzza(x,y)+fIIIzzb(x,y)+fIIIzzc(x,y)+fIIIzzd(x,y)+f
IIIzze(x,y)+fIIIzzf(x,y)+fIIIzzg(x,y)+fIIIzzh(x,y)+fIIIzzi(x,y))) ;


fIxza =  @(x,y)  (1/(8.*pi)).*( ((3.*(zc-z).*(xc-x))./(R2(x,y).^5)) + ((-
1.*(45.*(zc-z).^3.*(xc-x)))./(R2(x,y).^7)) );
fIxzb =  @(x,y)  (1/(8.*pi)).*( ((18.*(zc-z).*(xc-x))./(R2(x,y).^5)) + (-
1.*(8.*(zc-z).*(xc-x))./(R2(x,y).^2.*(R2(x,y)+y+yc).^3)) );
fIxzc =  @(x,y)  (1/(8.*pi)).*( (-1.*(4.*(zc-z).*(xc-
x))./(R2(x,y).^3.*(R2(x,y)+y+yc).^2)) + ((12.*(zc-z).^3.*(xc-
x).*(3.*R2(x,y)+y+yc))./(R2(x,y).^4.*(R2(x,y)+y+yc).^4)) );
fIxzd =  @(x,y)  (1/(8.*pi)).*( (-1.*(12.*(zc-z).^3.*(xc-
x))./(R2(x,y).^4.*(R2(x,y)+y+yc).^3)) + (-1.*(8.*(zc-z).*(xc-
x).*(3.*R2(x,y)+y+yc))./(R2(x,y).^3.*(R2(x,y)+y+yc).^3)) );
fIxze =  @(x,y)  (1/(8.*pi)).*( ((12.*(zc-z).^3.*(xc-
x).*(3.*R2(x,y)+y+yc))./(R2(x,y).^5.*(R2(x,y)+y+yc).^3)) + (-1.*(30.*yc.*y.*(zc-
z).*(xc-x))./(R2(x,y).^7)) );
fIxzf =  @(x,y)  (1/(8.*pi)).*( ((210.*yc.*y.*(zc-z).^3.*(xc-x))./(R2(x,y).^9))
+ (-1.*(60.*yc.*y.*(zc-z).*(xc-x))./(R2(x,y).^7)) );
fIxzg =  @(x,y)  (1/(8.*pi)).*( (0) + (0) );
fIxzh =  @(x,y)  (1/(8.*pi)).*( (0) + (0) );
```

```
fIxzi =  @(x,y)  (1/(8.*pi)).*( (0) + (0) );
 fIxz =  @(x,y) (((1-(x.^2./a.^2)-
(y.^2./b.^2)).^(1./2))).*((fIxza(x,y)+fIxzb(x,y)+fIxzc(x,y)+fIxzd(x,y)+fIxze(x,y
)+fIxzf(x,y)+fIxzg(x,y)+fIxzh(x,y)+fIxzi(x,y))) ;

fIIxza = @(x,y)  (1/(8.*pi)).*( (8./(R2(x,y).*(R2(x,y)+y+yc).^2)) + (-
1.*(2./R2(x,y).^3)) );
fIIxzb = @(x,y)  (1/(8.*pi)).*( ((12.*(xc-x).^2)./R2(x,y).^5) + ((12.*(zc-
z).^2)./R2(x,y).^5) );
fIIxzc = @(x,y)  (1/(8.*pi)).*( (-1.*(8.*(xc-
x).^2)./(R2(x,y).^2.*(R2(x,y)+y+yc).^3)) + (-1.*(4.*(xc-
x).^2)./(R2(x,y).^3.*(R2(x,y)+y+yc).^2)) );
fIIxzd = @(x,y)  (1/(8.*pi)).*( (-1.*(8.*(zc-
z).^2)./(R2(x,y).^2.*(R2(x,y)+y+yc).^3)) + (-1.*(4.*(zc-
z).^2)./(R2(x,y).^3.*(R2(x,y)+y+yc).^2)) );
fIIxze = @(x,y)  (1/(8.*pi)).*( (-1.*(90.*(xc-x).^2.*(zc-z).^2)./R2(x,y).^7) +
((12.*y.*yc)./R2(x,y).^5) );
fIIxzf = @(x,y)  (1/(8.*pi)).*( (-1.*(4.*(xc-
x).^2.*(3.*R2(x,y)+y+yc))./(R2(x,y).^3.*(R2(x,y)+y+yc).^3)) + (-1.*(4.*(zc-
z).^2.*(3.*R2(x,y)+y+yc))./(R2(x,y).^3.*(R2(x,y)+y+yc).^3)) );
fIIxzg = @(x,y)  (1/(8.*pi)).*( (-1.*(24.*(xc-x).^2.*(zc-
z).^2)./(R2(x,y).^4.*(R2(x,y)+y+yc).^3)) + (-1.*(60.*y.*yc.*(xc-
x).^2)./R2(x,y).^7) );
fIIxzh = @(x,y)  (1/(8.*pi)).*( (-1.*(60.*y.*yc.*(zc-z).^2)./R2(x,y).^7) +
((24.*(xc-x).^2.*(zc-z).^2.*(3.*R2(x,y)+y+yc))./(R2(x,y).^4.*(R2(x,y)+y+yc).^4))
);
fIIxzi = @(x,y)  (1/(8.*pi)).*( ((24.*(xc-x).^2.*(zc-
z).^2.*(3.*R2(x,y)+y+yc))./(R2(x,y).^5.*(R2(x,y)+y+yc).^3)) + ((420.*y.*yc.*(xc-
x).^2.*(zc-z).^2)./R2(x,y).^9) );
 fIIxz = @(x,y) (((1-(x.^2./a.^2)-
(y.^2./b.^2)).^(1./2))).*((fIIxza(x,y)+fIIxzb(x,y)+fIIxzc(x,y)+fIIxzd(x,y)+fIIxz
e(x,y)+fIIxzf(x,y)+fIIxzg(x,y)+fIIxzh(x,y)+fIIxzi(x,y))) ;

fIIIxza = @(x,y)  (1/(8.*pi)).*( ((9.*(yc-y).*(xc-x))./R2(x,y).^5) +
((3.*(yc+y).*(xc-x))./R2(x,y).^5) );
fIIIxzb = @(x,y)  (1/(8.*pi)).*( ((6.*y.*(xc-x))./R2(x,y).^5) + (-1.*(4.*(xc-
x))./(R2(x,y).^2.*(R2(x,y)+y+yc).^2)));
fIIIxzc = @(x,y)  (1/(8.*pi)).*( (-1.*(4.*(xc-x))./(R2(x,y).^3.*(R2(x,y)+y+yc)))
+ (-1.*(8.*(xc-x))./(R2(x,y).^2.*(R2(x,y)+y+yc).^2)) );
fIIIxzd = @(x,y)  (1/(8.*pi)).*( (-1.*(30.*y.*(xc-x).*(zc-z).^2)./R2(x,y).^7) +
(-1.*(4.*(xc-x).*(yc+y))./(R2(x,y).^3.*(R2(x,y)+y+yc).^2)) );
fIIIxze = @(x,y)  (1/(8.*pi)).*( (-1.*(45.*(xc-x).*(yc-y).*(zc-
z).^2)./R2(x,y).^7) + (-1.*(45.*(xc-x).*(yc+y).*(zc-z).^2)./R2(x,y).^7) );
fIIIxzf = @(x,y)  (1/(8.*pi)).*( ((8.*(xc-x).*(zc-
z).^2)./(R2(x,y).^3.*(R2(x,y)+y+yc).^3)) + ((12.*(xc-x).*(zc-
z).^2)./(R2(x,y).^4.*(R2(x,y)+y+yc).^2)) );
fIIIxzg = @(x,y)  (1/(8.*pi)).*( ((12.*(xc-x).*(zc-
z).^2)./(R2(x,y).^5.*(R2(x,y)+y+yc))) + (-1.*(4.*(xc-x).*(zc-
z).^2.*(R2(x,y)+(3.*y)+(3.*yc)))./(R2(x,y).^4.*(R2(x,y)+y+yc).^3)) );
fIIIxzh = @(x,y)  (1/(8.*pi)).*( (12.*(xc-x).*(zc-
z).^2.*(3.*R2(x,y)+y+yc)./(R2(x,y).^4.*(R2(x,y)+y+yc).^3)) + (12.*(xc-x).*(zc-
z).^2.*(yc+y).*(3.*R2(x,y)+y+yc)./(R2(x,y).^5.*(R2(x,y)+y+yc).^3)) );
fIIIxzi = @(x,y)  (1/(8.*pi)).*( (0) + (0) );
 fIIIxz = @(x,y)  (((1-(x.^2./a.^2)-
(y.^2./b.^2)).^(1./2))).*((fIIIxza(x,y)+fIIIxzb(x,y)+fIIIxzc(x,y)+fIIIxzd(x,y)+f
IIIxze(x,y)+fIIIxzf(x,y)+fIIIxzg(x,y)+fIIIxzh(x,y)+fIIIxzi(x,y))) ;

fIyza =  @(x,y)  (1/(8.*pi)).*( ((3.*(zc-z).*(yc-y))./R2(x,y).^5) + ((18.*(zc-
z).*(yc+y))./R2(x,y).^5) );
```

```
fIyzb =  @(x,y)  (1/(8.*pi)).*( (-1.*(45.*(zc-z).^3.*(yc+y))./R2(x,y).^7) + (-
1.*(30.*y.*yc.*(zc-z).*(yc+y))./R2(x,y).^7) );
fIyzc =  @(x,y)  (1/(8.*pi)).*( ((30.*(zc-z).^3.*y)./R2(x,y).^7) + (-
1.*(12.*(zc-z).*y)./R2(x,y).^5) );
fIyzd =  @(x,y)  (1/(8.*pi)).*( (-1.*(60.*y.*yc.*(zc-z).*(yc+y))./R2(x,y).^7) +
((210.*y.*yc.*(zc-z).^3.*(yc+y))./R2(x,y).^9) );
fIyze =  @(x,y)  (1/(8.*pi)).*( (0) + (0) );
fIyzf =  @(x,y)  (1/(8.*pi)).*( (0) + (0) );
fIyzg =  @(x,y)  (1/(8.*pi)).*( (0) + (0) );
fIyzh =  @(x,y)  (1/(8.*pi)).*( (0) + (0) );
fIyzi =  @(x,y)  (1/(8.*pi)).*( (0) + (0) );
 fIyz =  @(x,y)  (((1-(x.^2./a.^2)-
(y.^2./b.^2)).^(1./2))).*((fIyza(x,y)+fIyzb(x,y)+fIyzc(x,y)+fIyzd(x,y)+fIyze(x,y
)+fIyzf(x,y)+fIyzg(x,y)+fIyzh(x,y)+fIyzi(x,y)));

fIIyza = @(x,y)  (1/(8.*pi)).*( (-1.*(6.*y.*(xc-x))./R2(x,y).^5) + ((9.*(xc-
x).*(yc+y))./R2(x,y).^5) );
fIIyzb = @(x,y)  (1/(8.*pi)).*( ((3.*(yc-y).*(xc-x))./R2(x,y).^5) +
((60.*y.*(xc-x).*(zc-z).^2)./R2(x,y).^7) );
fIIyzc = @(x,y)  (1/(8.*pi)).*( (-1.*(90.*(yc+y).*(xc-x).*(zc-
z).^2)./R2(x,y).^7) + (-1.*(60.*yc.*y.*(xc-x).*(yc+y))./R2(x,y).^7) );
fIIyzd = @(x,y)  (1/(8.*pi)).*( ((420.*y.*yc.*(yc+y).*(xc-x).*(zc-
z).^2)./R2(x,y).^9) + (0) );
fIIyze = @(x,y)  (1/(8.*pi)).*( (0) + (0) );
fIIyzf = @(x,y)  (1/(8.*pi)).*( (0) + (0) );
fIIyzg = @(x,y)  (1/(8.*pi)).*( (0) + (0) );
fIIyzh = @(x,y)  (1/(8.*pi)).*( (0) + (0) );
fIIyzi = @(x,y)  (1/(8.*pi)).*( (0) + (0) );
 fIIyz = @(x,y)  (((1-(x.^2./a.^2)-
(y.^2./b.^2)).^(1./2))).*((fIIyza(x,y)+fIIyzb(x,y)+fIIyzc(x,y)+fIIyzd(x,y)+fIIyz
e(x,y)+fIIyzf(x,y)+fIIyzg(x,y)+fIIyzh(x,y)+fIIyzi(x,y)));

fIIIyza = @(x,y)  (1/(8.*pi)).*( ((12.*(zc-z).^2)./R2(x,y).^5) + (-
1.*(2./R2(x,y).^3)) );
fIIIyzb = @(x,y)  (1/(8.*pi)).*( (-1.*((3.*y.*(y+(3.*yc)))-
(9.*yc.*(y+yc)))./(R2(x,y).^5)) + ((15.*(zc-z).^2.*((y.*(y+3.*yc))-
(3.*yc.*(yc+y))))./(R2(x,y).^7)) );
fIIIyzc = @(x,y)  (1/(8.*pi)).*( ((3.*(yc-y).*(yc+y))./R2(x,y).^5) +
((6.*y.*(yc+y))./R2(x,y).^5) );
fIIIyzd = @(x,y)  (1/(8.*pi)).*( ((6.*y.*yc)./R2(x,y).^5) + (-
1.*(45.*(yc+y).^2.*(zc-z).^2)./R2(x,y).^7) );
fIIIyze = @(x,y)  (1/(8.*pi)).*( (-1.*(30.*y.*yc.*(zc-z).^2)./R2(x,y).^7) + (0)
);
fIIIyzf = @(x,y)  (1/(8.*pi)).*( (0) + (0) );
fIIIyzg = @(x,y)  (1/(8.*pi)).*( (0) + (0) );
fIIIyzh = @(x,y)  (1/(8.*pi)).*( (0) + (0) );
fIIIyzi = @(x,y)  (1/(8.*pi)).*( (0) + (0) );
 fIIIyz = @(x,y) (((1-(x.^2./a.^2)-
(y.^2./b.^2)).^(1./2))).*((fIIIyza(x,y)+fIIIyzb(x,y)+fIIIyzc(x,y)+fIIIyzd(x,y)+f
IIIyze(x,y)+fIIIyzf(x,y)+fIIIyzg(x,y)+fIIIyzh(x,y)+fIIIyzi(x,y)));

t = zeros(3,2);
t(1,1) = x1;
t(1,2) = y1;
t(2,1) = x2;
t(2,2) = y2;
t(3,1) = x3;
t(3,2) = y3;
```

```
  Kmn_HSIzz = intm2(fIzz, t);
 Kmn_HSIIzz = intm2(fIIzz, t);
Kmn_HSIIIzz = intm2(fIIIzz, t);

  Kmn_HSIxz = intm2(fIxz, t);
 Kmn_HSIIxz = intm2(fIIxz, t);
Kmn_HSIIIxz = intm2(fIIIxz, t);

  Kmn_HSIyz = intm2(fIyz, t);
 Kmn_HSIIyz = intm2(fIIyz, t);
Kmn_HSIIIyz = intm2(fIIIyz, t);


end
```

Description:

```
function [K_matrix,major_Radius,minor_Radius,ElementData] =
Kmatrix(v,G,xorigin_coord,yorigin_coord,zorigin_coord,majorRadius,minorRadius,n,
Num)
m=Num;
ElementDatai = zeros(m,15);
X_origini = zeros(m,1);
Y_origini = zeros(m,1);
Z_origini = zeros(m,1);
major_Radiusi = zeros(m,1);
minor_Radiusi = zeros(m,1);

Ne = m*n ;

  for i = 1 : n
   [meshData] = EllipseMesh(majorRadius(i,1),minorRadius(i,1),Num);
   ElementDatai = [ElementDatai; meshData];

   xcracki  = xorigin_coord(i,1)*ones(m,1);
   ycracki  = yorigin_coord(i,1)*ones(m,1);
   zcracki  = zorigin_coord(i,1)*ones(m,1);
   X_origini = [X_origini; xcracki];
   Y_origini = [Y_origini; ycracki];
   Z_origini = [Z_origini; zcracki];

   maj_rad = majorRadius(i,1)*ones(m,1);
   major_Radiusi = [major_Radiusi; maj_rad];

   min_rad = minorRadius(i,1)*ones(m,1);
   minor_Radiusi = [minor_Radiusi; min_rad];

  end


ElementData = zeros(Ne,15);
X_origin = zeros(Ne,1);
Y_origin = zeros(Ne,1);
Z_origin = zeros(Ne,1);
major_Radius = zeros(Ne,1);
```

```
minor_Radius = zeros(Ne,1);

  for i = 1 : Ne

    ElementData(i,:) =  ElementDatai(i+m,:);
       X_origin(i,:) =  X_origini(i+m,:);
       Y_origin(i,:) =  Y_origini(i+m,:);
       Z_origin(i,:) =  Z_origini(i+m,:);
   major_Radius(i,:) =  major_Radiusi(i+m,:);
   minor_Radius(i,:) = minor_Radiusi(i+m,:);

  end

ElementData
%meshData

KmnIzz      = ones(Ne,Ne);
Kmn_hsIzz   = ones(Ne,Ne);

KmnIIzz     = ones(Ne,Ne);
Kmn_hsIIzz  = ones(Ne,Ne);

KmnIIIzz    = ones(Ne,Ne);
Kmn_hsIIIzz = ones(Ne,Ne);

KmnIxz      = ones(Ne,Ne);
Kmn_hsIxz   = ones(Ne,Ne);

KmnIIxz     = ones(Ne,Ne);
Kmn_hsIIxz  = ones(Ne,Ne);

KmnIIIxz    = ones(Ne,Ne);
Kmn_hsIIIxz = ones(Ne,Ne);

KmnIyz      = ones(Ne,Ne);
Kmn_hsIyz   = ones(Ne,Ne);

KmnIIyz     = ones(Ne,Ne);
Kmn_hsIIyz  = ones(Ne,Ne);

KmnIIIyz    = ones(Ne,Ne);
Kmn_hsIIIyz = ones(Ne,Ne);

for i = 1 : Ne
   for j = 1 : Ne
       x1 = ElementData(j,4);
       x2 = ElementData(j,5);
       x3 = ElementData(j,6);
       y1 = ElementData(j,7);
       y2 = ElementData(j,8);
       y3 = ElementData(j,9);

      if i == j
        xcn = ElementData(i,10);
        ycn = ElementData(i,11);

        KNn1 =
KNN1_alt(x1,x2,x3,y1,y2,y3,major_Radius(j,1),minor_Radius(j,1),xcn,ycn);
```

```
        KNn2 =
Knn2(x1,x2,x3,y1,y2,y3,major_Radius(j,1),minor_Radius(j,1),xcn,ycn);

        KmnIzz(i,j)     = (KNn1 + KNn2)*(G/(4*pi));
        KmnIIzz(i,j)    = 0;
        KmnIIIzz(i,j)   = 0;

        KmnIxz(i,j)     = 0;
        KmnIIxz(i,j)    = (KNn1 + KNn2)*(G/(4*pi));
        KmnIIIxz(i,j)   = 0;

        KmnIyz(i,j)     = 0;
        KmnIIyz(i,j)    = 0;
        KmnIIIyz(i,j)   = (KNn1 + KNn2)*(G/(4*pi));

      else
        xcn = ElementData(i,10)+X_origin(i,1)-X_origin(j,1);
        ycn = ElementData(i,11)+Y_origin(i,1)-Y_origin(j,1);
        zcn = Z_origin(i,1);
          z = Z_origin(j,1);


[KmNIzz,KmNIIzz,KmNIIIzz,KmNIxz,KmNIIxz,KmNIIIxz,KmNIyz,KmNIIyz,KmNIIIyz] =
IntgTriangle(major_Radius(j,1),minor_Radius(j,1),x1,x2,x3,y1,y2,y3,z,xcn,ycn,zcn
);

        KmnIzz(i,j)   = (G/(4*pi))*KmNIzz;
        KmnIIzz(i,j)  = (G/(4*pi))*KmNIIzz;
        KmnIIIzz(i,j) = (G/(4*pi))*KmNIIIzz;

        KmnIxz(i,j)   = (G/(4*pi))*KmNIxz;
        KmnIIxz(i,j)  = (G/(4*pi))*KmNIIxz;
        KmnIIIxz(i,j) = (G/(4*pi))*KmNIIIxz;

        KmnIyz(i,j)   = (G/(4*pi))*KmNIyz;
        KmnIIyz(i,j)  = (G/(4*pi))*KmNIIyz;
        KmnIIIyz(i,j) = (G/(4*pi))*KmNIIIyz;

      end
    end

end

    for i = 1 : Ne
            for j = 1 : Ne
               xcn = ElementData(i,10)+X_origin(i,1)-X_origin(j,1);
               ycn = ElementData(i,11)+Y_origin(i,1)-Y_origin(j,1);
               zcn = Z_origin(i,1);

               x1 = ElementData(j,4);
               x2 = ElementData(j,5);
               x3 = ElementData(j,6);
               y1 = ElementData(j,7);
               y2 = ElementData(j,8);
               y3 = ElementData(j,9);
                z = Z_origin(j,1);


[Kmn_HSIzz,Kmn_HSIIzz,Kmn_HSIIIzz,Kmn_HSIxz,Kmn_HSIIxz,Kmn_HSIIIxz,Kmn_HSIyz,Kmn
```

```
_HSIIyz,Kmn_HSIIIyz] =
KmnHS(v,major_Radius(j,1),minor_Radius(j,1),x1,x2,x3,y1,y2,y3,z,xcn,ycn,zcn);

                Kmn_hsIzz(i,j)   = 2*G*Kmn_HSIzz;
                Kmn_hsIIzz(i,j)  = G*Kmn_HSIIzz;
                Kmn_hsIIIzz(i,j) = G*Kmn_HSIIIzz;

                Kmn_hsIxz(i,j)   = 2*G*Kmn_HSIxz;
                Kmn_hsIIxz(i,j)  = G*Kmn_HSIIxz;
                Kmn_hsIIIxz(i,j) = G*Kmn_HSIIIxz ;

                Kmn_hsIyz(i,j)   = 2*G*Kmn_HSIyz;
                Kmn_hsIIyz(i,j)  = G*Kmn_HSIIyz;
                Kmn_hsIIIyz(i,j) = G*Kmn_HSIIIyz;

            end
    end


  K_matrixIzz   = KmnIzz   + Kmn_hsIzz;
  K_matrixIIzz  = KmnIIzz  + Kmn_hsIIzz;
  K_matrixIIIzz = KmnIIIzz + Kmn_hsIIIzz;
  K_matrix_ZZ   = [K_matrixIzz K_matrixIIzz K_matrixIIIzz];

  K_matrixIxz   = KmnIxz   + Kmn_hsIxz;
  K_matrixIIxz  = KmnIIxz  + Kmn_hsIIxz;
  K_matrixIIIxz = KmnIIIxz + Kmn_hsIIIxz;
  K_matrix_XZ   = [K_matrixIxz K_matrixIIxz K_matrixIIIxz];

  K_matrixIyz   = KmnIyz   + Kmn_hsIyz;
  K_matrixIIyz  = KmnIIyz  + Kmn_hsIIyz;
  K_matrixIIIyz = KmnIIIyz + Kmn_hsIIIyz;
  K_matrix_YZ   = [K_matrixIyz K_matrixIIyz K_matrixIIIyz];


  K_matrix      = [K_matrix_ZZ; K_matrix_XZ; K_matrix_YZ];

  K_matrix


end
```

ACKNOWLEDGEMENT

I am eternally grateful to Emeritus Professor Yukitaka Murakami for introducing me to the field of Elasticity, Fracture Mechanics, and Metal Fatigue. The ideas I gathered from Professor Murakami's special courses at Aalto University in 2013 and his earlier works on crack interactions shaped me thinking in this thesis.

I am very grateful to my supervisor, Professor Hisao Matsunaga for his thorough supervision and guidance of this study. Professor Matsunaga's kindness and valuable suggestions was crucial to successful completion of this thesis. Also, I appreciate the valuable supports from Dr. Wada Kentaro and Dr. Saburo Okazaki with specimens preparation and laboratory work.

My sincere gratitude to Professor Masahiro Endo of Fukuoka University and Professor Shigeru Hamada of Kyushu University for thorough review of this dissertation. Their comments and suggestions to the draft manuscript clearly improved the quality of the final version.

I am grateful to Professor Heikki Remes at Aalto University, Finland for accepting me to his laboratory as a visiting researcher during the course of this thesis. I am also grateful to Dr. Pauli Lehto at Aalto University for providing support with laboratory work. I am grateful to Tiina Vuorio at HAMK Research center, Finland for her collaboration and discussions regarding corrosion testing.

This work was completed while I work full-time as Chief Research Engineer for Konecranes Global Oy. It would have been impossible for me to complete this thesis without the support of my managers. I owe a great deal of thanks to Mats Åkesson, Teemu Puustinen, Markku Häivälä and Matti Kemppainen for their flexibility, understanding and encouragements.

I am very grateful to my family and friends for their encouragements and supports in everything I do.

I dedicate this work to my late wife, Kafilat who passed away during the course of this study and to my beautiful daughter, Aisha.

Adeyinka Abass

July, 2023